**EXPERIMENTAL ANALYSIS OF PROPELLER INTERACTIONS WITH A
FLEXIBLE WING MICRO-AIR-VEHICLE**

THESIS

Brian J. Gamble, Captain, USAF

AFIT/GAE/ENY/06-M10

**DEPARTMENT OF THE AIR FORCE
AIR UNIVERSITY**

AIR FORCE INSTITUTE OF TECHNOLOGY

Wright-Patterson Air Force Base, Ohio

APPROVED FOR PUBLIC RELEASE; DISTRIBUTION UNLIMITED

AFIT/GAE/ENY/06-M10

EXPERIMENTAL ANALYSIS OF PROPELLER INTERACTIONS WITH A FLEXIBLE WING MICRO-AIR-VEHICLE

THESIS

Presented to the Faculty

Department of Aeronautics and Astronautics

Graduate School of Engineering and Management

Air Force Institute of Technology

Air University

Air Education and Training Command

In Partial Fulfillment of the Requirements for the

Degree of Master of Science in Aeronautical Engineering

Brian J. Gamble, B.S.A.E.

Captain, USAF

March 2006

AFIT/GAE/ENY/06-M10

EXPERIMENTAL ANALYSIS OF PROPELLER INTERACTIONS WITH A FLEXIBLE WING MICRO-AIR-VEHICLE

Brian J. Gamble, B.S.A.E.

Captain, USAF

Approved:

_____   _____
Dr. Mark F. Reeder (Chairman)   Date

_____   _____
Dr. Donald L. Kunz (Member)   Date

_____   _____
Raymond C. Maple, Lt Col, USAF (Member)   Date

AFIT/GAE/ENY/06-M10

Abstract

An investigation into the effects of the propeller slipstream on a flexible wing micro-air-vehicle (MAV) was conducted. The Air Force Research Lab, Munitions Directorate designed a man-portable MAV with a 24" wingspan and 6" root chord to be used for battle damage assessment and reconnaissance. Two wings have been developed for this MAV. One is a rigid carbon-fiber wing and the other consists of flexible parachute material attached to a carbon-fiber skeleton. Experimental methods were implemented to investigate propeller and wing interactions, characterizing torque and thrust requirements on the motor along with aerodynamic forces on the aircraft as the wing was placed in various locations. Initially, the motor and propeller were mounted on an air bearing table and connected to a torque and load cell. A fuselage prototype was developed and built to mount the wing at multiple heights and distances from the propeller while keeping the same angle of attack. The airframe was attached to a six degree-of-freedom balance. A tri-axial hot-wire anemometer was used to capture velocity profiles in the wind tunnel to characterize propeller wake interactions. Momentum theory provided a method to extract drag and thrust from the velocity profiles. Propeller wake results indicate 12-18% of propeller thrust translates into aircraft drag while 25-45% of motor torque is countered by aircraft roll moment. Values depend on wing location. Results indicate that changing wing location is a viable option for improving pitch and yaw stability, without increasing power requirements.

iv

Acknowledgments

I would like to express my sincere appreciation to my faculty advisor, Dr. Mark Reeder, for his guidance and support throughout the course of this thesis effort. His insight into the sometimes difficult experimental procedures made this research possible and kept me focused. He was always there when I needed him but also listened to my ideas and gave me the opportunity to perform the research in my own manner. I would also like to thank my sponsor, Dr. Michael OL from AFRL/VA, for his support of this research. The research lab team led by Jay Anderson was vital in every step of this project. From Randy Miller who helped create the testing prototype to Andy Pitts and Dwight Gehring who spent countless hours performing difficult calibrations and running lengthy tests. They all did a wonderful job and were always eager to help out. Last, I want to thank my wife and son for showing me the love and support I needed to succeed in this endeavor.

Brian J. Gamble

Table of Contents

List of Figures

List of Tables

List of Symbols

A	Propeller Disc Area
A1	Corrected Axial Force (from Balance)
α	Angle of Attack
β	Sideslip Angle
C_D	Coefficient of Drag
C_L	Coefficient of Lift
C_P	Power Coefficient
C_Q	Torque Coefficient
C_T	Thrust Coefficient
D	Drag
D_∞	Drag due to Freestream Velocity
D_T	Total Drag
D_{PW}	Drag due to Propeller Wake
D	Propeller Disc Diameter
E	Modulus of Elasticity
ε	Wire Strain
FM	Figure of Merit
h_i	Tri-Wire Calibration Pitch Factor
J	Propeller Advance Ratio
k_i	Tri-Wire Calibration Yaw Factor
L	Lift
ℓ	Roll Moment
n	Propeller Rotational Speed (revolutions per second)
η	Propulsive Efficiency
Ω	Propeller Angular Velocity (radians per second)
P	Power
ρ	Air Density
Q	Torque
q_∞	Dynamic Pressure
R	Propeller Radius
Re	Reynolds Number
S	Wing Planform Area
SF	Strain Factor
σ	Stress
T	Thrust
u	Axial Velocity Component (Body Axis)
U_i	Tri-Wire Specific Velocities (Wire Axis)
v	Vertical Velocity Component (Body Axis)
V_O	Velocity Behind Propeller Disc
V_S	Velocity Well Downstream of Propeller
V	Velocity Upstream of Propeller

V_1	Velocity Upstream of Body
V_2	Velocity Downstream of Body
V_s	Strain Gauge Input Voltage
V_o	Strain Gauge Output Voltage
w	Spanwise Velocity Component (Body Axis)
W	Aircraft Weight
x	Axial Coordinate (Body Axis)
X_o	Axial Separation Between Propeller and Wing
y	Spanwise Coordinate (Body Axis)
z	Vertical Coordinate (Body Axis)
Z_o	Vertical Separation Between Propeller and Wing

EXPERIMENTAL ANALYSIS OF PROPELLER INTERACTIONS WITH A FLEXIBLE WING MICRO-AIR-VEHICLE

I. Introduction

Background

Unmanned Aerial Vehicles (UAVs) have become an integral part of the aerospace community. They have numerous military and civilian applications including surveillance, search and rescue, damage assessment, reconnaissance and tactical attack. Currently the military uses these vehicles primarily for gathering intelligence, surveillance, and reconnaissance. The most notable current UAVs used by the military for these purposes are the Predator and Global Hawk. The Joint Unmanned Combat Air Systems (J-UCAS) program, developed by the Defense Advanced Research Projects Agency (DARPA) in conjunction with the Air Force and Navy, is currently investigating the possibility of using weaponized UAVs in combat missions (darpa.mil). These full size UAVs are valuable assets to the military, but possess limitations similar to manned aircraft for quick surveillance and battle assessment in the field.

In order to meet the demands of special forces teams to acquire real-time surveillance at relatively short distances of less than five miles, DARPA defined a new category of UAVs, called Micro-Air-Vehicles (MAVs) (McMichael and Francis, 1997). These MAVs are much smaller and cheaper than current UAVs and could be used to perform similar missions. They would also possess the capability to perform unique military missions such as covert imaging in constrained areas, biological and chemical agent detection and urban battlefield communications enhancement (fas.org). They

1

would potentially use electric motors and carry camera equipment to provide on-demand information to the soldier about his surroundings, resulting in unprecedented situational awareness and fewer casualties (McMichael and Francis, 1997). The Air Force Research Lab, Munitions Directorate, Flight Vehicles Integration Branch (AFRL/MNAV) developed a carbon-fiber matrix MAV with a 24" wing consisting of a rigid skeleton overlapped by a flexible material. This MAV is designed to be folded and carried by soldiers in their pack. When removed from the pack, the wing would expand and the MAV could be remotely piloted over the next hill to provide surveillance information back to the soldiers. AFRL/MNAV requested that AFIT perform extensive wind tunnel testing on the flexible wing model and compare it to a rigid wing of identical planform.

In a project supported by AFRL/MNAV, Captain Anthony DeLuca (USAF) performed an experimental wind tunnel investigation to determine the aerodynamic performance characteristics of the MAV and reported results in ref. #10. The aircraft was characterized for both the flexible wing and a rigid wing of the identical shape in the tests. The experiments included finding lift, drag and side forces along with pitch, roll and yaw moments at multiple tunnel speeds. Ref. #10 also documents the stability derivatives and investigates control surface deflection effects. Finally, a limited number of powered runs were performed in an attempt to capture gross characteristics of the motor/propeller performance. Lieutenant Jose Rivera Parga (Mexican Navy) and Ensign Troy Leveron (USNR) also performed wind tunnel tests on the MAV at AFIT. Their experiments focused on the flight quality of different empennage configurations. They

primarily investigated the effects of changing the current v-tail design to a rotatable, bird-like tail system as described in ref. #34 and #29.

Although numerous studies of propeller/wing interactions have been accomplished, the full effects of the propeller driven propulsion system on the flexible wing are unknown. Experimental tests provide insight into thrust and power variations, aerodynamic effects on the wing and fuselage, propeller upwash/downwash (propwash) and aeroelastic vibrations (Witkowski et al., 1999: Fratello et al., 1991: Chiaramonte et al., 1996). Free wake analysis (FWA) models also attempt to describe the influence of the propeller on the wing (Favier et al., 1989: Ardito Maretta, 1998). Basic research includes these effects on rigid wings of different shapes and orientations, however an understanding of the effects on a flexible wing would provide an improved basis for future MAV designs.

Problem Statement

Propulsion systems for MAVs have to satisfy extraordinary requirements for high power density (McMichael & Francis, 1997). Power requirements for the MAV were not thoroughly documented in earlier work. Even for the handful of powered runs, due to the coupled effects of the propeller/wing interactions, independent motor power values could not be obtained using a six degree-of-freedom balance alone. Rather, the measured power values obtained by Captain DeLuca included both the motor torque and the reaction torque, or roll moment of the MAV, which will indicate a value less than the actual required power. Without a method for obtaining reliable, independent motor torque and thrust values, it is difficult to quantify how changes to the MAV design could

3

improve its power requirements. In general, for a propeller driven aircraft there are a number of ways to reduce the power required, including minimizing wing loading and vehicle weight, and maximizing lift to drag ratio (McMichael & Francis, 1997). It has already been demonstrated that the flexible wing reduces the weight of the MAV and provides higher lift to drag ratios versus the rigid wing (DeLuca, 2004:57).

The stability of the vehicle is also a primary concern, and Captain Travis Higgs (USAF) in ref. #20 showed that maintaining roll stability and directional stability is a challenge with the vehicle tested. One way to improve directional stability is to move the aircraft center of gravity to a forward position. This in turn may require the center of lift to shift forward as well to maintain a proper pitch moment for the aircraft. This could be accomplished in a straightforward manner by repositioning both the battery pack and the wing more forward. However, it is unclear how a reduced distance from the wing to the propeller might influence both propeller efficiency and the torque budget for the single-propeller aircraft.

More generally, power-on effects on performance and stability have not been studied in much detail for MAVs, apart from flight tests, in part due to the difficulty inherent in obtaining good data. One potential means of accounting for powered effects is by using momentum theory, which in turn requires an accurate depiction of the velocity field around the vehicle. A limited number of tests have been performed to assess the technique in comparison to force balance data.

4

Research Objectives

The objectives of this experimental study were to evaluate the propeller/wing interactions of both the rigid and flexible wings at multiple wing locations. This includes measuring the variations in motor thrust and torque along with aerodynamic reactions on each wing of the MAV. Velocity measurements provided the opportunity to characterize the flowfield created by the propeller wake in addition to the freestream velocity. These objectives were accomplished by the following:

- Independently measure motor thrust and torque coefficients, airframe lift, drag and roll moment due to propwash. This was accomplished using a unique experimental setup but was limited to static tests. Wing location, relative to the propeller, was varied as part of this experiment.

- Measure the propeller-on, powered vehicle forces and moments using a six-component balance in the AFIT low-speed wind tunnel at flight conditions

- Measure velocity in the wind tunnel with a three-component hot-wire at multiple locations, with and without each wing, in the wake of the propeller only and with the addition of freestream tunnel velocity. Utilize momentum theory with velocity profiles to characterize thrust and drag.

The focus of this research is to determine the level of propwash effects on the aerodynamics of the MAV along with power requirement variations as the wing is positioned in different locations. Differences in the characteristics of the rigid and flexible wings are an important parameter to assess. Notably, angle of attack, α, and sideslip angle, β, were not varied in these tests.

Methodology/Limitations

To begin the task of measuring thrust and torque on the motor separately, a test was developed in which the propeller was placed on a reverse rotation motor attached to

a torque cell and load cell. The device rested on an air bearing table providing a near frictionless environment. The MAV wing was mounted on a modeled fuselage which permitted the wing to be repositioned axially without changing angle of attack. The MAV was positioned in front of the propeller in its typical configuration and connected to a six degree-of-freedom (6 DOF) balance to provide aerodynamic load data. This test was performed out of the tunnel with only the propeller providing air flow. The setup for separating the MAV from the motor was limited to tests outside the tunnel due to flow interference effects. Therefore, all of the relationships between motor thrust and torque and aerodynamic loading as a function of wing placement developed in this research are for the zero freestream case. This is one of the limitations of this research, but the possibility of performing these tests in the wind tunnel could be investigated in the future.

Powered runs in the wind tunnel for the MAV, as configured for flight, were used to define the flowfield velocity, which provided information on the propeller effects beyond those performed outside the tunnel and helped validate results from the first test. Graphical illustrations of the velocity profiles clearly show the axial and cross-stream velocity components created by the propeller slipstream and how the flowfield interacts with the rigid and flexible wings. Velocity profiles were also used with momentum theory to extract thrust and drag values. Due to physical constraints inside the tunnel, some of the velocity data had to be interpolated, which is another limitation of this research. The combination of the two experiments offers valuable insight into the propeller/wing interaction phenomenon for the MAV.

Preview

The following research provides insight into the effects of propeller/wing interactions, characterizing both a rigid and a flexible wing MAV. Chapter II details some of the important research previously performed on the MAV along with other experimental and analytical research done on propeller/wing interactions. It also includes some general information on propeller performance, wake development and momentum theory.

Chapter III outlines the methodology of the entire set of experiments. Full test descriptions including the equipment used for the tests, experimental procedures and data analysis along with photographs and design justification are included. Chapter IV includes numerical and graphical results of each test as well as a detailed observational and interpretive analysis. Finally, a complete summary of conclusions as well as recommendations for follow-on work and improvements are discussed in chapter V.

II. Literature Review

Overview

The purpose of this chapter is to make familiar the technology and engineering concepts incorporated into the experimental research conducted on the MAV. It includes necessary background information on flexible wing MAVs, propeller performance and wake development, propeller/wing interaction experiments, propeller velocity field experiments and momentum theory.

Flexible Wing MAVs

The recent push toward designing small unmanned aerial vehicles for military use has led to numerous advances in MAV technology. Rapid progress in the miniaturization of sensors, actuators and communications hardware has made the desired mission of MAVs a possibility. Along with size reduction and the slow flight speeds of MAVs comes difficulty in maintaining aerodynamic performance (Shyy et al., 1999:523). The performance of the flight vehicle can be expressed in terms of the lift to drag ratio, or in more specific terms, of the flight power requirements for steady level flight given by:

$$P = W \left(\frac{C_D}{C_L^{\frac{3}{2}}} \right) \sqrt{ \left(\frac{2}{\rho} \right) \left(\frac{W}{S} \right) } \tag{1}$$

Where:
P = power required
W = aircraft weight
C_D = drag coefficient

C_L = lift coefficient
ρ = air density
S = wing planform area

In order to decrease power required and improve MAV flight performance, lift to drag must increase, weight must decrease, or planform area must increase. Since the focus of the MAV is to reduce size, the rigid planform area is limited. Also, the more the weight of a MAV is reduced, the more susceptible the vehicle is to wind gusts and unsteady flight conditions. Therefore, MAVs require airfoils capable of sustaining good lift to drag performance over a range of flow conditions (Shyy et al., 1999:523).

Currently the Reynolds numbers (Re) for most MAVs fall in the range of 10^4 – 10^5. At such low Reynolds numbers the flow around the leading edge of the wing is usually laminar. Also, low Re can result in a situation where the boundary layer fluid momentum is not enough to overcome the adverse pressure gradient on the back of the wing causing laminar separation to occur (Mueller, 1989). This flow separation can lead to sudden increases in drag and a loss of efficiency (Ifju et al., 2002:1). In an attempt to mitigate flow separation and gust effects experienced by MAVs, a flexible wing design is used. It has the ability to change shape during flight and sustain good performance in a fluctuating environment (Shyy & Smith, 1997). The ability to adapt to the airflow is known as adaptive washout. It is produced through the extension of the flexible membrane and twisting of the skeletal framework, which results in angle of attack changes as well as decambering along the length of the wing (Ifju et al., 2002:2). According to Ifju, as a plane hits a head-on gust the airspeed suddenly increases, causing a shape change in the wing that decreases the lifting efficiency. Because the airspeed in

9

the gust is higher, the wing maintains nearly the same lift. The opposite occurs when the airspeed decreases, resulting in a wing that flies with exceptional smoothness. DeLuca, Reeder, OL and Freeman (ref. #11) demonstrated that the lift to drag (L/D) curve was broadened with respect to angle of attack (α) through a similar mechanism.

To further improve the design of MAVs, studies were performed by Shyy et al. (ref. #35) to investigate airfoil shape and thickness. They found that increasing camber on the airfoil at low Reynolds numbers increases performance. They also deduced that a thinner airfoil with the same camber will exhibit better aerodynamic performance while maintaining acceptable angles of attack (Shyy et al., 1999:525-526).

The experiments conducted at AFIT are all done on variants of the MAVs shown in Figure 1. Both the rigid and flexible wing models are shown. The flexible wing model was described as BATCAM, short for combat camera. Since the time AFRL/MNAV provided AFIT with the MAVs, it is notable that the vehicle has undergone several design changes, both in its utilization in the field and in experimental research.

Figure 1. Flexible and Rigid Wing MAVs Provided by AFRL/MNAV

Experimental results from tests conducted by Captain DeLuca show comparative

lift to drag ratio curves for the rigid wing and flexible wing models shown in Figure 1.

The curves, shown in Figures 2 and 3, indicate results similar to tests conducted by

Waszak and Jenkins (ref. #39) on flexible wing MAVs. The flexible wing is able to

achieve higher *L/D* values at nearly all angles of attack and tunnel velocities. Also, as

seen in the coefficient of lift curves of Figure 3, the flexible wing delays stall up to 4

degrees at low velocities. So far, all of the current studies performed on flexible wing

MAVs indicate a valuable aerodynamic improvement over their rigid wing counterparts.

Another advantage of the flexible wing is its ability to be rolled-up into a more

compact configuration as seen in Figure 4. This enables soldiers to carry a smaller

vehicle yet still be able to deploy a MAV that has adequate wing loading. The desired

low wing loading is achieved by having large wing areas and lightweight vehicles.
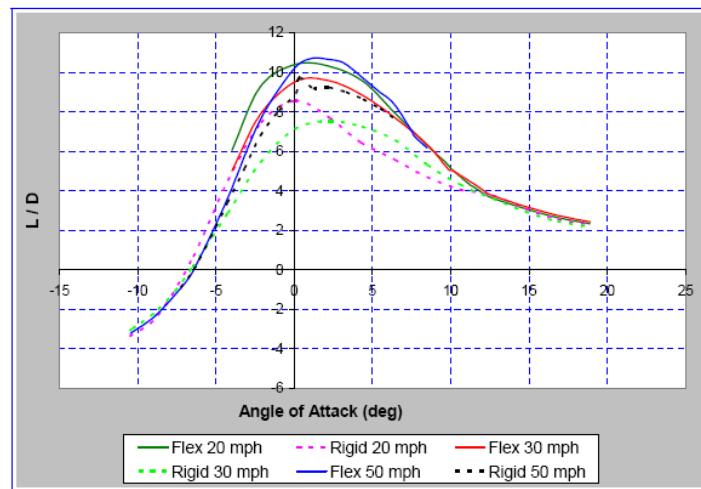
Figure 2. L/D vs. α for AFIT MAV (DeLuca, 2004:57)
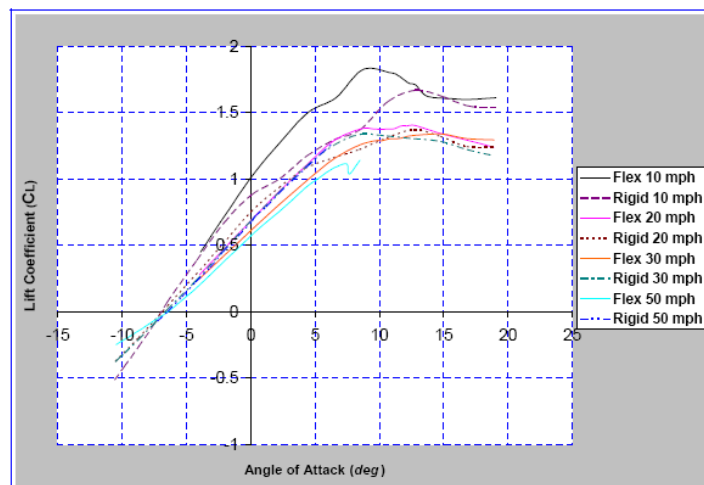
Figure 3. C_L vs. α for AFIT MAV (DeLuca, 2004:48)
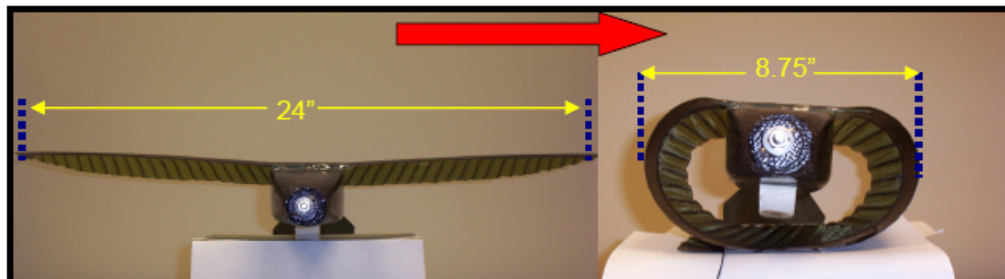
Figure 4. AFIT MAV Flexible Wing Folded-up (Rivera Parga, 2004:7)

Propeller Performance

Current flexible wing MAVs are being powered by small electric motors and propellers. The performance of these propellers remains of vital interest given the high power density requirements of MAVs in low Reynolds number environments. The three primary measures of performance for propellers are the coefficients of thrust (C_T) and power (C_P) along with propulsive efficiency (η). Equations **(2)** through **(4)** show how these values are obtained from experimental data (Nelson, 1944:24).

$$C_T = \frac{T}{\rho \pi R^2 (\Omega R)^2} \tag{2}$$

$$C_P = \frac{P}{\rho \pi R^2 (\Omega R)^3} \tag{3}$$

$$\eta = \frac{C_T}{C_P}\left(\frac{V}{nD}\right) \tag{4}$$

In these equations, Ω is the propeller angular velocity in radians per second, R and D are the radius and diameter of the propeller respectively, n is the propeller rotation speed in revolutions per second, T is the thrust and P is the power. The power is directly related to the propeller torque, Q, by $P = \Omega Q$ and $C_P = C_Q$ (Leishman, 2002:44). The value (V/nD) is also referred to as the advance ratio, J, where V is the forward velocity of the aircraft (Raymer, 1992:327).

Since a number of the experiments conducted in this research are conducted at zero freestream velocity, another propeller measure of efficiency is adopted from the

rotorcraft community. Normally used in describing the thrust efficiency of a hovering

rotorcraft, the figure of merit (*FM*), is the ratio of the ideal power required to hover to the

actual power. Figure of merit is defined in equation **(5)** (Leishman, 2002:46).

$$FM = \frac{C_T^{3/2}}{\sqrt{2}C_P}$$ **(5)**

Many archival publications relating thrust and power coefficients to advance ratio

show some general trends for propellers. Figure 5 shows power coefficient and thrust

coefficient curves versus advance ratio for a two-blade Clark-Y section propeller

(Nelson, 1944:111). As the advance ratio increases, the coefficient of power decreases as

a result of a higher inflow velocity reducing the effective angle of attack on the blades of

the propeller, decreasing the aerodynamic torque on the blades and reducing the power

required on the motor (Nelson, 1944:36). Similarly, as advance ratio increases, the

coefficient of thrust decreases since the higher inflow velocity reduces the amount of

thrust produced by the propeller. In forward flight the propeller thrust is proportional to

the inverse of the velocity (Raymer, 1992:329). For a fixed advance ratio, as the thrust

coefficient increases so does the power coefficient.
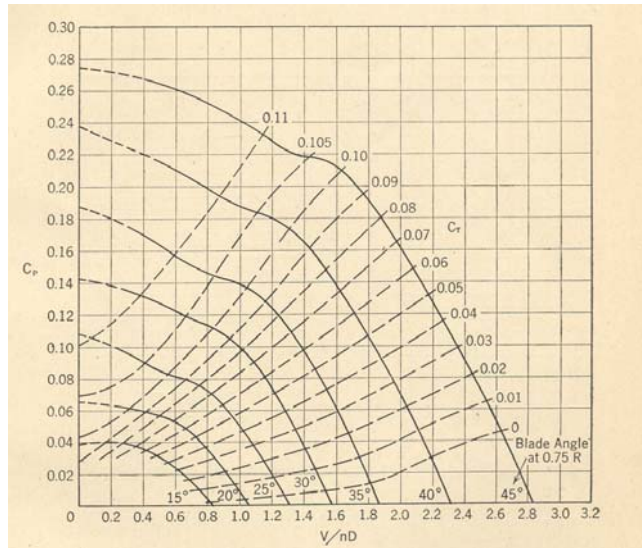
Figure 5. Power Coefficient Curves for 2-Bladed Propeller (Nelson, 1944:111)

Propeller Wake Generation

The flowfield generated by the turning of a propeller is extremely complicated, involving wake/freestream interaction, wake decay, vortex shedding and tip vortex/wake interaction (Lepicovsky and Bell, 1983:264). Numerous experimental and computational studies have been performed in an attempt to define this flowfield. These studies range from actual velocity measurements and flow visualization techniques to numerical methods based on free-wake-analysis computations. A few examples are described here, in part, to emphasize the value of velocity data in characterizing propwash.

In 1996, Fukada, Nigim and Koyama (ref. #18) performed smoke-wire flow visualization and hot-wire anemometry measurements on a 16 in. diameter two-bladed propeller at 1500 revolutions per minute (RPM) in static (zero freestream velocity) conditions. They measured the velocity field at multiple locations behind the propeller. Figure 6 shows the axial (a), radial (b) and tangential (c) mean-time and ensemble-

15

averaged velocity components just behind the propeller. According to this data, the

maximum axial mean velocity component is located at a radial distance $0.8R$ from the

center of the propeller. It also shows that both the axial and radial components of the

velocity just behind the propeller fluctuate rapidly yet the tangential, or rotational,

velocity remains fairly constant.
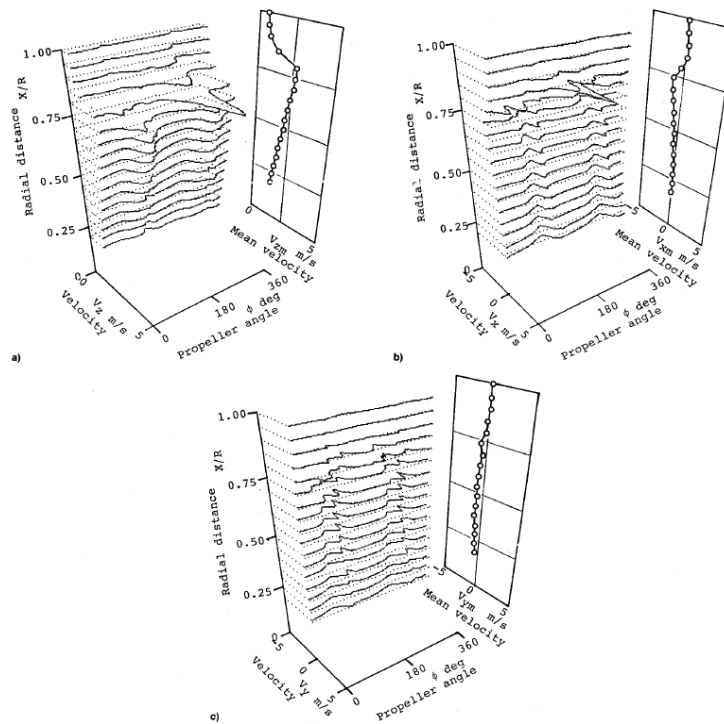
Figure 6. Radial Distributions of Propeller Wake Velocity Field (Fukada, Nigim & Koyama, 1996:411)

Figure 7 shows the axial velocity component at a radial distance $0.5R$ from the

center of the propeller. The profile shows the results from just aft of the propeller to 8

inches aft. The mean velocity plot shows a virtually constant value over the entire range.

Figure 8 presents the unsteadiness of the axial velocity profile and shows how the

velocity field becomes more steady the farther aft of the propeller. These type of flow

patterns could help explain why a wing is placed in a certain location with respect to the

propeller. All of the velocity measurements presented in Chapter IV are time-averaged

and not analyzed for unsteadiness however, this type of data is available and can be

useful in flowfield analysis.
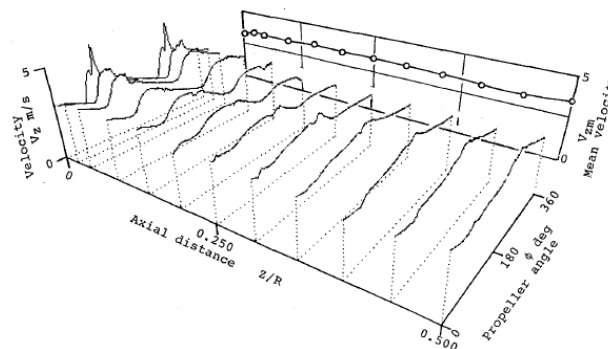
Figure 7. Axial Distribution of Propeller Wake Velocity Field (Fukada, Nigim & Koyama, 1996:410)
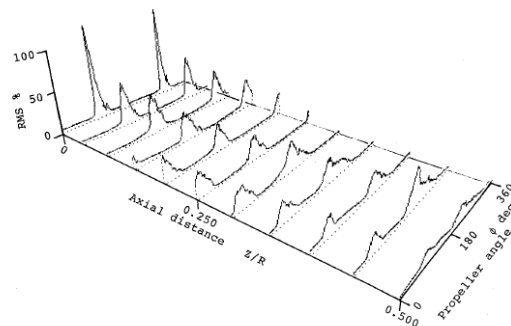
Figure 8. Axial Velocity Unsteadiness Profiles at 0.5R (Fukada, Nigim & Koyama, 1996:412)

Lepicovsky and Bell (ref. #28) performed similar tests on a 13 in. diameter two-

bladed propeller using a laser velocimeter to measure the three-dimensional velocity

field. The tests they performed at 4250 RPM demonstrated that a maximum axial mean

17

velocity component occurred at a radial distance $0.7R$ from the center of the propeller in the near field behind the propeller. They also found at that radial distance ($0.7R$), the axial velocity component reaches its maximum at approximately $0.2R$ aft of the propeller then starts to gradually decrease (Lepicovsky & Bell, 1983:267). Interestingly, the radial velocity component reaches its largest magnitude in the negative (inward) direction close to the propeller disk and remains negative nearly everywhere in the flowfield, indicating a slipstream contraction. Finally, the tangential or swirl velocity component starts just aft of the propeller disk and reaches a relatively constant value axially behind the propeller (Lepicovsky & Bell, 1983:269).

Favier, Ettaouil and Maresca (ref. #14) used a free-wake-analysis (FWA) approach to model the flowfield geometry behind a four-bladed propeller. The free wake assumes the geometry corresponding to the bound circulation distribution is determined by the inflow velocities and blade configuration. It constantly updates the wake geometry until it converges on a bound circulation and thrust coefficient (Favier, Ettaouil & Maresca, 1989:837). They compared their wake model to experiment and found similar results. Figure 9 shows a comparison of experiment and calculation of the radial velocity flowfield for phase-averaged velocities at two axial positions. It provides a good visual idea of what the flowfield is doing behind a typical propeller. Propwash velocity profiles presented in Chapter IV are time-averaged and take on slightly different characteristics. Figure 10 shows a calculated vortex-sheet geometry from the FWA model and provides another conceptual view of the propeller's flowfield development.

Figure 9. Radial Velocity Flowfield Behind Four-Bladed Propeller (Favier, Ettaouil &Maresca 1989:844)

Fig. 14   Calculated vortex-sheet geometry shed from one blade at $\tau = 0.16$: a) $\alpha_o = 23$ deg, $\gamma = 0.44$; and b) $\alpha_o = 32.5$ deg, $\gamma = 0.89$.

Figure 10. Vortex Sheet Geometry Behind Single Propeller Blade (Favier, Ettaouil &Maresca 1989:845)

19
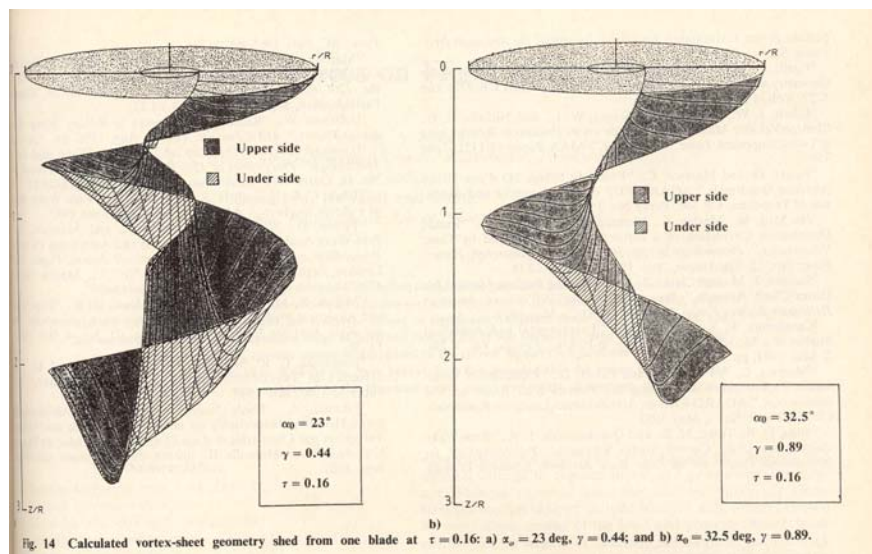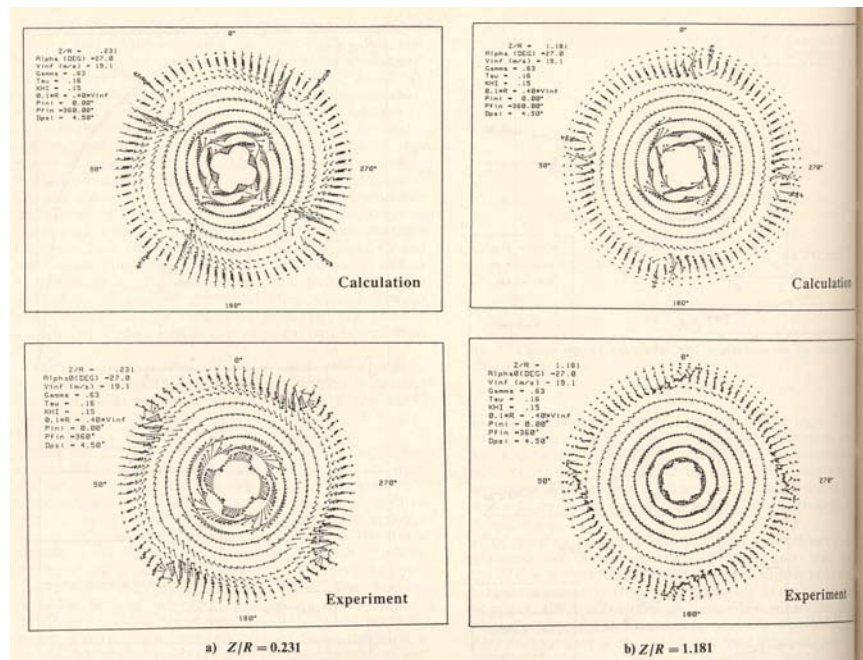
Propeller/Wing Interaction

As a wing is introduced into the flowfield behind a propeller there is a net slipstream influence on the aerodynamics of the wing. The presence of the wing also has an effect on the propeller thrust and power coefficients. In the vast majority of experimental and numerical studies performed on propeller/wing interactions, the emphasis is generally placed on the influence of the wake generated by the propeller on the wing aerodynamics. However, the wing also has the effect of substantially changing the wake geometry and propeller performance (Fratello, Favier & Maresca, 1991:366). They go on to say:

> A proper investigation of the propeller/wing interaction problem thus requires one to characterize both the propeller slipstream effect on the wing and the reciprocal influence of the wing presence on the propeller flowfield and performances.

In an attempt to quantify this statement, Fratello et al. set up an experiment to test the propeller/wing interactions in a wind tunnel. In their experiment, a four-bladed 34 inch diameter propeller was attached to a nacelle and a wing as seen in Figure 11. The motor and torquemeter were housed in the nacelle and the wing was mounted on a mast with a set of strain gauges for lift, drag and moment measurements (Fratello, Favier & Maresca, 1991:366). Through a series of tests where the wing was both coupled and uncoupled from the propeller/nacelle, they were able to extract the basic contributions of each element.
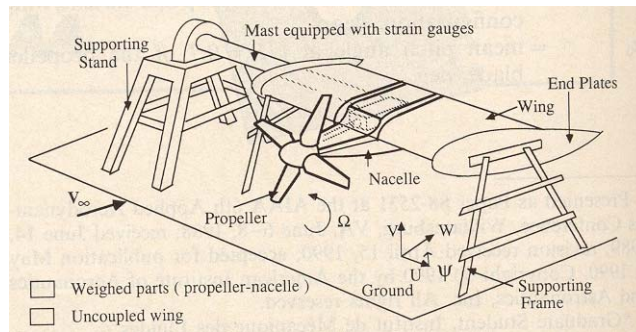
Figure 11. Propeller Interaction Experimental Setup (Fratello et al., 1991:366)

The overall findings of their experiment were that the net slipstream influence on the wing is characterized by an increase of the drag coefficient for the wing as the thrust of the propeller increases. Also, the overall lift coefficient decreases as the thrust increases. From measurements obtained by spanwise pressure taps they deduced that the lift coefficient increases behind the up-going blade and decreases behind the down-going blade. This is consistent with other research conducted by Chiaramonte et al. in 1996 (ref. #5), and Cho and Williams in 1990 (ref. #7). The other interesting results of their experiment were the effects the wing had on the propeller performance. Figure 12 shows the results the addition of the wing in the flowfield had on the propeller thrust and power coefficients. In these plots, γ is the advance ratio, τ is the thrust coefficient and χ is the power coefficient. The results indicate a fairly constant increase (14%) in thrust over the range of advance ratios as well as a constant increase (8%) in power. The power coefficient increase is probably caused by the straightening effect of the wing on the propeller slipstream (Fratello, Favier & Maresca, 1991:370). Since the propeller operated at constant rotating frequency, the increase in thrust and power coefficients results in an increase of power from the electric motor.

21
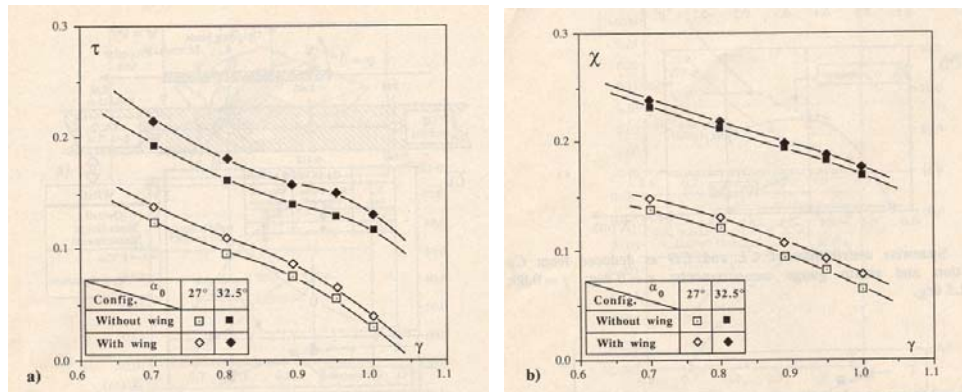
Figure 12. Thrust and Power Coefficients (Fratello et al., 1991:370)

In another experiment conducted by Witkowski, Lee and Sullivan (ref. #38) at
Purdue University, propeller/wing interactions were tested in a wind tunnel using the
setup shown in Figure 13. They were able to measure time-averaged lift and drag on the
wing as well as motor thrust and power separately, although some corrections were
required due to losses in the belt drive. Keeping the same vertical and horizontal distance
between the propeller hub and the wing quarter-chord, they varied the angle of attack of
the wing and the advance ratio to produce their results. Figure 14 shows both the
reaction force coefficients on the wing as well as the propeller performance measures.
There is a difference in experimental configuration from that of Figure 11. First, the
wing in this case is level with the center of the propeller hub instead of above it. Second,
the propeller is mounted at the outermost spanwise part of the wing as seen in the top
view of Figure 13. This causes the upwash part of the propeller wake only to act on the
wing. The propeller swirl then helps to counteract the wing's downwash which
effectively increases the local angles of attack, enhancing the section lift and rotating the
force vector forward, decreasing drag (Witkowski et al., 1989:830). Therefore, as power

increases, lift increases and drag decreases. As expected, both the coefficients of thrust

and power decrease as advance ratio increases.
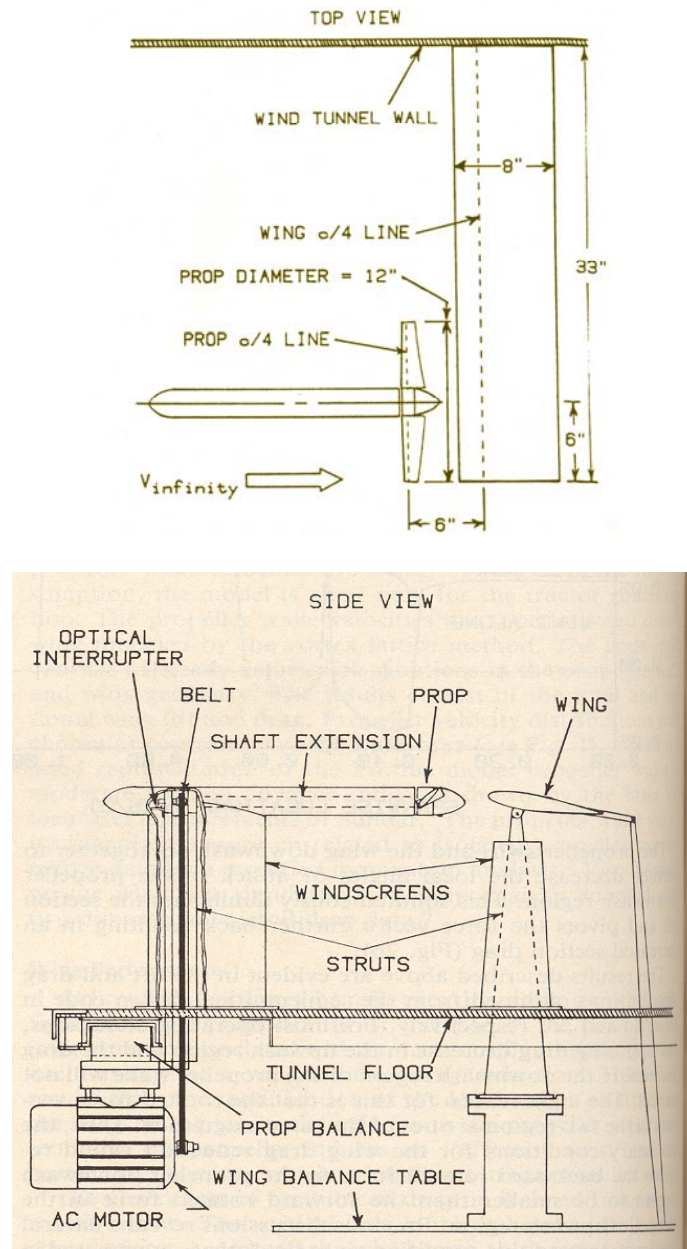
Figure 13. Purdue University Interaction Setup (Witkowski et al., 1989:832)
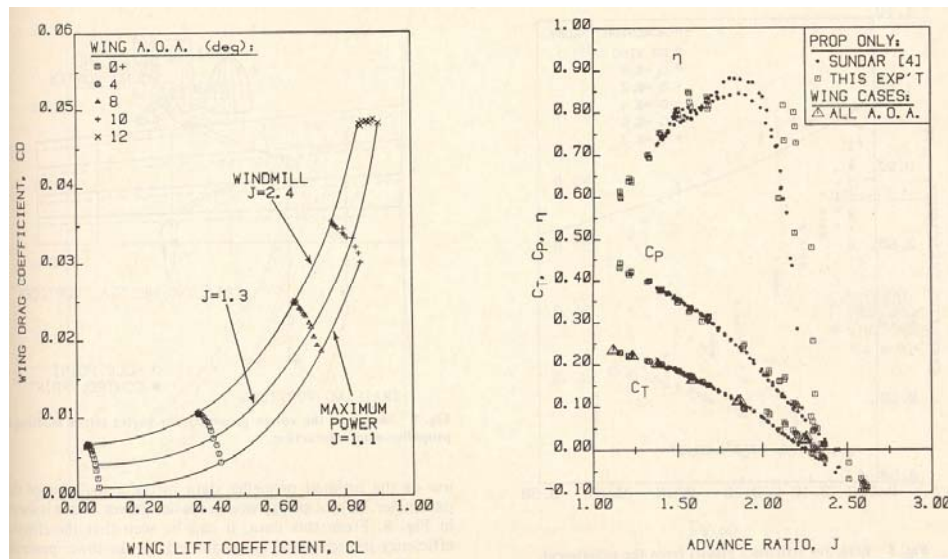
Figure 14. Wing Reaction Forces/Propeller Performance (Witkowski et al., 1989:833)

Numerous other studies have been conducted examining the effects of propeller and wing interactions. In 1990, Bi and Leishman (ref. #4) performed wind tunnel experiments on the mutual interactions between a helicopter rotor and fuselage. They performed similar experiments between a helicopter rotor and fixed lifting surfaces in 1994 (ref. #27). Chiocchia and Pignataro (ref. #6) studied induced drag due to propeller-wing interactions and investigated ways to reduce drag by positioning two propellers on the outer portion of the wing; similar to the mechanism studied by Witkowski et al.. E, Yang and Li (ref. #12) performed numerical analysis via a panel method to investigate the interference effects of a propeller slipstream on a typical aircraft flowfield. Finally, Elsaadawy and Britcher (ref. #13) performed wind tunnel tests to investigate the effects of the intermittent turbulence shed by a propeller on the boundary layer at low Reynolds numbers.

Momentum Theory

A simple momentum theory analysis can be used to estimate the thrust of a propeller. The propulsive force is achieved by increasing the momentum of air in the opposite direction of the force. The theory, developed by Froude, assumes that the propeller acts as a pure energy supplier. It also assumes that the propeller is an infinitely thin disc with area, A, and that thrust loading and velocity are uniform over the disc (Houghton & Carpenter, 1993:461). With these assumptions in a one-dimensional flow analysis, the propeller thrust can be found by:

$$T = \rho A V_O (V_S - V) \tag{6}$$

Where:
A = propeller disc area
V_O = velocity behind disc
V_S = velocity well downstream
V = velocity well upstream (freestream)

In a similar fashion, momentum theory can be used to determine the drag of a body from the velocity measurements in its wake. When a body is introduced into a flowfield, viscosity effects cause the wake behind the body to be retarded. In the wake region, the velocity is less than the upstream value (Kuethe & Chow, 1986:66). Figure 15 illustrates the velocity profile downstream of a body in a flow. Assuming steady incompressible 2-D flow and negligible gravity effects, mass conservation requires that

$$\rho V_1 dy_1 = \rho V_2 dy_2 \tag{7}$$

which can also be written as

25

$$D = \int_{Sta.2} \rho V_2 (V_1 - V_2) dy_2 \qquad \textbf{(8)}$$

In this equation, the integrand represents the momentum lost by the fluid leaving the control volume through dy_2 per second (Kuethe & Chow, 1986:67). According to the momentum theorem, this is exactly equal to the drag per unit length of the body. The same can be extended to the three dimensional case using surface integrals.
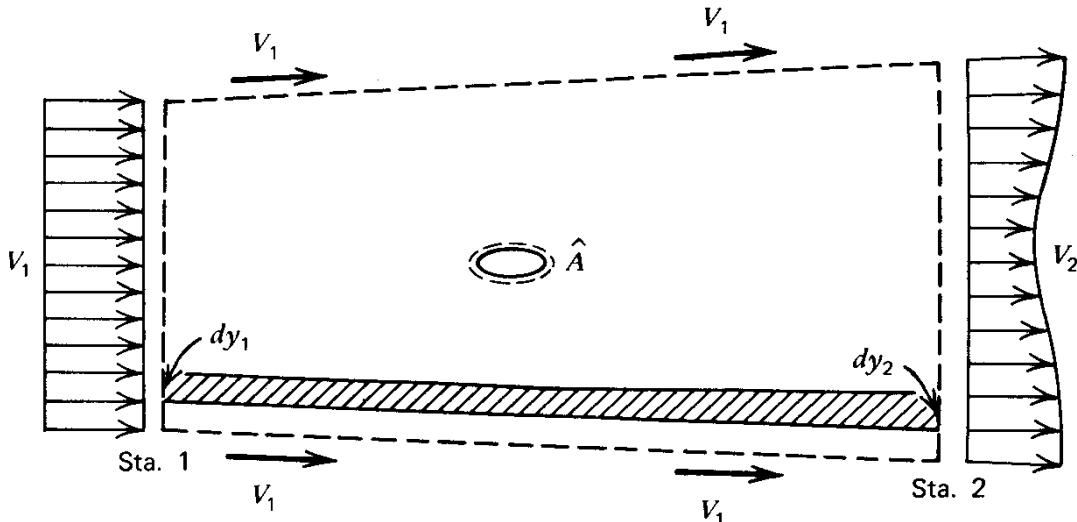
Figure 15. Velocity Profile of Body in Flowfield (Kuethe & Chow, 1986:67)

Summary

Chapter II discussed some of the current MAV technologies and engineering concepts that describe the test vehicle for this research. It also presented important information based on previous research in the areas of propeller performance, wake development and propeller/wing interaction. Finally, it presented momentum theory concepts which will be utilized to extracts force values from velocity profile measurements taken in the wind tunnel.

III. Methodology

Overview

This chapter fully describes the equipment, experimental procedures and data analysis used in the MAV propeller/wing interaction experiments. Two separate sets of experimental tests were conducted on the MAV. The first set of experiments was a static (zero freestream velocity) test of the propeller/wing/body interference characteristics with the wing in multiple positions. This test also included the loads on the wing measured by a six-component balance. The second test was conducted in the low speed wind tunnel where MAV loads along with velocity profiles were gathered using a six-component balance and a three-component hot-wire anemometer, respectively.

Test Subjects

Micro-Air-Vehicle

The baseline vehicle being tested in this experiment is the MAV shown in Figure 1. The fuselage is composed of a thin carbon fiber matrix, rectangular in shape and tapered back to a thin box-shaped tail boom. The wing, whether rigid or flexible, is high mounted on the fuselage. The control surfaces which are attached to a v-tail with a 45° mean angle, are a combination of elevators and rudder (ruddervators). In all tests, the ruddervator angles were set to zero degree deflection. The rigid and flexible wings both have the same geometric planform. The rigid wing is completely constructed of carbon fiber, whereas the flexible wing's leading edge (approximately ¼ chord length) is carbon fiber with carbon fiber ribs running the rest of the chord length of the wing. Either a

27

flexible latex or military parachute membrane is attached to the ribs to construct the rest of the wing. Table 1 lists the geometric properties of the basic MAV configuration. Figure 16 shows both the rigid and flexible wings used in this experiment.

Table 1. MAV Geometric Properties

Flexible Wing Mass	0.070 lb$_m$
Rigid Wing Mass	0.159 lb$_m$
Wing Area	93.5 in^2
Root Chord	6”
Mean Aerodynamic Chord	4.2”
Wingspan	24”
Leading Edge Thickness	0.025”
Parachute Thickness	0.005”
Aspect Ratio	6.16
MAV Length	19.25”

Figure 16. Flexible and Rigid Wings for the MAV

The propeller used in this experiment is a Graupner SUPER NYLON two-bladed propeller. It is a 6 inch diameter propeller with 3 inches of pitch, which means is should ideally advance 3 inches per rotation. Thin reflective tape is added to one blade of the propeller for RPM measurements. The propeller is shown in Figure 17.
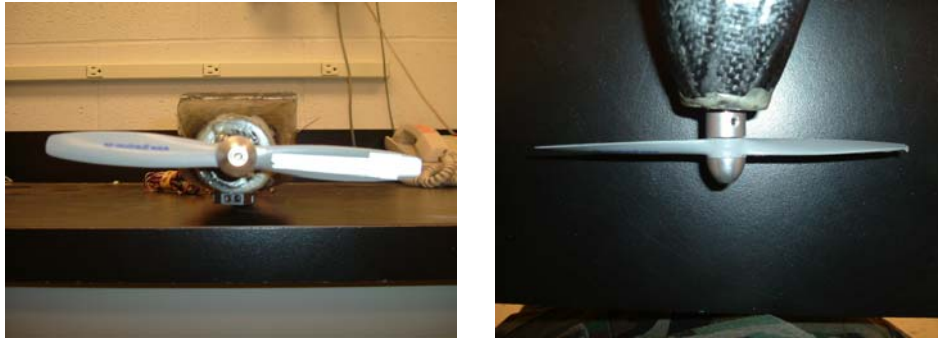
Figure 17. Graupner 6" Two-Blade Propeller

Fuselage Testbed

In order to perform a number of the propeller/wing interaction tests on the static

test stand, a plastic fuselage prototype was designed and built so the wing could be

repositioned axially without changing angle of attack. The basic dimensions of the

fuselage were taken from the original MAV with some modifications. In order to ease

the movement of the wing on the fuselage, the testbed was made in two different pieces.

The top portion follows the airfoil contour of the wing and is directly attached to the

center of the wing. The bottom portion is shaped like the original fuselage with a flat top

so the wing portion can be attached and slid forward and backward. Since the portion of

the tests that use the fuselage testbed do not include tail effects, the fuselage ends just

behind the trailing edge of the wing in its original configuration. A cylindrical hole is

located at the rear of the fuselage for mounting on the sting and balance. A tongue and

groove track system connects the top and bottom pieces. The fuselage pieces were

developed and drawn in SolidWorks® and created on AFIT's Eden 3300 rapid

prototyping machine. They are both shown in Figure 18 with the bottom portion attached

to the sting and the top portion attached to a flexible wing. The lower picture shows the

two pieces put together. More pictures of the fuselage testbed pieces can also be found in Appendix D.
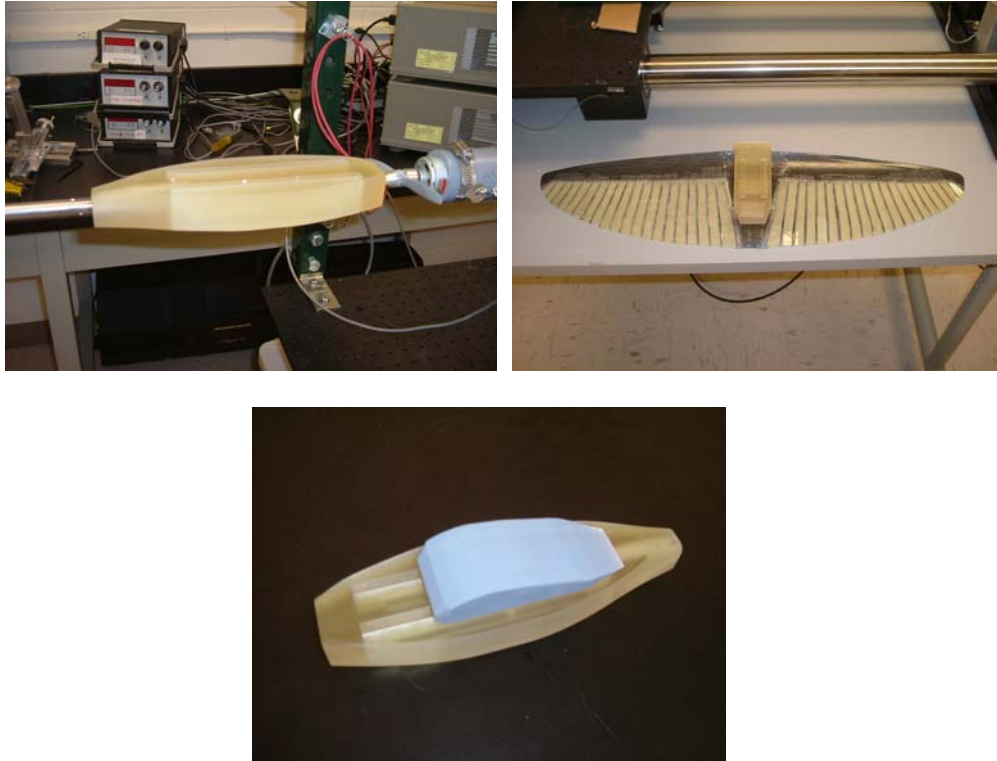
Figure 18. Rapid Prototyped Plastic Fuselage Testbed Pieces

Propeller/Wing Static Test Interaction Study

Equipment/Test Setup

The purpose of this test was to measure the propeller performance coefficients along with the loads on the wing in a static environment. In order to accomplish this, the motor and propeller had to be separated from the aircraft. To provide the proper flow across the wing, a reverse rotation electric motor was used and mounted opposite the front of the MAV. The ElectriFly T-600R (7.2-9.6V) reverse rotation electric motor was

attached to a 50 *in-oz* Lebow torque cell. The motor and torque cell were mounted to an

air-bearing table that virtually eliminates friction effects. At the end of the air-bearing

table was a 25 *lb$_f$* Interface load cell used to measure thrust. The air-bearing table was

first used by Ensign Roberto Igue (USNR) in ref. #23. An optical tachometer was also

attached to the table to provide propeller RPM data. This part of the setup is shown in

Figure 19. A close-up view of the propeller, motor and torque cell are shown in Figure

20.
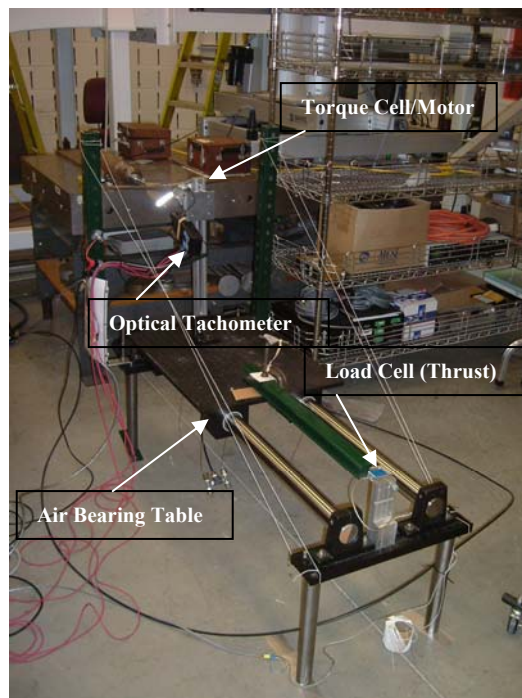
Figure 19. Air Bearing Table Setup
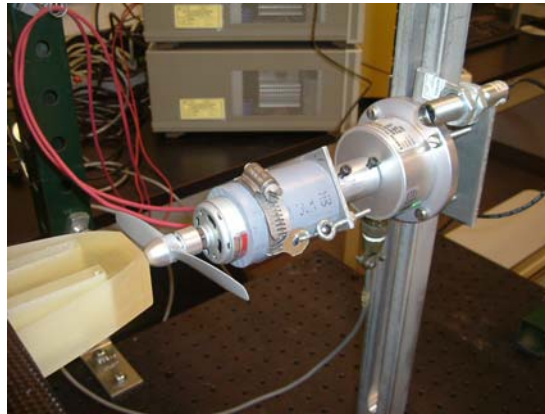
Figure 20. Propeller, Motor and Torque Cell Mount

The motor was powered by the Agilent (0-60V/0-10A) variable output power supply. This enabled the RPM of the propeller to vary with increased power to the motor. The voltage outputs from the torque cell and load cell were sent through the Vishay Measurements 2310 signal conditioning amplifier to a National Instrument BNC-2120 computer interface analog to digital converter and into a computer. The data was then captured using National Instruments Labview™.

The torque cell and load cell were both calibrated in conjunction with the signal conditioners by Mr. Andy Pitts, AFIT laboratory technician. The torque cell was calibrated by hanging known weights on a one inch moment arm attached to the shaft of the torque cell. Each weight, which corresponds to a specific torque (*in-oz*), gave a voltage output. The voltage values were then curve fit for the range of torque values expected in this experiment. The curve was linear and provided a simple relationship between voltage output and measured torque. A similar process was used with the load cell, but with the weights placed directly on the instrument. The load cell output was also linear. The data for these calibrations can be found in Appendix C.

Two different optical tachometers were used during the course of this experiment. The first was a Monarch TACH-44 digital display tachometer, which was factory calibrated and has a published accuracy of ±1 RPM. The output of this tachometer is limited to a digital display, which must be read visually. In order to automate the data collection process, a second tachometer was used which was able to output a voltage corresponding to its measured RPM. The Extech Instruments photo tachometer was also factory calibrated but has a published accuracy of only ±1.2% of the measured RPM. For this reason, the Extech tachometer was calibrated against the higher fidelity Monarch tachometer. Utilizing both tachometers, the voltage output of the Extech was compared to the digital display of the Monarch and calibrated accordingly.

On the other side of the propeller was the fuselage prototype testbed with the MAV wing attached. The fuselage was connected to the AFIT-1 six-component balance and hard mounted with a sting onto a large steel table. This part of the test setup can be seen in Figure 21. On the left side is a top view of the propeller and motor attached to the air-bearing table. On the right is the flexible wing mounted on the MAV testbed and attached to the balance.
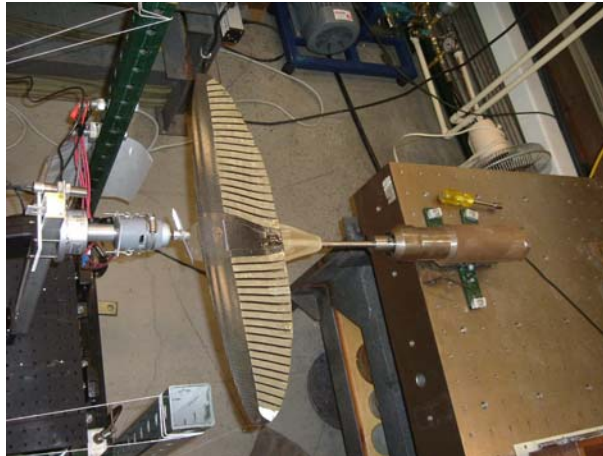
Figure 21. Top View of the Propeller Test Stand (left) and the MAV Testbed Attached to Six-Component Balance (right)

The AFIT-1 six-component balance made by Modern Machine & Tool Company was used to measure the forces and moments acting on the MAV. The balance is shown in Figure 22. The balance was mounted inside the aft end of the prototype fuselage and attached to a sting coming out of a table vice. The balance consists of multiple strain gauges. The strain gauges are a series of thin wire filaments wound in a serpentine fashion and placed in a Wheatstone Bridge configuration like that seen in Figure 23 (DeLuca, 2004:150). Voltage is continuously supplied to the gauges and as a load is applied to the wire filaments, they either elongate or shrink, thereby changing the resistance in the wires. This results in a difference in input (V_s) and output (V_o) voltage from the strain gauge.

Figure 22. AFIT-1 Six-Component Balance (Rivera Parga 2004:70)
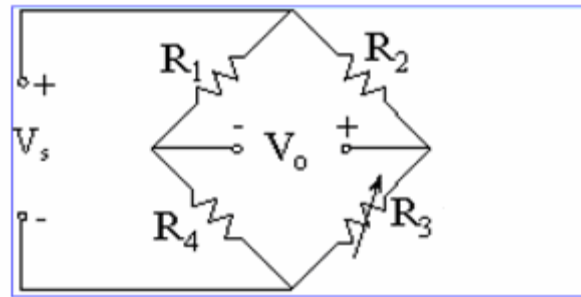
Figure 23. Strain Gauge/Wheatstone Bridge Setup (DeLuca 2004:150)

The difference in voltage is used with the manufacturer supplied strain factor (*SF*) to

calculate the wire strain (*ε*) as follows: (Rivera Parga, 2004:71)

$$\varepsilon = 4 * \frac{Vo}{Vs} * \frac{1}{SF}$$

(9)

Once the strain is found, the stress (*σ*) is calculated from Hooke's Law, where *E* is the

material modulus of elasticity.

$$\sigma = E * \varepsilon$$

(10)

Finally, the forces are calculated by multiplying the stress by the wire's cross-sectional

area and the moments are calculated by multiplying that force by the wire's length. The

force and moment outputs from the balance are collected in a Labview™ program and output in a table format for data reduction. The AFIT-1 balance has the following load limits:

Table 2. Maximum Loads for AFIT-1 Balance

Component	Maximum Load
Normal Force	10 lbs
Axial Force	5 lbs
Side Force	5 lbs
Pitch Moment	10 in-lbs
Roll Moment	4 in-lbs
Yaw Moment	5 in-lbs

Prior to testing, the six-component balance was calibrated by Mr. Dwight Gehring, AFIT wind tunnel technician, using calibrated static weights and adjusting the calibration constants in the Labview™ software so that the loads that are output on the workstation match the weights attached to the balance. Linearity was also checked by applying additional weights to each sensor and making sure the computer output increases linearly with the increased loads.

Experimental Procedure

Once all of the instruments were calibrated, the testing could begin. Prior to any power-on testing, however, a tare file was created that measured any outside forces on the wing due to atmospheric disturbances. This could potentially have an effect since the tests were conducted outside the tunnel in an open laboratory. Also, prior to every run the net forces and moments on the balance were zeroed-out so the output of the test only measured the reaction to the propeller airflow. On the motor setup the torque cell and

load cell were also set to exactly zero prior to every run. This was done with the fine tuning knob on each of the signal conditioning amplifiers.

An initial set of tests was performed to provide baseline values for power and thrust coefficients on the motor. These included full runs with the propeller only, then the addition of the prototype fuselage and finally the addition of the rigid and flexible wings in their original position. A full run consists of collecting data at multiple RPM values ranging from about 8000 to 14,000 RPM. Since the power output to the motor was controlled by a variable dial on the power supply, it was difficult to set the speed exactly to one RPM. The average RPM value was measured over the time of data acquisition and used for data analysis. The torque and load cell data were collected simultaneously at each RPM for 1000 samples at 100 Hz.

After the initial set of runs on the motor, a parametric study which included collecting both motor data and wing/MAV reaction force and moment data began. The first set of these tests were run on the flexible wing and the second on the rigid wing. The data were collected with the wing at five different axial locations and four different vertical locations from the center of the propeller. The axial distance (X_o) is measured from the front of the propeller to the leading edge of the wing and the vertical distance (Z_o) is measured from the center of the propeller hub to the leading edge of the wing. A positive Z_o value indicates the wing is above the propeller. This is shown in Figure 24. The interactions were tested at all of these locations to investigate the changes in propeller performance as well as wing reaction as a function of wing position. At each of the 20 wing locations, full data sets were collected at 4 different RPM settings with each

running for 20 to 30 seconds. The RPM values are approximate since they varied slightly

for each run. Table 3 shows the test matrix for both the flexible and rigid wings.
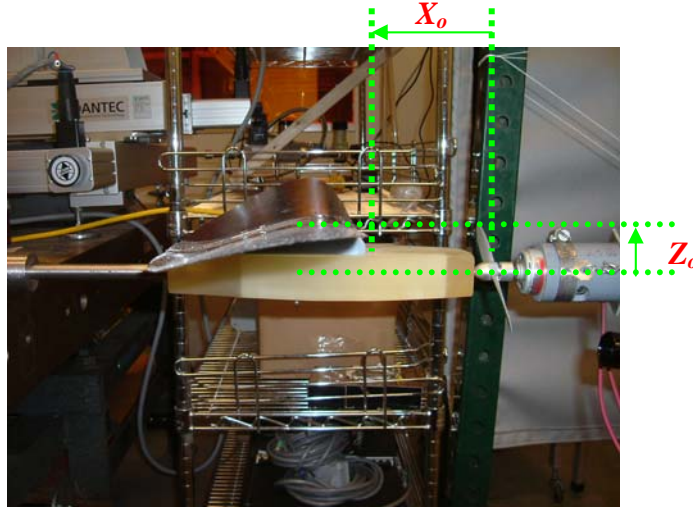
Figure 24. Wing Location with Respect to the Propeller

Table 3. Propeller/Wing Static Interaction Test Matrix

RPM 8000 10,000 12,000 14,000	Axial Position 1"	Axial Position 2"	Axial Position 3"	Axial Position 3.75"	Axial Position 4.375"
Vertical Position 1.25"	Thrust/Power Lift/Drag/ Roll Moment	Thrust/Power Lift/Drag/ Roll Moment	Thrust/Power Lift/Drag/ Roll Moment	Thrust/Power Lift/Drag/ Roll Moment	Thrust/Power Lift/Drag/ Roll Moment
Vertical Position 0.75"	Thrust/Power Lift/Drag/ Roll Moment	Thrust/Power Lift/Drag/ Roll Moment	Thrust/Power Lift/Drag/ Roll Moment	Thrust/Power Lift/Drag/ Roll Moment	Thrust/Power Lift/Drag/ Roll Moment
Vertical Position 0"	Thrust/Power Lift/Drag/ Roll Moment	Thrust/Power Lift/Drag/ Roll Moment	Thrust/Power Lift/Drag/ Roll Moment	Thrust/Power Lift/Drag/ Roll Moment	Thrust/Power Lift/Drag/ Roll Moment
Vertical Position -0.75"	Thrust/Power Lift/Drag/ Roll Moment	Thrust/Power Lift/Drag/ Roll Moment	Thrust/Power Lift/Drag/ Roll Moment	Thrust/Power Lift/Drag/ Roll Moment	Thrust/Power Lift/Drag/ Roll Moment

The test process at each of the 20 wing positions was as follows:

1. With motor off, zero out the torque cell, load cell and balance

2. Begin taking continuous balance data in laboratory control room

3. Run motor up to 8000 RPM

4. Initiate power, thrust and RPM data acquisition (1000 samples at 100 *Hz*) at separate workstation

5. Collect data for 20 to 30 seconds

6. Repeat steps 3-5 for 10,000 RPM, 12,000 RPM, and 14,000 RPM

7. Dial motor down to zero RPM and reposition wing in new location then repeat steps 1-6

A full set of data was collected for both the flexible and rigid wings for comparison. The following section discusses how the data was analyzed.

Data Analysis

For this set of tests, data were collected at two separate workstations. Torque, thrust and RPM voltage data were input into one computer, while balance output voltage was collected by another. Both used signal conditioners and analog to digital converters along with Labview™ software to collect and store the data. At each test point, torque, thrust and RPM were time averaged over a 10 second span and saved into a data file readable in Microsoft® Excel. Utilizing the calibration for each instrument, the voltages were then converted to torque (*in-oz*), thrust (*oz*) and RPM. The propeller power, *P*, was then found by multiplying torque by the rotational speed. From these values the propeller

performance coefficients were found using equations **(2)** and **(3)** from Chapter II. Recall

these equations:

$$C_T = \frac{T}{\rho \pi R^2 (\Omega R)^2}$$ **(2)**

$$C_P = \frac{P}{\rho \pi R^2 (\Omega R)^3}$$ **(3)**

Where:
C_T = coefficient of thrust
C_P = coefficient of power
ρ = air density (slugs/ft^3)
R = propeller radius (ft)
Ω = angular velocity (radians per second)

At each test point, balance data was collected for 20 to 30 seconds. This allowed

time for any vibrations due to the increase in propeller speed to settle out. It also

provided enough time to produce adequate data for time-averaged forces and moments on

the MAV. The data were stored directly into a text file under the following headings:

N1=Normal Force (lift), N2=Pitch Moment, A1=Axial Force (drag), L1=Roll Moment,

S1=Side Force, S2=Yaw Moment. Data for wind tunnel speed, angle of attack and

sideslip angle also exist in the file, but were ignored for this test. Prior to averaging the

balance data at each test point, initialization data and propeller speed transition data were

deleted. Each data file corresponding to a wing position then included 20 or more force

and moment values at the 4 RPM settings. These values were separated by RPM and

averaged in Excel to provide single values of lift, drag and roll moment. The forces were

output in *lb$_f$* and the moments in *in-lb$_f$*. Since all of this data was collected in a static

environment with no dynamic pressure ($q_\infty = 0$), aerodynamic coefficients were not calculated.

Numerous plots were developed from the propeller thrust and torque and MAV balance data. These plots are presented in Chapter IV for the purpose of characterizing differences in propeller/wing interactions based on propeller speed and wing location. Both the rigid and flexible wings were fully tested for comparison.

Wind Tunnel (Hot-Wire and Balance) Study

Equipment/Test Setup

The purpose of the second phase of testing was to further investigate the propeller effects on the MAV in the wind tunnel. This included mounting the wing(s) back on the actual MAV fuselage in their design location and placing the MAV in the AFIT low speed wind tunnel on the six-degree balance. Hot-wire measurements were taken using a triple-wire anemometer to provide velocity profiles at multiple locations about the MAV.

The AFIT nominal 3'x3' low speed wind tunnel, located in building 644 room L154, was constructed by Aerolab. It is an open circuit wind tunnel that draws in air from within the room. It has a design speed of 150 *mph* and has been tested at 148 *mph*. A schematic of the wind tunnel is shown in Figure 25.

Figure 25. AFIT Low Speed Wind Tunnel Schematic (DeLuca, 2004:26)
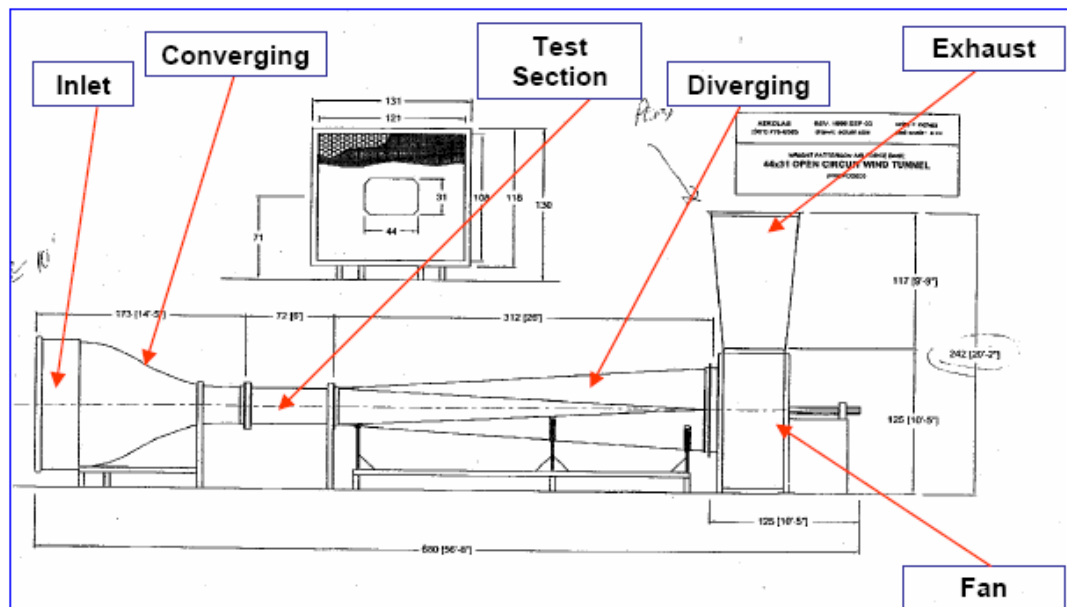
Air is sucked-in through the inlet where four steel mesh anti-turbulence screens and an aluminum honeycomb straighten the flow. It is then sent through an 8' long converging section where the contraction ratio is 9.5:1. The test section measures 72" long by 44" wide by 31" high. The top and sides of the test section are constructed of Plexiglas and can be removed for test section access. The top section is slotted to allow the hot-wire probe access to the flow. It can be seen in Figure 26. The plate consists of one centrally located slot down the x-axis of the tunnel and six equally spaced openings across the y-axis. This limits the number of locations that the hot-wire can be placed in relation to the MAV during testing.
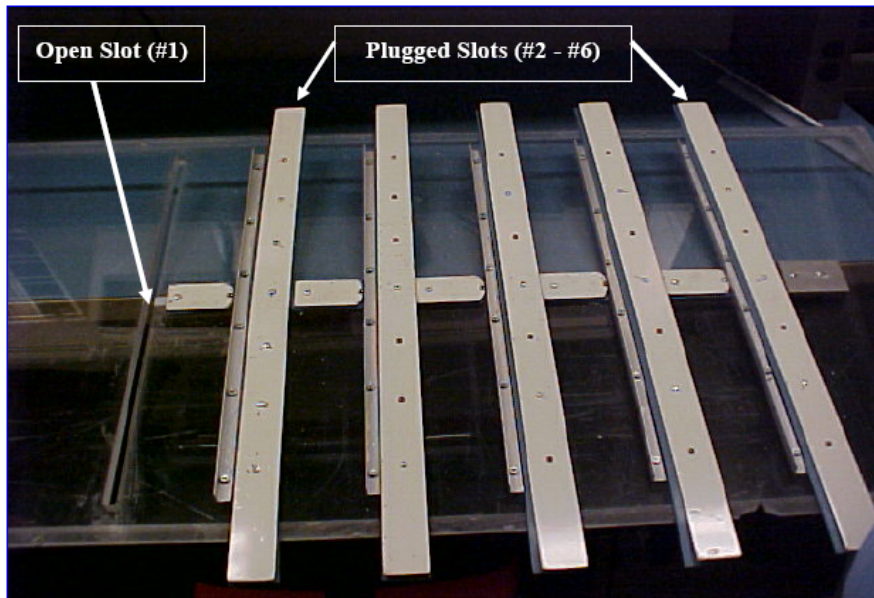
Figure 26. Plexiglas Slotted Tunnel Top Section (DeLuca, 2004:20)

Once air passes through the test section, it is then sent through a long diverging section to the fan, where it is exhausted 90° toward the ceiling of the room. The wind tunnel utilizes a 200 BHP Toshiba motor that has a maximum operating speed of 1785 RPM.

The same AFIT-1 six-component balance used in the propeller/wing interaction study was used in the wind tunnel. It was attached to a permanent sting support system that enters the test section from the bottom of the tunnel. The support system is able to move the test subject ±20° angle of attack and ±15° sideslip angle. For this test, the sting was kept in its neutral position. The test section is shown in Figure 27. It includes the sting with the balance mounted on the sting support and the hot-wire probe extending in from the top of the tunnel.
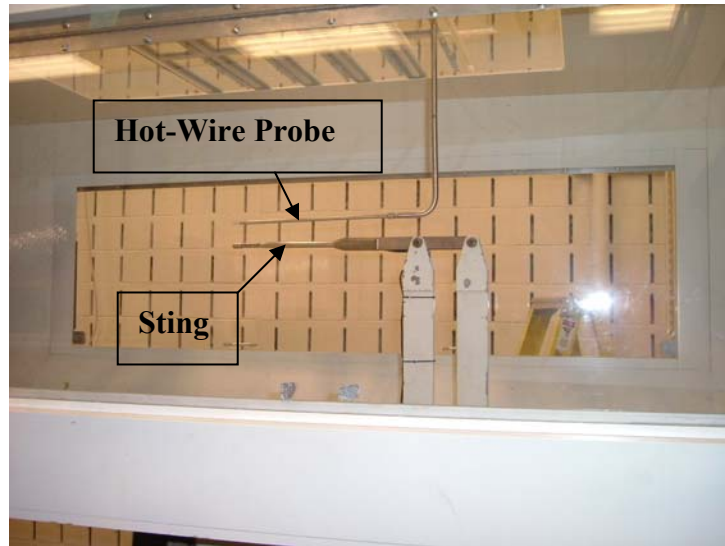
Figure 27. AFIT Wind Tunnel Test Section with Hot-Wire Probe and Balance Sting

In order to provide velocity profiles around the MAV, a Dantec Dynamics Streamline 55P91 tri-wire anemometer was used. It provided velocity measurements in all three axes (u,v,w) with respect to the tunnel. The three components are important when studying the three-dimensional flowfield created by the propeller. The tri-wire is shown in Figure 28. It consists of three mutually perpendicular gold-plated wire sensors with a diameter of 5 μm and length of 1.25 mm that lie within a 3 mm sphere (dantecdynamics.com). Its nominal velocity limits are 0.05 m/s to 200 m/s.
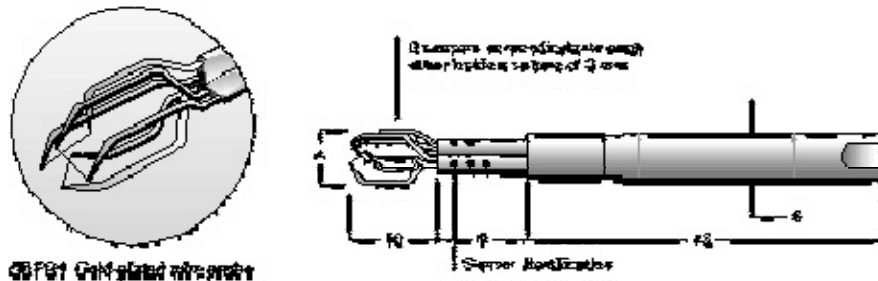
Figure 28. Dantec 55P91 Triple Wire Anemometer (dantecdynamics.com)

This was the first time this triple wire system had been used at AFIT and it had to be calibrated. Mr. Dwight Gehring and Capt Brian Gamble performed the calibration. Dantec Dynamics produces calibration instruments to aid in the process. The Dantec Dynamics Streamline 90H02 Flow Unit Calibration System was used to calibrate the tri-wire. The wire was mounted normally in front of a nozzle that uses compressed air to provide factory calibrated velocities across the hot-wire. The accuracy of the calibrator is advertised at ± 0.02 *m/s*. The velocity across the wire was increased in small increments over the operating range of the tunnel. The data was collected by Dantec's Streamware[®] software and fed into a calibration algorithm. After the initial calibration routine, a directional calibration was performed. For this calibration, flow velocity remained constant while the probe was set to a fixed inclination angle of 30° and rotated through 360° in 15° increments. The *u*, *v* and *w* components of velocity are found in the software by the following equations:

$$u = U_1 \cos 54.736 + U_2 \cos 54.736 + U_3 \cos 54.736$$
$$v = -U_1 \cos 45 - U_2 \cos 135 + U_3 \cos 90 \qquad \textbf{(11)}$$
$$w = -U_1 \cos 114.094 - U_2 \cos 114.094 - U_3 \cos 35.264$$

Where U_1, U_2 and U_3 are found by the following set of equations:

$$U_{1eff}{}^2 = k_1{}^2 U_1{}^2 + U_2{}^2 + h_1{}^2 U_3{}^2$$
$$U_{2eff}{}^2 = h_2{}^2 U_1{}^2 + k_2{}^2 U_2{}^2 + U_3{}^2 \qquad \textbf{(12)}$$
$$U_{3eff}{}^2 = U_1{}^2 + h_3{}^2 U_2{}^2 + k_3{}^2 U_3{}^2$$

Where U_{1eff}, U_{2eff} and U_{3eff} are the effective cooling velocities acting on the three hot-wire sensors and k_i and h_i are the yaw and pitch factors found during calibration (Streamline[®]

Reference Manual, 8.11). The results of these calibrations along with the hot-wire error

analysis can be found in Appendices C and E.

Following calibration, the tri-wire was mounted to a probe that extends down

from the top of the tunnel through the open slots and was attached to a Dantec fully

automatic and programmable traversing system. This allows the probe to automatically

move precisely throughout the tunnel during testing without having to interrupt the test.

The traversing system is shown in Figure 29.
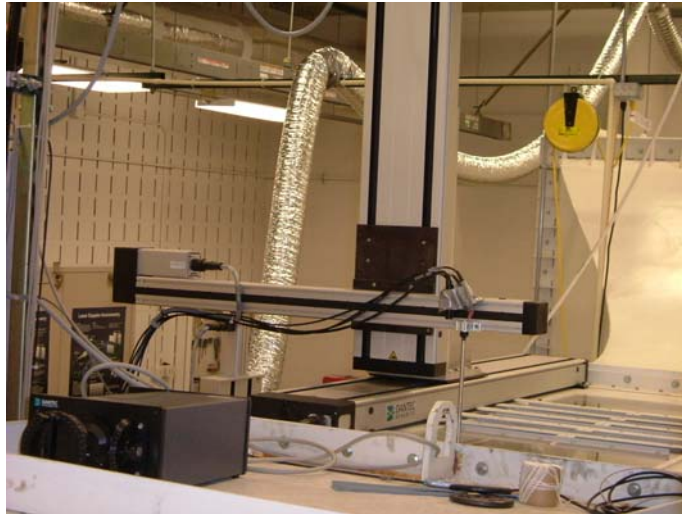
Figure 29. Hot Wire Traversing System

Experimental Procedure

Prior to starting the first set of tests in the wind tunnel, the hot-wire and balance

were fully calibrated. Also, the hot-wire had to be mounted properly and set in the

traversing machine so test grids could be developed. With the probe entering the tunnel

through the farthest aft slot of the tunnel top, the tip of the hot-wire was located

approximately 1" aft of the trailing edge of the flexible wing at the root chord location.

This was the axial location of the hot-wire for nearly all of the testing. The hot-wire was mounted perpendicularly in the tunnel so oncoming tunnel flow was coincident with the *u*-component of the wire.

Once the hot-wire was properly mounted, a zero-point was set for the traversing machine. It was set as far out on the left wing as the slot would allow and just over 3" below the trailing edge of the wing. From this point, test grids were developed for velocity data acquisition. Five separate grids were built in order to work the probe around the sting and tail of the MAV. Two large grids, one on each side of the wing, were developed to span 180 *mm* up and 140 *mm* across. The traversing machine uses metric units and data was taken at 10 *mm* increments. These grids spanned into the center until the probe was aligned with the outside of the v-tail. Two smaller grids were then developed to cover the underside of the v-tail and one more grid covered the area above the v-tail. Due to the physical constraints of the v-tail and the sting, data was not collected at three small areas near the center of the MAV. This was a limitation of the experiment that could be improved upon with a smaller hot-wire probe in future work. Data from these five grids provided a velocity profile for most of the wing. The outer part of the wing could not be reached with the given tunnel configuration unless the hot-wire probe was rotated about the *z*-axis. Therefore to provide velocity data at the wingtip, the probe was rotated 18.5° and another grid was made to cover the outer section of the wing. Figure 30 shows a representative sketch of the grids used during this test.
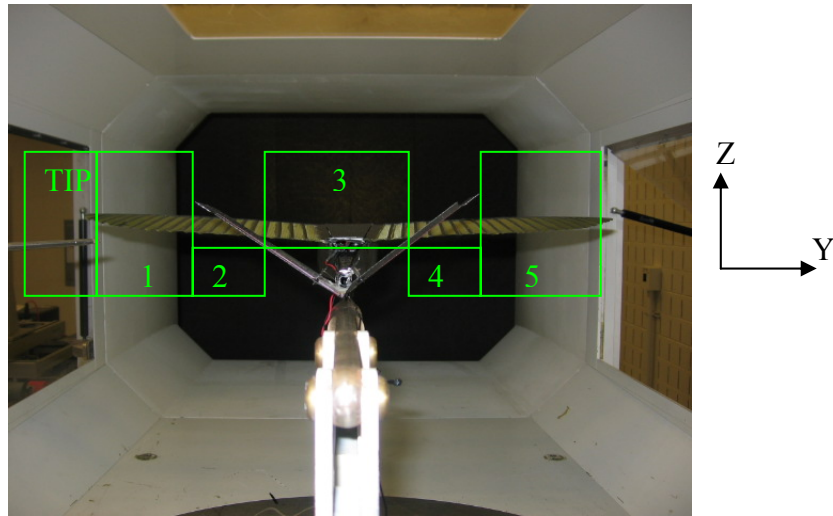
Figure 30. Hot-Wire Test Grids from Aft View of MAV Inside Wind Tunnel

Since some of the velocity data being collected during this part of the test was

being used for a momentum balance, numerous configurations had to be tested. Velocity

and balance data were collected for multiple combinations including nominal tunnel

speeds of 0, 20, and 30 *mph* and with or without the propeller running at 8000 RPM.

Prior to the first test, a tare file was collected on the balance and the balance values were

zeroed out. From this point, the tunnel was started up and set to run at a nominal 20 *mph*.

This corresponds to a Reynolds number of about 8.5 x 10^4. The propeller was taken off

of the MAV for the non-powered runs. As the hot-wire was taking velocity data, the

balance was measuring the MAV's forces and moments. Running through the five

traversing grids took almost 90 minutes from start to finish with the propeller motor off.

The grids were traversed automatically with the Dantec software, however each of the

grid's start points had to be selected manually between runs. This test was repeated at a

nominal 30 *mph*, which corresponds to a Reynolds number of about 1.3 x 10^5. Then the

propeller was reinstalled and data was collected at the nominal 20 *mph* and 30 *mph*

48

settings with the propeller running at 8000 RPM. The test was also performed with only

the propeller running and no freestream velocity. With the length of the run times for the

traversing grids, the MAV motor would get hot and needed to be cooled between test

runs. The motor was cooled with compressed air so it would not overheat during a test.

This extended the test time considerably. Since the carbon fiber fuselage is completely

enclosed at the front of the MAV, no cooling air reached the motor during testing or

flight. This is something that should be corrected for future tests.

Once all of the tests were completed with the flexible wing on, it was removed

and the same tests were conducted with the wing off. These were accomplished to

provide velocity profile differences caused by the wing and utilized in the momentum

balance to find thrust and drag. The same tests were then performed on the MAV with

the rigid wing attached for comparison to the flexible wing. Table 4 shows the test

matrix for the wind tunnel study.

Table 4. Wind Tunnel (Hot-Wire/Balance) Test Matrix

MAV CONFIGURATION	TUNNEL SPEED (Nominal)	PROPELLER MOTOR
Flexible Wing	20 mph	Off
Flexible Wing	30 mph	Off
Flexible Wing	20 mph	8000 RPM
Flexible Wing	30 mph	8000 RPM
Flexible Wing	Off	8000 RPM
No Wing	20 mph	Off
No Wing	30 mph	Off
No Wing	20 mph	8000 RPM
No Wing	30 mph	8000 RPM
No Wing	Off	8000 RPM
Rigid Wing	20 mph	Off
Rigid Wing	30 mph	Off
Rigid Wing	20 mph	8000 RPM
Rigid Wing	30 mph	8000 RPM
Rigid Wing	Off	8000 RPM

Data Analysis

For the wind tunnel tests, data was collected at two separate workstations. The

Dantec Streamware® software collected all of the raw hot-wire data. This data was

collected at 1000 *Hz* and reduced in the software program using the calibration developed

previously. Each traversing point collected roughly five seconds of data which was time-

averaged in the Dantec software and presented in a text file which gives position (*x, y, z*)

in traversing coordinates, the average *u*, *v*, and *w* velocity components in *m/s* and their

respective standard deviations. All of this data was then saved to disc and available to be manipulated in other software. The files were opened in Microsoft® Excel and manipulated for graphical purposes. This included shifting all of the coordinates among the test grids to a common zero point. The center of the MAV represented the zero in the *y*-direction, while the lowest point of the traverse was used as the zero in the *z*-direction. Also, the sign of the spanwise velocity component was switched to match the coordinate system. The wingtip velocity data was transformed to account for the 18.5° rotation in the hot-wire probe. All of the grids were combined for each different test and plotted in Tecplot®. These plots are presented in Chapter IV.

Balance data was collected and processed in Labview™ and stored to file. It included tunnel speed, angle of attack and sideslip angle along with the forces and moments. The files were cleaned of any extraneous data and read into a MATLAB® program developed by Capt DeLuca and Lt Gebbie (Gebbie, 2005:113). The code was used to correct for tunnel specific properties as well as balance sensor interactions. Details of the program can also be found in Appendix D, pages 95-106 of Leveron (ref. #29). The balance data was used primarily to provide total axial force for the momentum balance. With the propeller running, this includes both thrust and drag. With the motor off, axial force represents drag on the MAV only. The *u*-component of the velocity from the hot-wire data was also used from various test runs in the momentum balance. The difference in the velocity for multiple configurations integrated over the surface of the test space was used to estimate drag. The results of the momentum balance are discussed in detail in Chapter IV.

Summary

Chapter III presented the equipment, test subjects, experimental procedures and data analysis used in both the static propeller/wing interaction study and the wind tunnel study. Photographs helped to provide a clear understanding of each test setup and test matrices showed the extent of the data collection process. All of the tests described in this chapter were successfully completed and their results are presented in Chapter IV.

IV. Analysis and Results

Overview

This chapter details the results of the propeller/wing interaction tests performed with the static test arrangement and the wind tunnel tests. The results of the static tests demonstrate how placing the wing in different locations affects the forces and moments acting on the motor and on the airframe. Graphical representations help illustrate the performance tradeoffs. Velocity profiles taken in the wind tunnel graphically show the freestream flowfield along with the propeller wake and how they interact with the MAV. The surface integral of the velocity is used to compute the momentum downstream of the as-configured MAV wing for both propeller-off and powered conditions. These results are compared to values measured with the wind tunnel balance. Lastly, results from the static tests and wind tunnel tests are compared and analyzed.

Propeller/Wing Static Test Interaction Results

The data presented for this study includes propeller thrust and torque along with MAV lift, drag and roll moment. A representative set of data for a single speed, 10,000 RPM, is included in Table 5 which shows the actual forces at multiple flexible wing locations. The data shows how the drag and roll moment stay relatively constant until the wing is very close to the propeller where they both increase. Also the lift created by the propeller is nearly zero until the propeller is raised above the wing, at Z_o=-0.75". Propeller thrust remains fairly constant as wing position changes at the 10,000 RPM case. Torque increases slightly as the wing moves closer to the propeller, but the wing effect is

more strongly tied to changes in the vertical positioning. Similar results for the other

speeds and the rigid wing are included in tabular form in Appendix A.

Table 5. Propeller/MAV Forces and Moments at 10,000 RPM (Flexible Wing)

Axial Separation X_o (in)	Vertical Separation Z_o(in)	Lift (lb$_f$)	Drag (lb$_f$)	Roll Moment (in-lb$_f$)	Thrust (lb$_f$)	Torque (in- lb$_f$)
4.375	1.25	0.003	0.041	0.071	0.364	0.187
3.75	1.25	-0.001	0.039	0.070	0.359	0.187
3.00	1.25	-0.004	0.041	0.070	0.361	0.190
2.00	1.25	-0.004	0.042	0.068	0.360	0.192
1.00	1.25	0.002	0.050	0.075	0.361	0.191
4.375	1.25	0.003	0.041	0.071	0.364	0.187
4.375	0.75	-0.001	0.042	0.086	0.333	0.194
4.375	0	0.013	0.047	0.088	0.350	0.194
4.375	-0.75	0.022	0.039	0.052	0.336	0.190

Non-dimensional values are useful when comparing two different test conditions.

The non-dimensional values are given as drag/thrust (*D/T*), roll moment/motor reaction

torque (ℓ/Q) and lift/drag (*L/D*). The first set of plots shows all of the non-dimensional

values for the different flexible wing locations at the four RPM settings. In each of these

plots, the *x*-axis shows the axial distance between the wing and propeller and the different

lines represent the height of the leading edge of the wing with respect to the propeller,

where negative values indicate the wing below the propeller. The 'blue dash-dot' line at

X_o=4.375" represents the current design location of the wing on the MAV. The contour

plots also provide a color representation of the different values at the 10,000 RPM

setting.
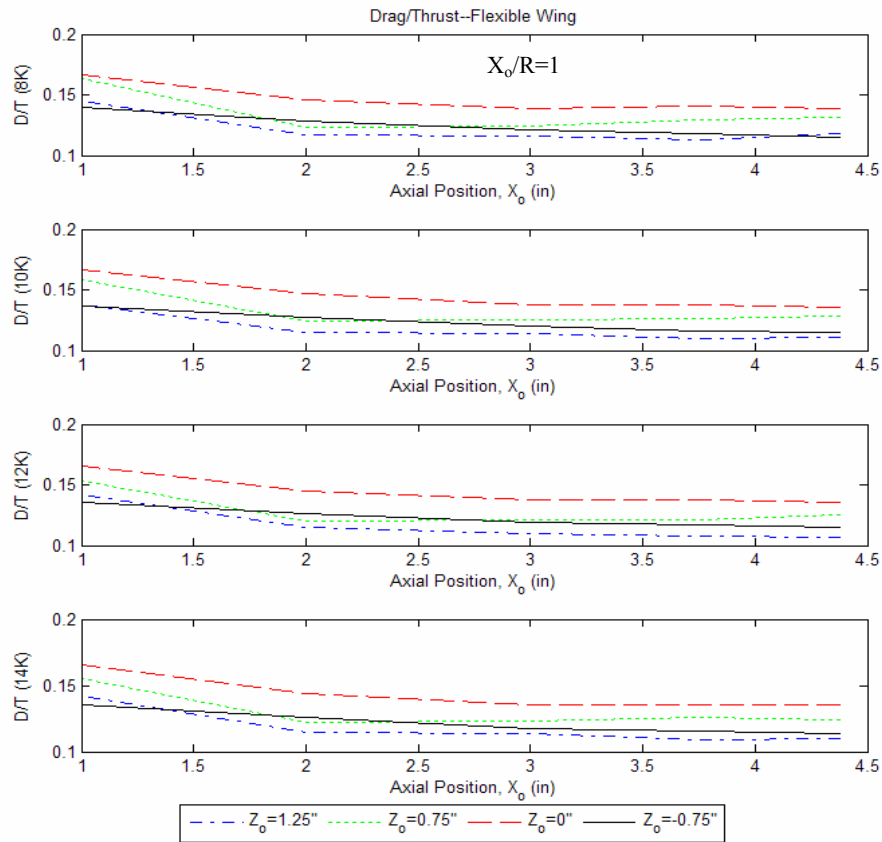
Figure 31. Drag/Thrust Curves at Multiple Wing Locations (Flexible Wing Root Chord=6", Propeller Radius=3")

The first thing to notice on the drag/thrust curves is that the non-dimensional values and trends remain relatively constant over the entire speed range (8000-14,000 RPM) as indicated by 8K, 10K, 12K and 14K in the y-axis title. Note that the y-axis range is 0.1 to 0.2 for each plot. As the axial distance between the propeller and wing decreases from 4.375" to 2" (1.46R to 0.67R), the drag/thrust changes very little. However, a notable increase in drag/thrust occurs when the wing is moved closer than 2" (0.67R) from the propeller. The flatness of the curves in the 4.375" – 2" range indicates that moving the wing forward will not increase the drag/thrust ratio for the zero

freestream condition. As the wing moves down in the Z_o-direction, the drag/thrust

increases until the wing is level with the propeller then begins to decrease again as the

wing is lowered below the centerline of the propeller. This indicates a maximum drag

condition when the height of the propeller hub is equal to the leading edge of the wing.

This is a reasonable result since at this point the maximum amount of the propeller wake

is affecting the wing of the MAV. Figure 32 is a contour map of the drag/thrust for the

10,000 RPM case, but is representative of all speeds. The shape of the map is dominated

by changes in drag, as thrust changes only a small amount over the entire region. Again,

positive Z_o values indicate the wing is above the propeller. It is easy to see that the

farther the wing is away from the propeller, both in the X_o and Z_o directions, the less drag

per unit thrust on the MAV. Note, however, that the range of values is 0.115 to 0.165,

which shows up to a 43% change.
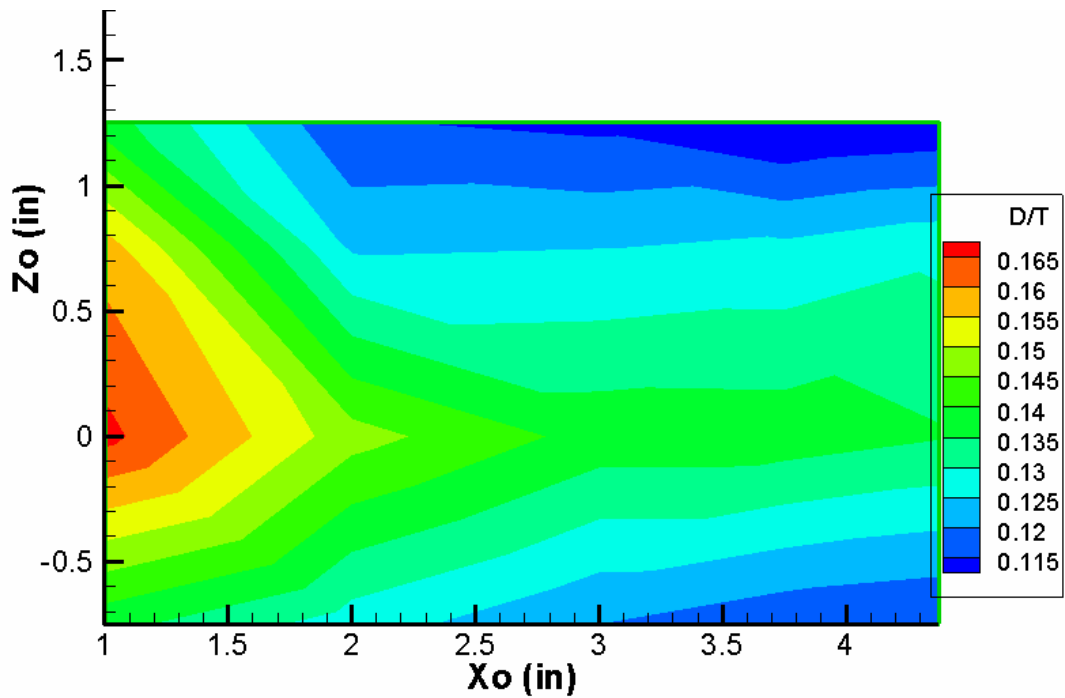
Figure 32. Contour Map of Drag/Thrust at 10,000 RPM, Multiple Wing Locations (Flexible Wing Root Chord=6", Propeller Radius=3")

The next non-dimensional value of importance is the roll moment/motor reaction torque of the MAV. This value represents the amount of roll induced by the propeller wake on the wing over the reaction torque of the motor. Like the drag/thrust term, these act in opposite directions. The roll moment on the MAV caused by the propwash actually counters the torque produced by the motor. In effect, the wing tends to straighten-out the rotational flow caused by the propeller wake. Figure 33 shows the roll moment/torque measurements collected over the range of propeller speeds for multiple wing positions.
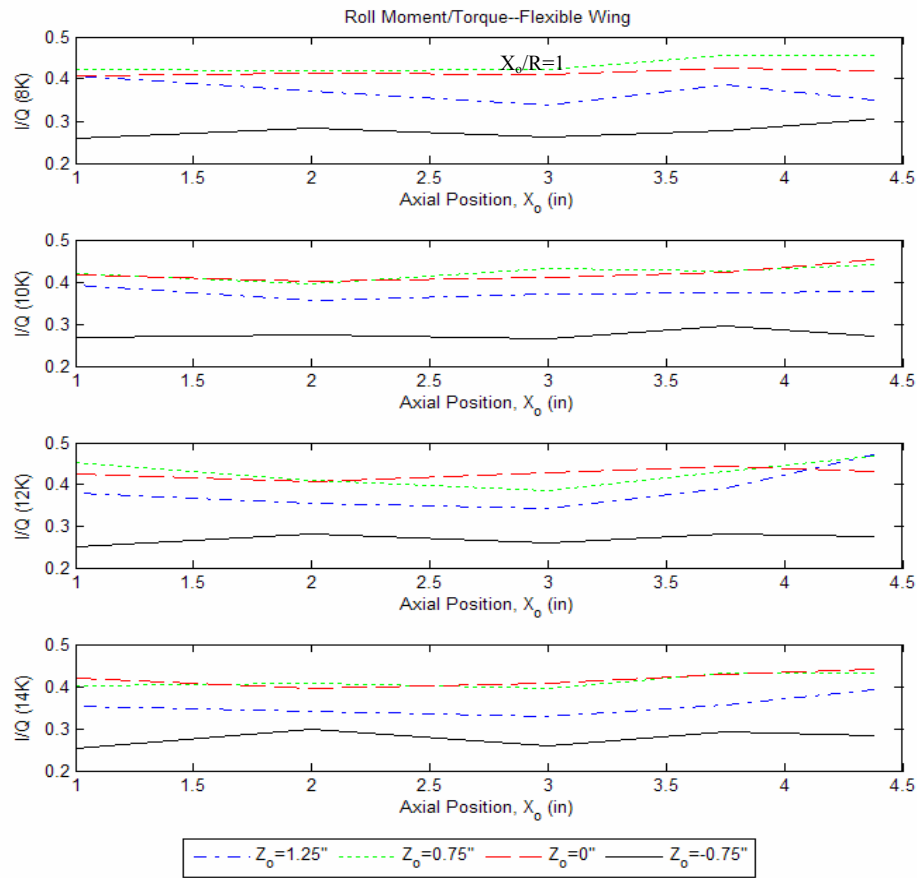
Figure 33. Roll Moment/Torque Curves at Multiple Wing Locations (Flexible Wing Root Chord=6", Propeller Radius=3")

Unlike the drag/thrust curves, the roll moment/torque curves change slightly for different RPM settings. At the design wing location (X_o=4.375", Z_o=1.25"), as the speed of the propeller increases from 8000 to 12,000 RPM, as signified by 8K, 10K and 12K, the roll moment/torque increases from about 0.35 to 0.48 then falls off to 0.39 at 14,000 RPM. Focusing on the wing location vs. roll moment/torque, there is not a large change as the wing moves axially toward the propeller in most cases. By contrast, the vertical location of the wing has a strong influence.

In general, a high value of roll moment/torque is desired since it tends to reduce the amount of motor induced roll on the aircraft during flight (av8n.com). With this argument, the optimal height for the wing would be level with the center of the propeller, indicated by the 'dashed red lines' in Figure 33. Again this is a sensible conclusion since the maximum propeller wake effect on the wing occurs at this point. There is then a design tradeoff between a low drag to thrust ratio and a high roll moment to torque ratio depending on the height of the wing with respect to the propeller. There is no obvious trend as the wing is moved toward the propeller. At some heights, roll moment/torque increases slightly and others it decreases slightly or stays fairly constant. These variations could also be due to instrument or measurement errors, which can be up to $\pm 6\%$ of the presented value. Further error analysis is shown in Appendix E. Figure 34 is a contour map of roll moment/torque that shows most variations occur in the Z_o-direction. The range of values is between 0.27 and 0.45. In this figure, the 0.43 to 0.45 (dark red) region indicates the highest roll moment/torque ratio. In this region the amount of torque that is counteracted by the wing is nearly 45% at 10,000 RPM.
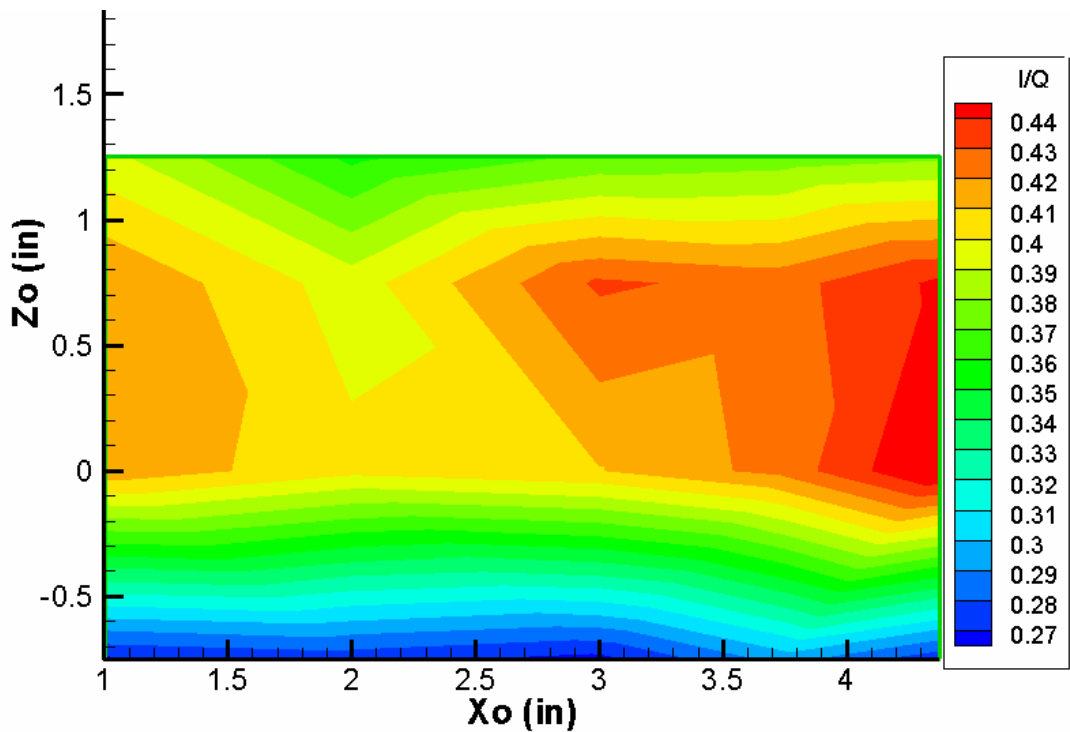
Figure 34. Contour Map of Roll Moment/Torque at 10,000 RPM,Multiple Wing Locations (Flexible Wing Root Chord=6", Propeller Radius=3")

The lift created by the propeller wake is very small in most cases when the propeller is mounted in the center of the fuselage. This is because the upwash acting on one side of the wing is countered by the downwash acting on the other side. Depending on the height of the wing however, lift can be positive due to the propeller wake if the net axial component of the velocity over the top of the wing is greater than over the bottom. Figure 35 shows the lift to drag ratio for the MAV at multiple wing locations. The value for lift/drag in most cases is negligible and should not affect design considerations. Only when the wing is mounted below the propeller (Z_o=-0.75") does the lift to drag ratio become large enough to make a difference in flight.
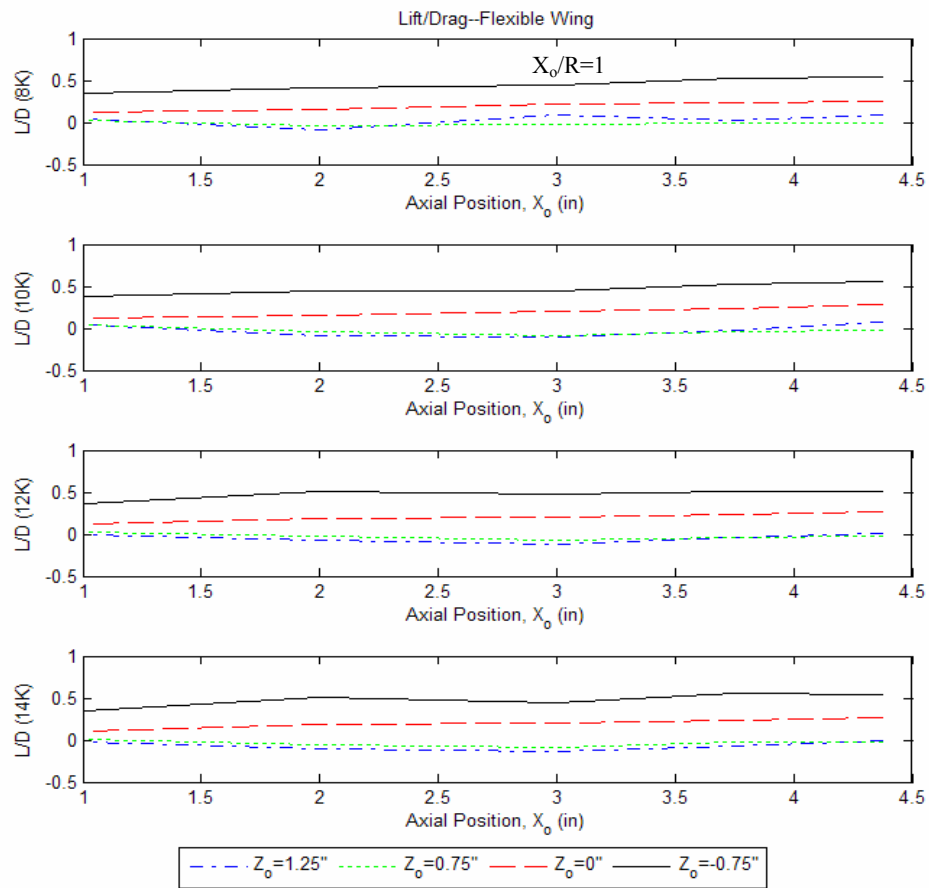
Figure 35. Lift/Drag Curves at Multiple Wing Locations (Flexible Wing Root Chord=6", Propeller Radius=3")

Looking at propeller and motor performance coefficients also provides some interesting results. Figure 36 shows the propeller thrust and torque coefficients as items are added to the flow at multiple RPM settings. The measurements were taken with the propeller only, the propeller and the fuselage only, then with the addition of the wing in three different axial locations. The coefficient of torque (C_Q) and the coefficient of thrust (C_T) both increase as the fuselage and then the wing are added to the flow. C_Q increases by about 2% and C_T by about 7% when the wing is added to the flow, which reflect the

results found by Fratello (ref. #17) in Figure 12 of this document. Both coefficients also increase as the wing moves closer to the propeller. This indicates an increase in power required to keep the motor at a certain RPM as the wing is introduced into the flow. This is an important consideration along with the non-dimensional findings in Figure 33. Moving the wing closer to the propeller while maintaining the same propeller speed not only decreases the roll moment to torque ratio, but also increases the power draw from the motor. It also increases the amount of thrust produced by the propeller which could be used as a design tradeoff.

If propeller speed is allowed to change in order to maintain thrust, the outcome is slightly different. For example, looking at the flexible wing at X_o=4.375" and 10,000 RPM in Figure 36, the coefficient of thrust is 0.113. This equates to a thrust of 5.8 *oz*. In order keep this same amount of effective thrust when the wing is moved forward to X_o=1" while still accounting for the increased drag to thrust ratio found in Figure 31, the useful net thrust would have to be 5.98 *oz*. With a coefficient of thrust at X_o=1" from Figure 36 of 0.0119, the required speed of the propeller to maintain the same thrust is reduced to 9907 RPM. This actually reduces the amount of power required by almost 2%.
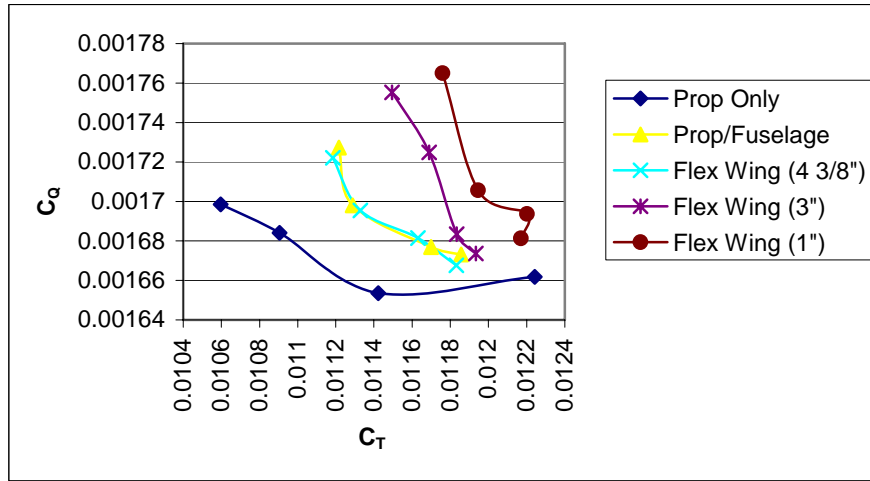
Figure 36. Propeller Thrust and Torque Coefficients

The average figure of merit for each condition also changes slightly. Figure of merit shows the relative efficiency of the propeller under zero freestream velocity conditions. Table 6 shows figure of merit values for each of the cases in Figure 36 along with the values found when testing the rigid wing. As the wing is added to the flow and subsequently moved closer to the propeller, the figure of merit increases. Figure of merit is defined by $(C_T^{3/2}/(2^{1/2}C_Q))$ for this static test (ref. #26) and both coefficients increase as the wing moves toward the propeller, making the propeller slightly more efficient. Thrust and torque measurements for the rigid wing compared closely to the flexible wing leading to similar figure of merit values.

Table 6. Figure of Merit for Multiple Configurations

CONFIGURATION	FIGURE OF MERIT
Propeller Only	0.525
Propeller and Fuselage	0.526
Flexible Wing (4.375")	0.525
Flexible Wing (3")	0.536
Flexible Wing (1")	0.556
Rigid Wing (4.375")	0.531
Rigid Wing (3")	0.540
Rigid Wing (1")	0.561

One important finding from the zero freestream propeller/wing interaction study is that at the MAV design wing location, the average drag to thrust ratio is 0.111 and the average roll moment to torque ratio is 0.398. Also, there is no reason based on the independent propeller/MAV reaction measurements that the wing on the MAV could not be slightly repositioned to potentially improve its stability. For example, at 10,000 RPM, moving the flexible wing 0.46R closer to the propeller causes the thrust to decrease by 1% and the torque to increase by 1.6%. The drag remains the same and the roll moment decreases by about 1.4%.

All of the tests performed on the flexible wing were also done on the rigid wing for comparison. For most cases, the drag was usually between 2% and 7% higher for the rigid wing, increasing with RPM as seen in Figure 37. Figure 37 includes a drag comparison for the rigid and flexible wings at X_o=4.375" and X_o=1". Thrust was only slightly higher for the rigid wing at higher RPM values and the plot is shown in Appendix A. On the other hand, the MAV roll moment was usually higher with the rigid wing at the lower RPM values and lower at the higher RPM values than with the flexible wing,

with torque values remaining about the same for the each wing. There is no overall trend when comparing the roll moment and torque for the rigid and flexible wings. Results show that the non-dimensional values of drag/thrust, roll moment/torque and lift/drag for the rigid wing are similar to that of the flexible wing for the zero freestream velocity case. Therefore, they are not described further in the body of the text but rather are shown in Appendix A for comparison.
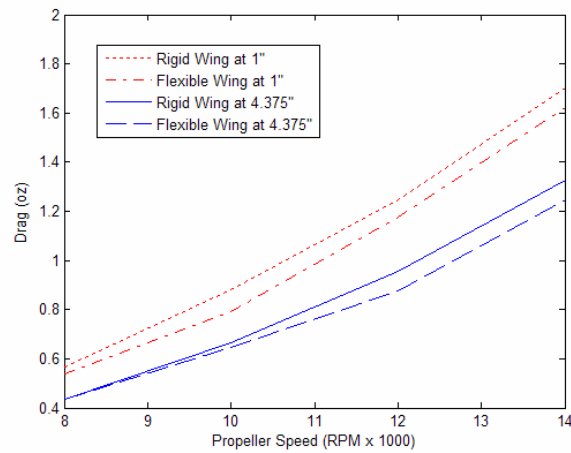
Figure 37. Rigid Wing and Flexible Wing Drag Comparison (8K to 14K RPM)

Wind Tunnel (Hot-Wire and Balance) Results

Data for the tests conducted in the wind tunnel include all three components of velocity and reaction forces and moments on the MAV. For the first part of the analysis, color contour maps of each of the different test are presented. In each of these plots, the point of view is looking at the MAV from behind as seen in Figure 30. Most of the plots include all five grids put together to depict the entire flow. A few of the plots also include the wingtip velocity on the left side of the MAV. All of the velocity components are presented in *m/s*. On the contour plots, the color map represents the positive *u*-

component or tunnel velocity moving across the hot-wire. The black arrows show the v and w velocity vectors acting in the cross-stream directions. Each legend shows a representative 1 *m/s* length vector. The w or up-down component of the velocity acting in the z-direction is slightly skewed, showing a downward component that is most likely due to the imperfection in the mounting of the hot-wire probe. Since the end piece of the probe is long, greater than 12 inches, it has a very slight downward angle to it that could not be physically overcome. It drops about 1/16" over the 12" length, which is about 0.3°, but is enough to show a slight discrepancy in the w-component. This could be overcome by using a shorter probe in the future. The white areas of the contour plots indicate areas unable to be tested due to probe interference with the sting and tail. Instead of graphically interpolating across the blank spots, they are blocked out to avoid any confusion.

During the different test runs, the tunnel velocity was set in the control room to a specific motor RPM and measured using the installed pressure taps in the tunnel test section. With the propeller running, however, the pressure taps indicated a difference in the tunnel velocity. In an attempt to keep the freestream velocity constant over multiple test runs, the motor RPM was set to a specific speed each time. This worked quite well for most of the tests, but some of the hot-wire velocity data showed a slight freestream discrepancy (less than 4%) between test runs. This is corrected in the momentum balance, but not in the graphical presentation.

Propeller-Only, Zero Freestream Velocity Profiles

The first set of plots shows propeller-only results with the tunnel motor off. The propeller is set to 8000 RPM. Figures 38 – 40 show velocity profiles for the no wing, flexible wing and rigid wing cases. In Figure 38 where the wing is removed from the fuselage and only the propeller wake is shown acting around the fuselage, the rotational flow is easy to see. It appears to be shifted slightly to the right of the centerline of the MAV, which is most likely due, in part, to the mounting of the propeller, which is not perfectly square with the fuselage. This shows up in all of the tests where the propeller is running. From the aft view of the MAV, the propeller wake rotates clockwise and reaches axial velocities of 8 *m/s*. The axial velocity component is strongest at a point above and to the right of the center of the propeller and decays outward in a radial fashion. Interestingly, at the axial plane of the test which is more than 11" aft of the propeller, the diameter of the propwash is only about 25% larger than the diameter of the actual propeller.
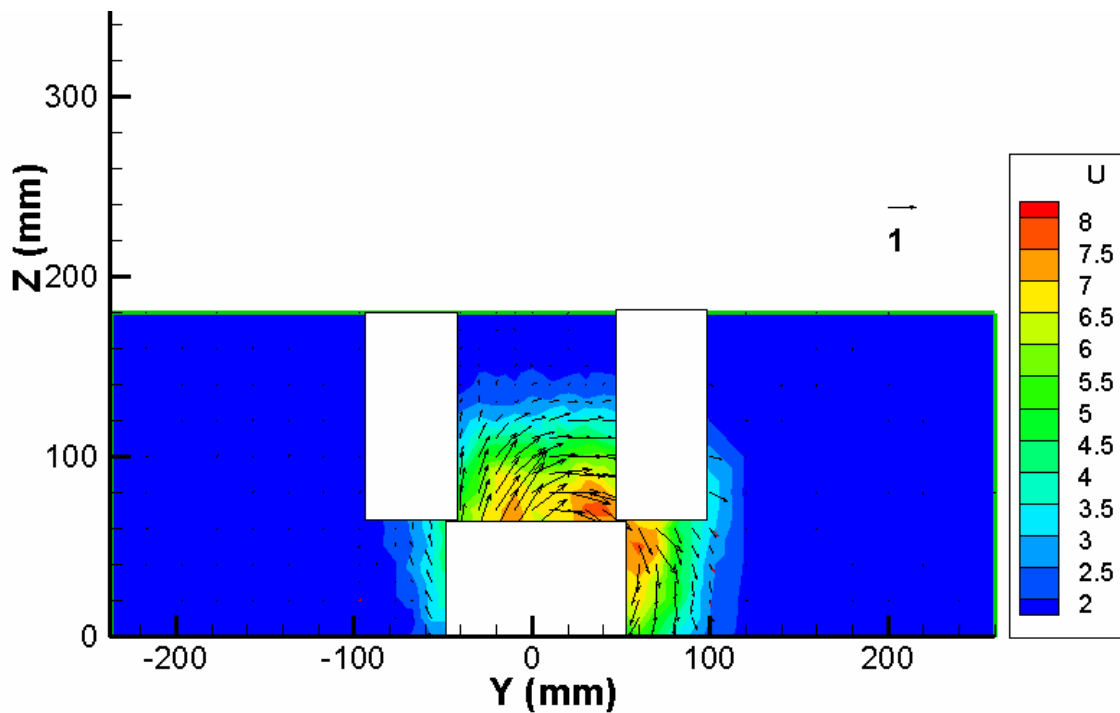
Figure 38. Wing Removed with a Zero Freestream, Powered Propeller Velocity Profile

Figure 39 shows the propeller running with the flexible wing attached to the fuselage. The plot clearly demonstrates how the rotational propeller wake is influenced by the wing. Starting with the top center of the propeller wake, the flow rotates clockwise until it hits the top of the right wing where it begins to move outward toward the wingtip. This creates the downward force on the right wing as indicated by the static test results. Then under the right wing the flow moves toward the center of the MAV. Under the left wing and close to the fuselage the flow then moves up toward the wing where it changes direction and moves out toward the wingtip under the left wing. This causes an upward force on the left wing. Collectively the rotational flow creates a right hand moment on the MAV, which counters the torque applied to the MAV by the motor.

The wing also causes the axial velocity component to spread or flatten out when compared to Figure 38.
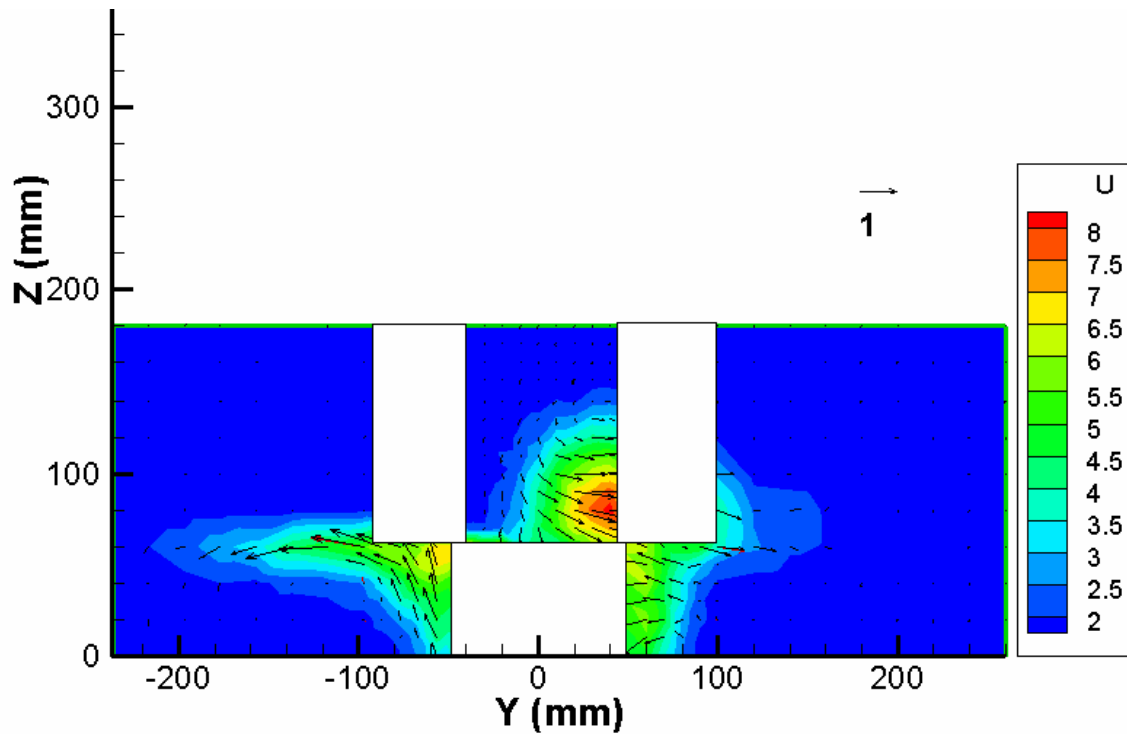
Figure 39. Flexible Wing with a Zero Freestream, Powered Propeller Velocity Profile

The velocity profile of the propeller running with the rigid wing attached is shown in Figure 40. The profile looks similar to that of the flexible wing with some minor differences. Most notably the downwash and upwash on the wings takes on different characteristics. When the downward flow hits the rigid wing at (y=80 *mm*, z=60 *mm*), it moves straight out in the *y*-direction. With the flexible wing the downwash appears to be absorbed slightly or pushes the flexible wing down. The same holds true on the left side of the rigid wing where the vector turning point is very distinct. The rigid wing also

seems to spread out the axial component of the propwash more than the flexible wing. This helps explain why the rigid wing had slightly higher drag values during the static tests than the flexible wing.
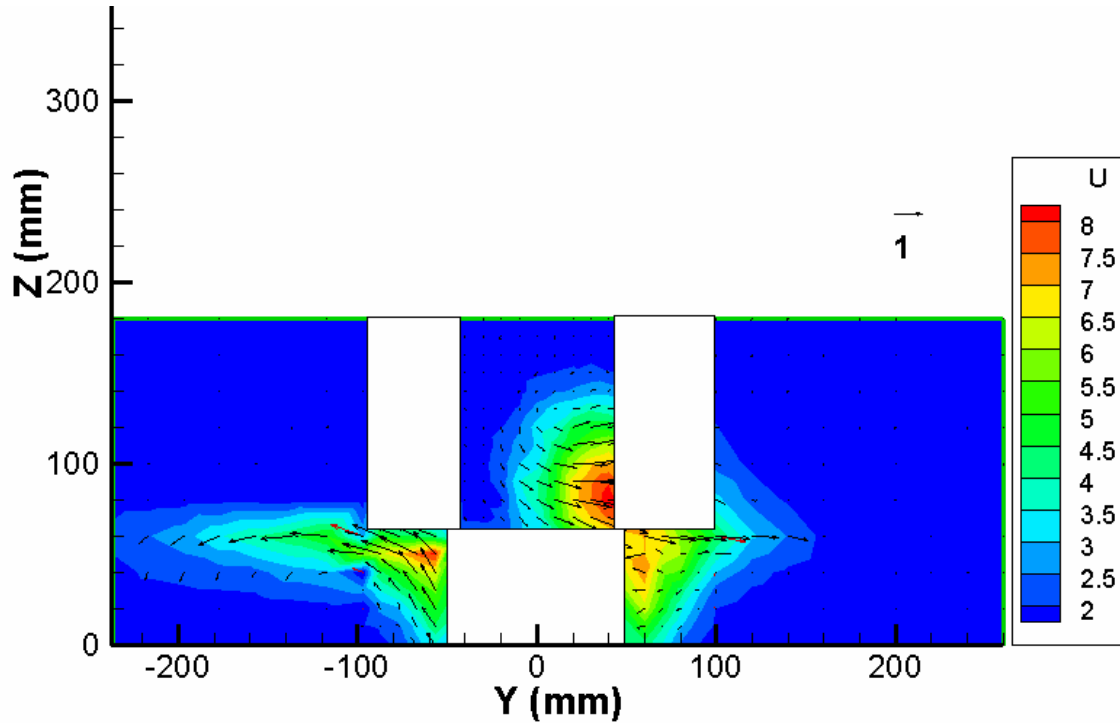
Figure 40. Rigid Wing with a Zero Freestream, Powered Propeller Velocity Profile

The next plot shows the difference between the rigid wing and the flexible wing profiles from the propeller only case. The flexible wing velocities are subtracted from the rigid wing velocities and as a result the values of the velocities are small. It graphically shows some of the propwash differences between the flexible and rigid wing mentioned above. The axial component suggests that the rigid wing provides a stronger deflection of the slipstream, causing it to spread out more, as the areas under the inner part of the wing show a faster velocity. Also, the increased strength in the rotational

70

defection of the rigid wing is seen by the vector lines above the right and below the left side of the wing. The differences are somewhat minor but they help quantify the differences between the rigid and flexible wing with respect to the propeller slipstream.
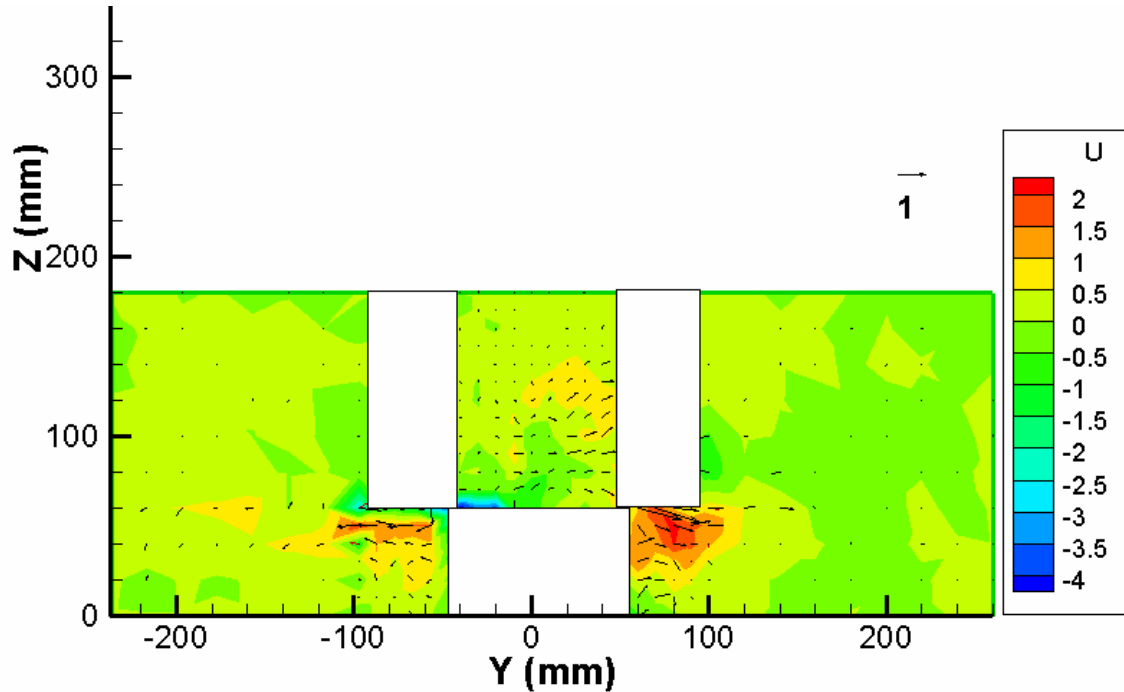
Figure 41. Difference Between Rigid Wing and Flexible Wing/Propeller Only Zero Freestream Velocity Profile (Rigid Minus Flexible)

Nominal 20 MPH Velocity Profiles

Figures 42 and 43 show the velocity profiles with the flexible wing attached. Figure 42 is with the tunnel running at 8.2 *m/s* (nominal 20 *mph* tunnel setting) and the propeller off. Figure 43 is with the same tunnel velocity but with the addition of the propeller running at 8000 RPM. In order to capture the entire flow regime for each plot the color scales are not the same. Figure 44 shows a vertical slice on the outer part of the wing to compare the actual freestream values between the two plots.

Figure 42 includes the wingtip region on the left side of the MAV. The vector lines clearly demonstrate the flow created by the wingtip vortices. The red areas (8.2 *m/s*) indicate the freestream tunnel velocity and all other contours show a velocity deficit over the wing and fuselage. The light green and yellow contours (6.0-7.5 *m/s*) around *z*=75 *mm* indicate the drag directly behind the wing and the blue in the center shows that the largest velocity decrease is at the center of the fuselage aft of the wing. The vector lines near the fuselage show a velocity component heading toward the MAV, which indicates the flow remains attached at this point, where the fuselage is tapered inward. For reference, the wing extends from -305 *mm* to +305 *mm*.
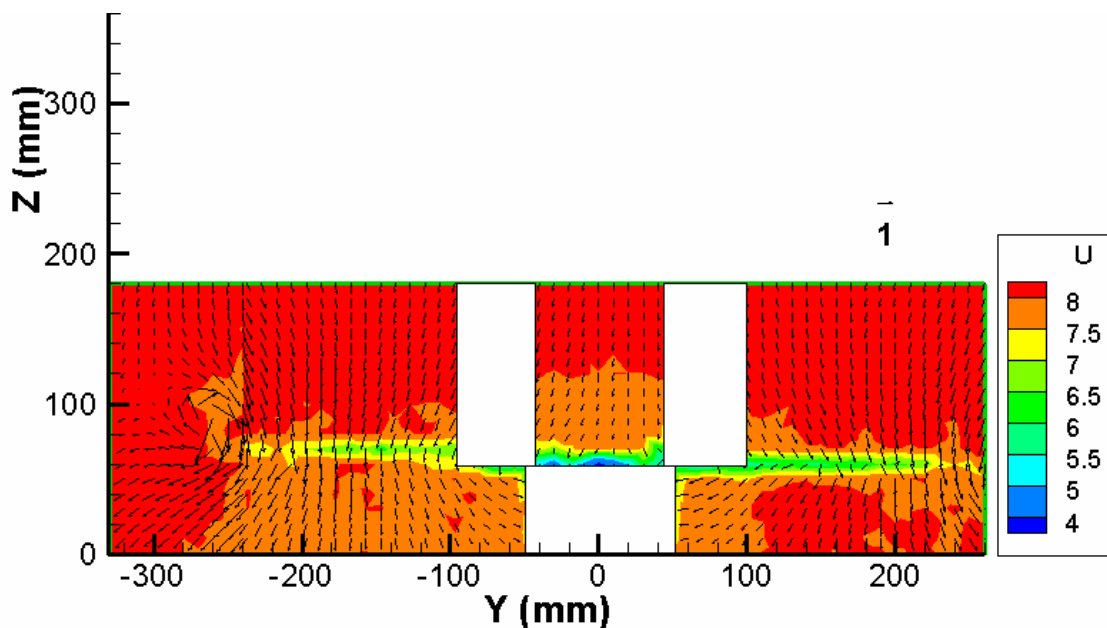
Figure 42. Flexible Wing with an 8.2 m/s (18.3 mph) Freestream Only Velocity Profile

The addition of the propeller running in Figure 43 changes the velocity profile in many ways. The most obvious change is the addition of the propeller wake creating a

large *u*-component near the center of the MAV as indicated by the 10 *m/s* to 11 *m/s* (orange and red) contour levels. Since the effect of the propeller is mixed with the tunnel velocity, it is not as pronounced as in the zero freestream case of Figure 39. The axial component has a maximum increase just over 3 *m/s* with the addition of the propeller in the nominal 20 *mph* case, while it created over 8 *m/s* of flow with no freestream. This shows that the axial velocity components cannot simply be added together to show the combined flow. The circular flow of the propeller wake is still highly recognizable, especially near the center of the MAV, however the propwash effects on the wings are not as prevalent. This shows that the addition of the freestream velocity could affect the magnitude of the reaction forces caused by the propeller on the MAV. This is further investigated in the momentum balance section of Chapter IV.
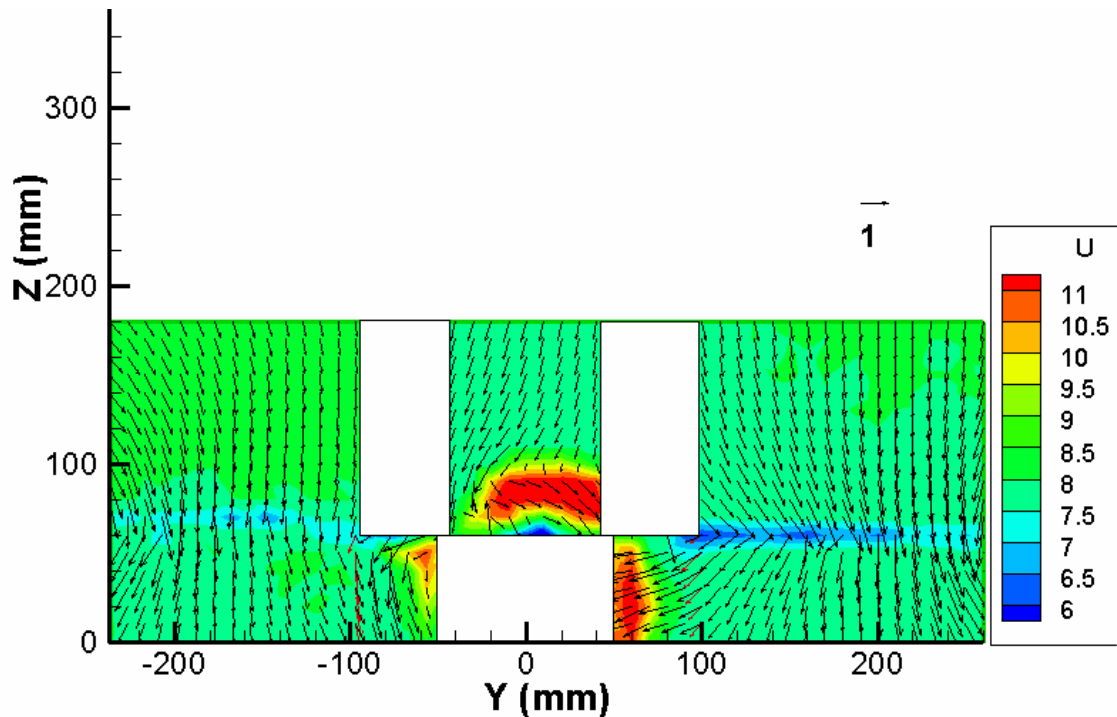
Figure 43. Flexible Wing with an 8.2 m/s Freestream, Powered Propeller Velocity Profile

In Figure 44 the velocity profiles of the previous two plots are compared to show how closely the *u*-components match up. At first glance of the two plots, they may appear quite different due to the color range. Also it is more difficult to identify the drag directly behind the wing in Figure 43 due to its color palette. Taking a vertical slice of the velocity beyond the effects of the propeller wake at *y*=160 *mm* shows that the two profiles differ by less than 2%. It also shows that the drag created by the wing at that point is at exactly the same location for each test.
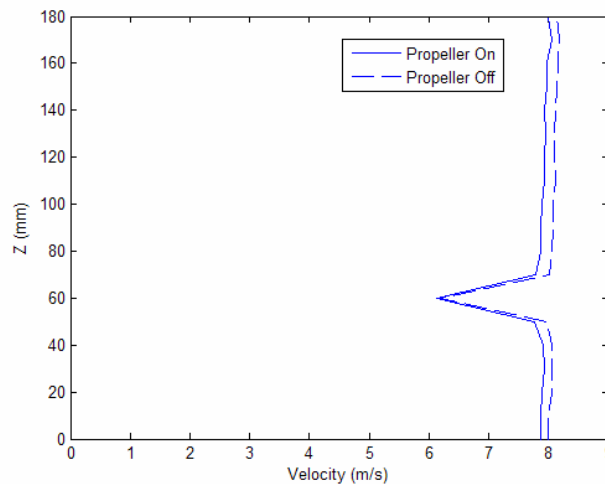
Figure 44. Flexible Wing Velocity Comparison at Outer Part of Right Wing (y=160mm) Between Propeller-On and Propeller-Off Cases (8.2 m/s)

The same tests with and without the propeller running were conducted on the rigid wing for comparison to the flexible wing. The results are shown in Figures 45 and 46. There is a slight difference in the measured freestream values between the flexible wing tests and the rigid wing tests. Again this difference (less than 4%) is due to minor

changes in testing conditions over multiple days. In the freestream-only case, with both the flexible and rigid wings, the velocity under the left wing (7.0 *m/s* to 7.5 *m/s,* yellow area in Figure 45) is less than the velocity under the right wing and over the entire MAV. This is most likely due to wind tunnel variations and not a physical attribute of the MAV or the propeller. The velocity deficit behind the rigid wing is also easy to depict although it varies more in the spanwise direction than it did for the flexible wing. The rigid wing's velocity deficit is high on the inside portion of the wing then decreases toward the wingtips whereas the flexible wing's remains relatively constant over most of the wing.
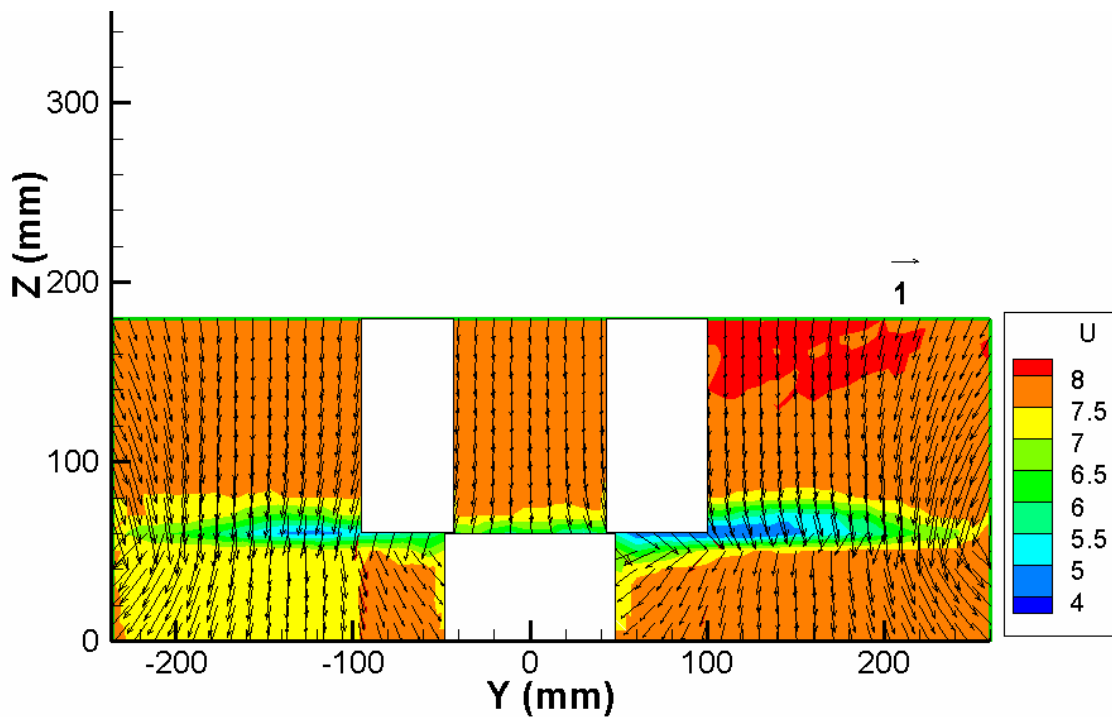
Figure 45. Rigid Wing with an 8.0 m/s (17.9 mph) Freestream Only Velocity Profile

With the propeller running in Figure 46, the rigid wing's velocity profile looks qualitatively similar to the flexible wing's profile. The *u*-component velocity increase

due to the propeller wake near the center of the MAV looks nearly identical for the rigid wing, as does the rotational flow at that point. An important difference is that the velocity deficit behind the wing is much more pronounced with the rigid wing than for the flexible wing. The height of the rigid wing's deficit is more than twice that of the flexible wing's and much more distinguishable on the left side where it is more difficult to see on the flexible wing. Notably, however, part of this apparent difference could also be due to the resolution of the grid during the propeller-on tests. After the first tests were performed on the flexible wing at 10 *mm* intervals the motor failed and had to be replaced. In an effort to extend the life of the motor, the tests on the outer wing grids were done at 20 *mm* intervals. The tests on the inner grids remained at 10 *mm* intervals to capture the bulk of the propwash effects.
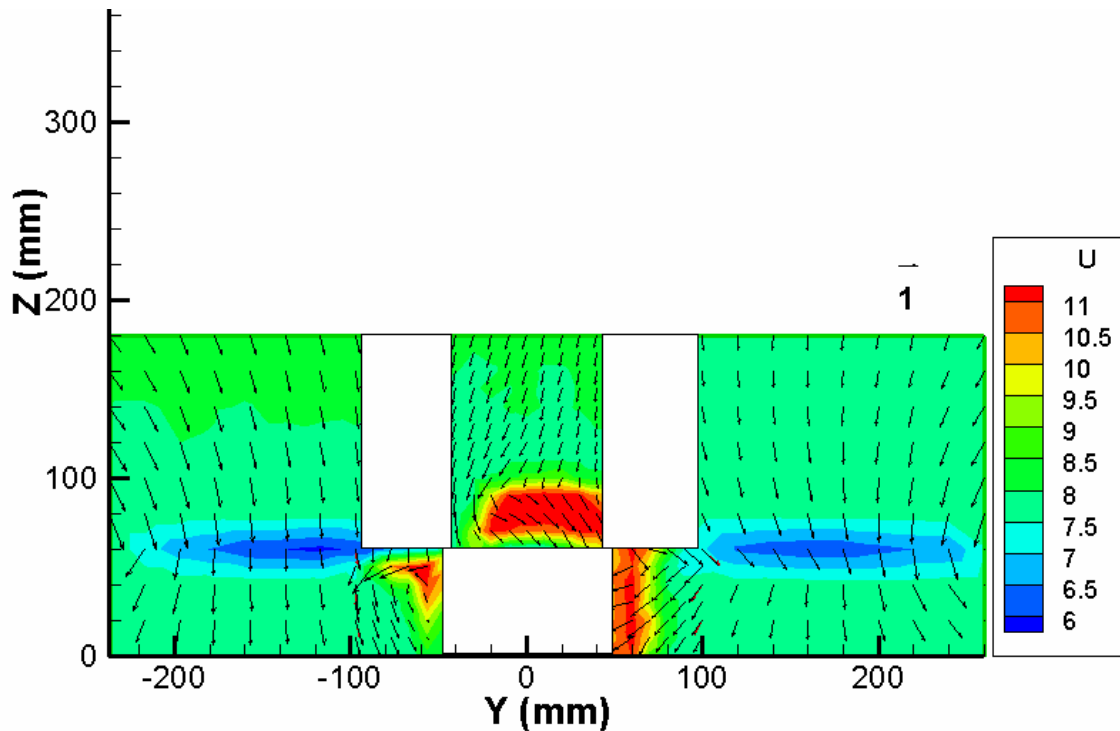
Figure 46. Rigid Wing with an 8.0 m/s Freestream, Powered Propeller Velocity Profile

As with the flexible wing, Figure 47 shows a comparison of the two rigid wing plots at *y=160 mm*. It demonstrates how close the freestream velocity profile is between the propeller running and propeller-off cases. Compared to the flexible wing at this point, the plot shows the velocity deficit notch is nearly 20 *mm* wider. The center of the velocity deficit behind both the flexible and rigid wings is located just above *z=60 mm*.
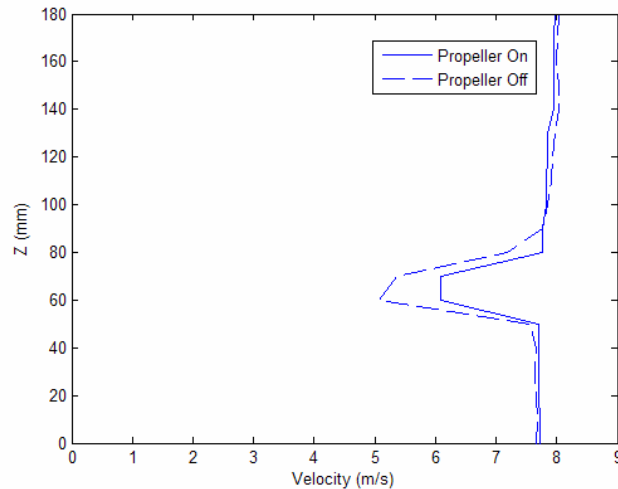
Figure 47. Rigid Wing Velocity Comparison at Outer Part of Right Wing (y=160mm) Between Propeller-On and Propeller-Off Cases (8.0 m/s)

The differences between the rigid and flexible wing at 8 *m/s* can be further examined. Figure 48 shows the difference between the rigid and flexible wing propeller-off velocity profiles on the right side of the wing at 8 *m/s*. The plot captures the difference in the axial velocity deficit created by the rigid wing versus the flexible wing and clearly shows that the deficit is much larger behind the rigid wing. The negative values between *z=50 mm* and *z=90 mm*, show specific areas where the deficit is higher

with the rigid wing. The larger area is most likely due to a laminar separation bubble on the rigid wing as described by Mueller (ref. #31) and Ifju et al. (ref #22), which causes an increase in drag. Notably, balance data acquired during each test shows the drag is 0.037 lb_f with the flexible wing and 0.052 lb_f with the rigid wing. It also shows the lift on the flexible wing is 0.310 lb_f and on the rigid wing is 0.423 lb_f, which leads to slightly higher values of induced drag on the rigid wing. Taking the increase in induced drag into account, the profile drag is still almost 24% higher with the rigid wing. The flexible wing was designed in part to help reduce the chance of laminar separation and the velocity data, in this regard, affirms the findings of DeLuca et al. (ref #11).
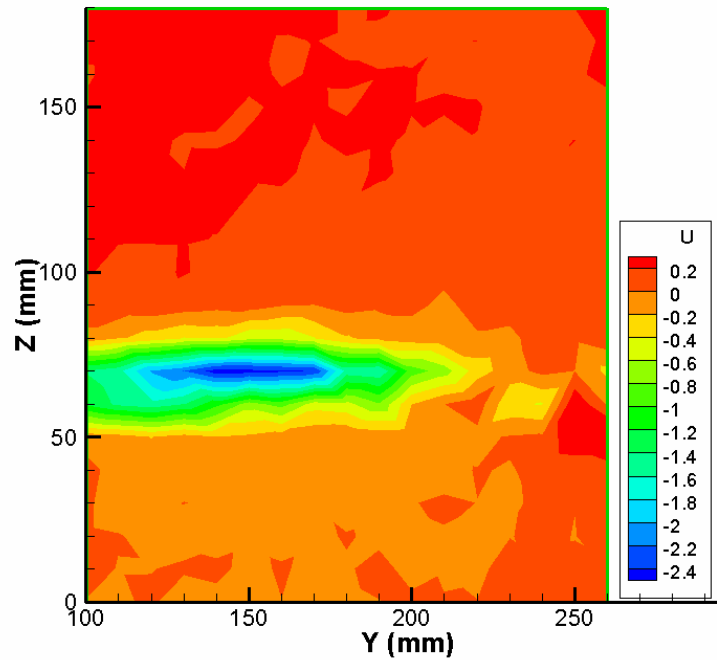
Figure 48. Difference Between Rigid Wing and Flexible Wing with an 8.0 m/s Freestream Velocity Profile of Right Wing (Rigid Minus Flexible)

Figures 49-51 show the rigid/flexible wing differences in the rotational flow components around the fuselage at 8 *m/s* with the propeller running. Figure 49 is a vector representation of the rigid wing minus the flexible wing. Figure 50 shows a contour plot of the *v* or spanwise velocity component and Figure 51 shows the same contour plot for the *w* or vertical component. Slight differences can be seen between the two wings near the fuselage. The rigid wing pushes the velocity outward on the wing more than the flexible wing, just as was seen in the zero freestream case. This is seen both in the vector lines of Figure 49 and in the spanwise velocity plot of Figure 50. The vertical velocity component shows only small differences at a few spurious points, but indicates a slightly stronger downward component above the right side and upward component under the left side with the rigid wing.
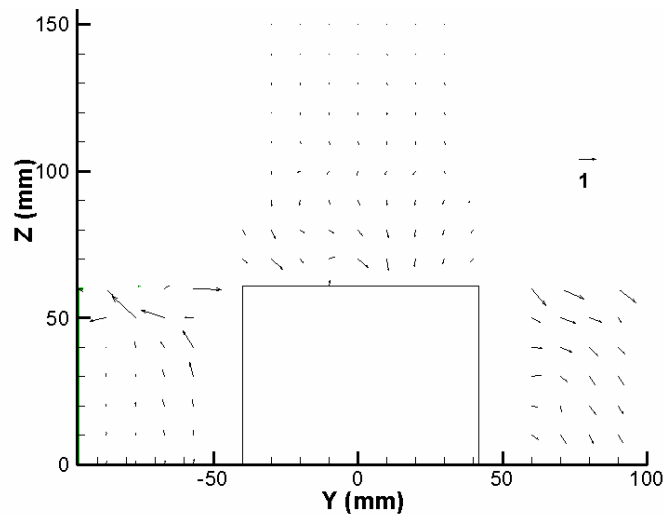
Figure 49. Difference Between Rigid Wing and Flexible Wing Vector Plot with an 8.0 m/s Freestream and Propeller-On (Rigid Minus Flexible)
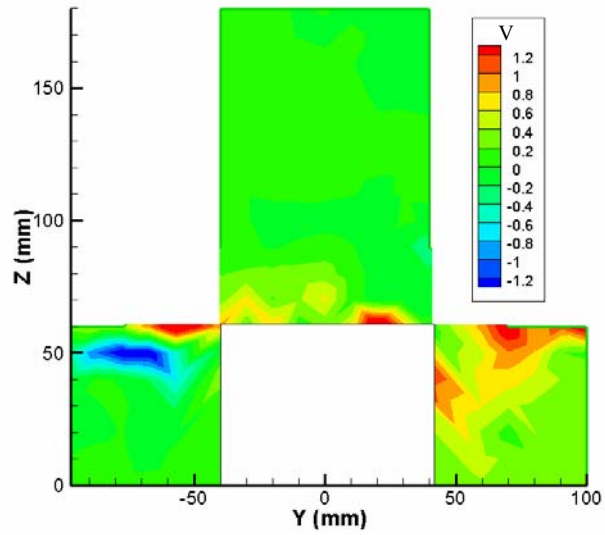
Figure 50. Difference Between Rigid Wing and Flexible Wing Spanwise Velocity Component with an 8.0 m/s Freestream and Propeller-On (Rigid Minus Flexible)
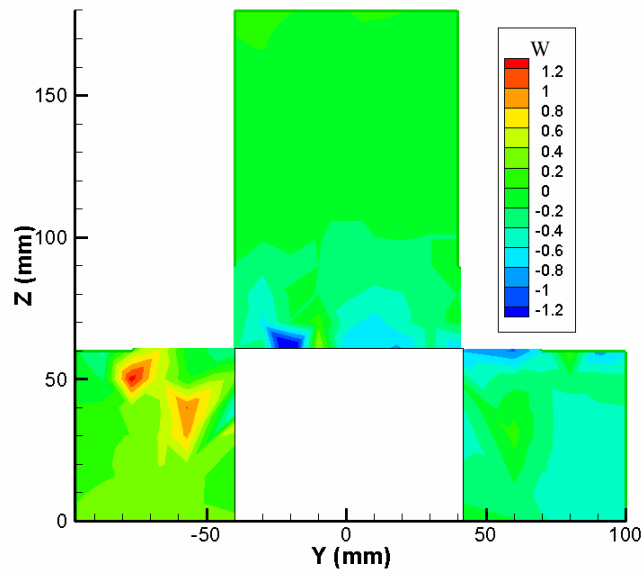
Figure 51. Difference Between Rigid Wing and Flexible Wing Vertical Velocity Component with an 8.0 m/s Freestream and Propeller-On (Rigid Minus Flexible)

Nominal 30 MPH Velocity Profiles

The same tests were performed at a nominal tunnel setting of 30 *mph* to inspect potential differences as speed is increased across the MAV. 20 *mph* and 30 *mph* settings were chosen to examine likely real world flight velocities. Figure 52 shows a full profile (wingtip included) of the flexible wing with a tunnel velocity of 12.25 *m/s* (nominal 30 *mph* tunnel setting). The velocity field looks very similar to the 20 *mph* case in Figure 42. The wingtip vortices and the velocity deficit behind the wing are clearly present. In both plots, the left side of flexible wing appears to be higher than the right. The center of the drag profile on the left wing is nearly 10 *mm* higher. The static wing heights were measured in the tunnel prior to testing and the left side was 1.6 *mm* higher at the root and 8 *mm* higher at the tip than the right side due to mounting imperfections. In the nominal 30 *mph* case, freestream velocity values are reached in all areas surrounding the wing, whereas in Figure 42, especially under the left side of the wing, freestream values were not achieved in the nominal 20 *mph* case. This holds true for most of the flexible and rigid wing plots in the 30 *mph* tests. Since the flow around the wing is fully encompassed by the freestream velocity, making the velocity deficit easy to measure, the momentum balance at 30 *mph* should be more reliable than at 20 *mph*.
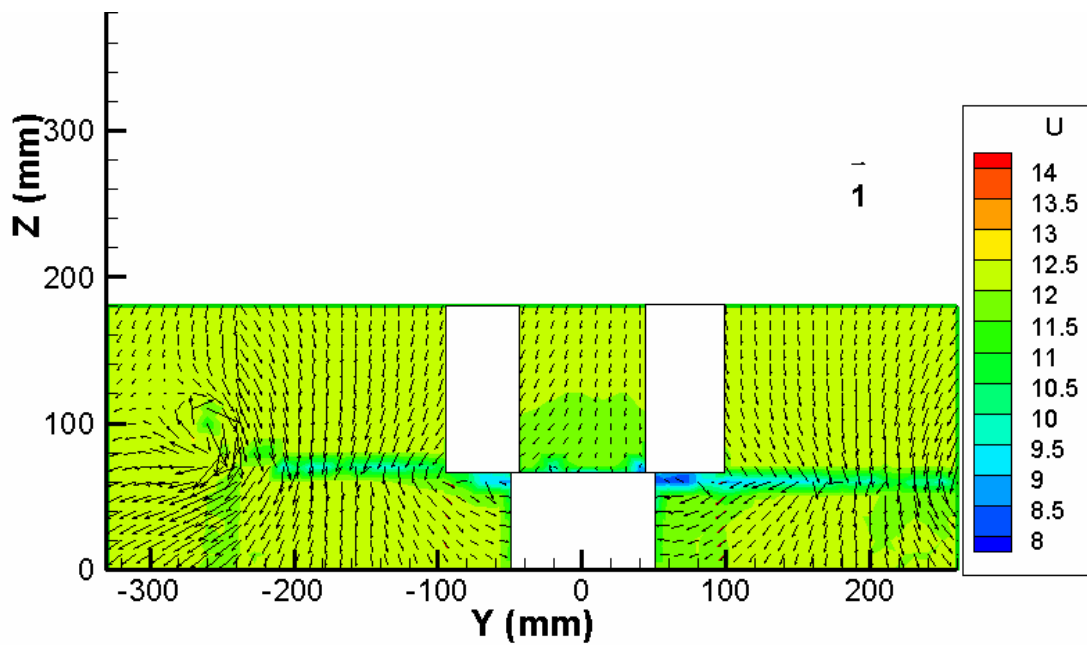
Figure 52. Flexible Wing with a 12.25 m/s (27.4 mph) Freestream Only Velocity Profile

Figure 53 shows the flexible wing with the nominal 30 *mph* (12.25 m/s) freestream and the propeller running. Again the pattern looks similar to the flexible wing in the nominal 20 *mph* test (Figure 43), however the axial propwash component contracts more in the nominal 30 *mph* test. At the top center of the 20 *mph* test, the axial propwash extends to $z=110$ *mm*, where it only goes to $z=98$ *mm* in the 30 *mph* test. This shows that the propwash contracts more as the freestream velocity increases, which is also easy to see when either case is compared to the zero freestream and propeller running plots (Figures 38-40). This could effectively cause a reduced roll moment due to propeller wake at higher inflow velocities.
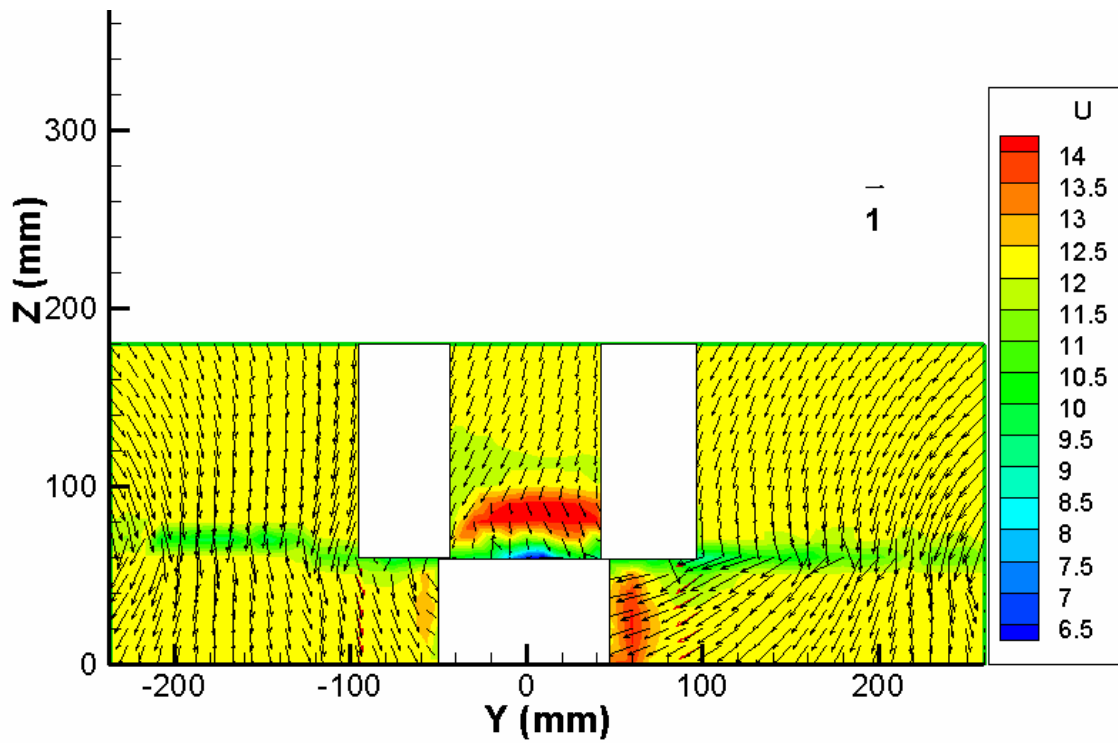
Figure 53. Flexible Wing with a 12.25 m/s Freestream, Powered Propeller Velocity Profile

Figure 54 shows a comparison of the two flexible wing velocity profiles at the nominal 30 *mph*. As in previous cases, the freestream values between the two tests are very close and the velocity deficit falls in the same location for both the propeller-on and propeller-off cases. In all of the tests, the velocity at the bottom of the profile is slightly less than at the top, which shows that the freestream velocity above the wing may actually be slightly higher than below. During the test setup, this was examined by moving the hot-wire probe to its lowest possible point which extended more than 100 *mm* below the as-presented *z*=0 *mm* location. The freestream velocity stayed constant during the scan and never quite reached the velocity value obtained above the wing. Rather it remained 1.2% lower.

83
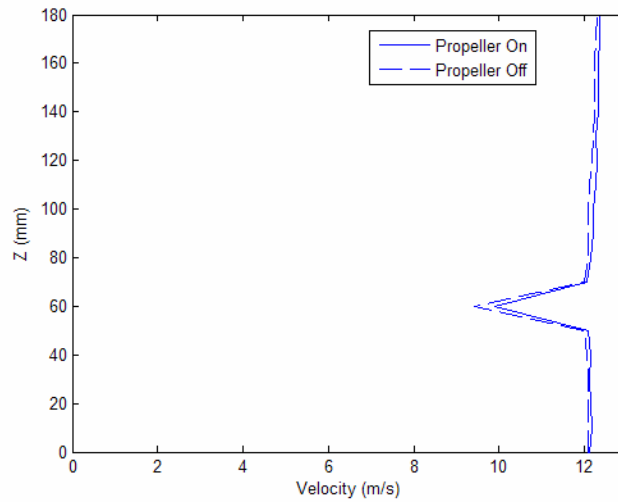
Figure 54. Flexible Wing Velocity Comparison at Outer Part of Right Wing (y=160mm) Between Propeller-On and Propeller-Off Cases (12.25 m/s)

The rigid wing velocity profiles at 12.1 *m/s* (nominal 30 *mph*) are shown in Figures 55 and 56. The wingtip area is included on the left side of the freestream-only plot and clearly shows a wingtip vortex. It also shows an increase in axial velocity just above the inner part of the wingtip at the center of the vortex, which is consistent with the findings of Anderson and Lawton (ref. #1). As in the nominal 20 *mph* case, the rigid wing provides a clear picture of the velocity deficit behind the wing which appears to be the same on both sides of the MAV.
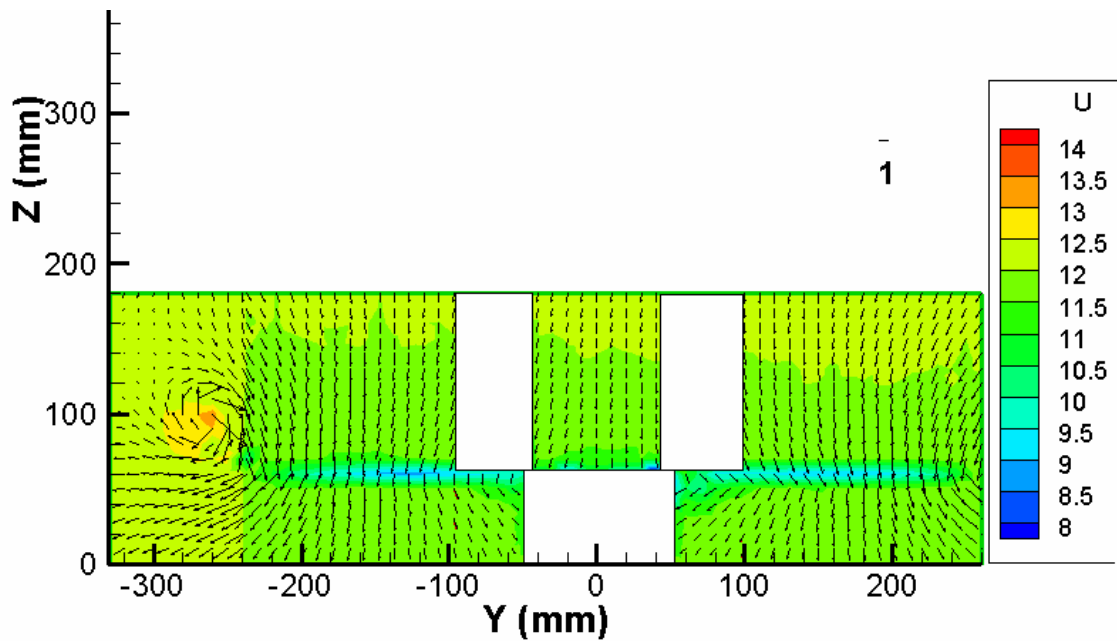
Figure 55. Rigid Wing with a 12.1 m/s (27.1 mph) Freestream Only Velocity Profile

When the propeller is added in Figure 56, the propwash effects look similar to those in the flexible wing profile; however, just as in the nominal 20 *mph* case, the velocity deficit behind the rigid wing appears to be slightly larger than behind the flexible wing. In this case the difference in the deficits between the rigid and flexible wing are much less pronounced. Figure 57 shows this difference over the right wing. Only small variations occur in a few regions however. The overall deficit profile of the rigid wing is quite similar to the flexible wing. This indicates that the effect of the laminar separation bubble that was seen on the rigid wing at 20 *mph* is far less prevalent for this higher freestream velocity. This is consistent with what one would expect with increasing Reynolds number.
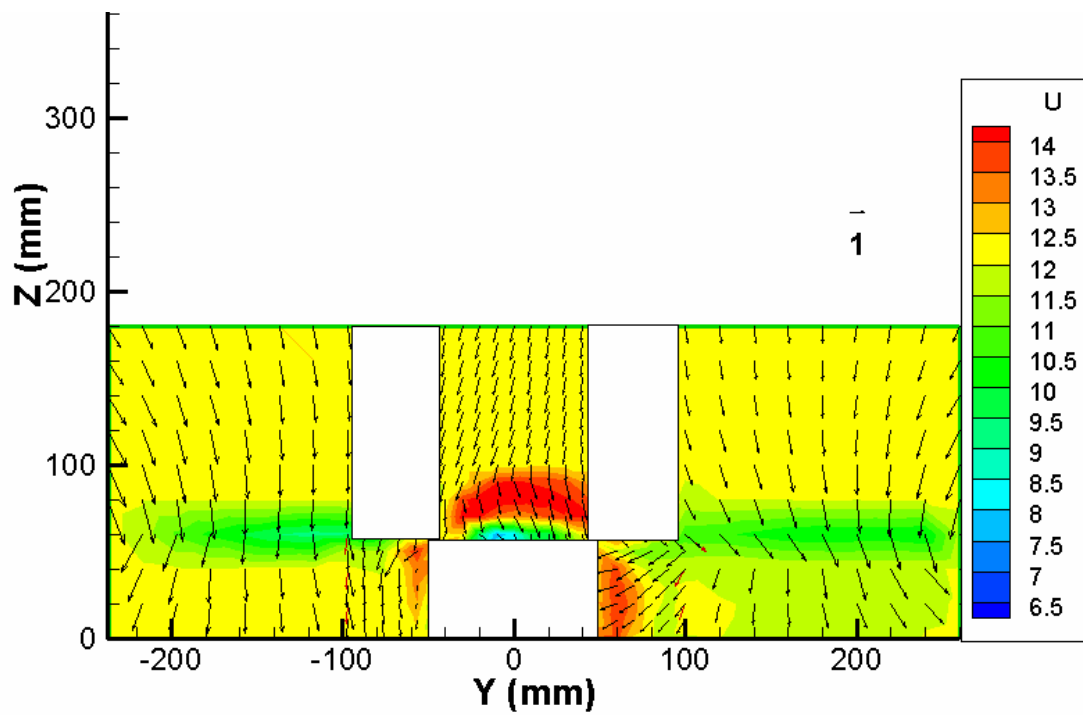
Figure 56. Rigid Wing with a 12.1 m/s Freestream, Powered Propeller Velocity Profile
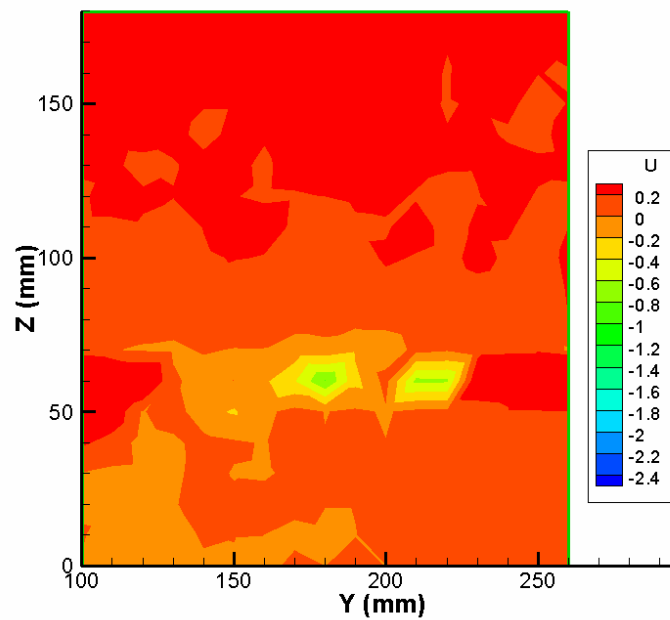
Figure 57. Difference Between Rigid Wing and Flexible Wing with a 12.2 m/s Freestream Velocity Profile of Right Wing (Rigid Minus Flexible)

Figure 58 shows the velocity comparison between the two rigid wing plots only. The freestream error is slightly larger than in the previous test, but is still less than 4%. Comparing the deficit region to the flexible wing case in Figure 54 again shows that they are very similar at this speed. Note that the spacing in this plot for the propeller-on case is 20 *mm*, instead of 10 *mm* as before, due to previously discussed testing procedures. This could be part of the reason for the larger spread in the velocity deficit notch of the propeller-on curve. The velocity data from the profiles shown in this section will now be used in a momentum balance to extract and separate thrust and drag values.
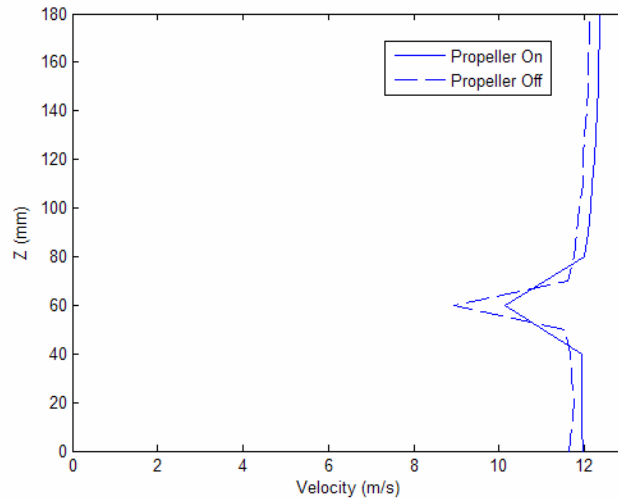
Figure 58. Rigid Wing Velocity Comparison at Outer Part of Right Wing (y=160mm) Between Propeller-On and Propeller-Off Cases (12.1 m/s)

Momentum Balance (Thrust and Drag)

The purpose of this section is to utilize the velocity profiles measured in the wind tunnel and use momentum theory to find propeller thrust, drag due to propwash and total drag. The values will be compared to those found in the static tests where the propeller

thrust and propwash drag could be easily found by separating the propeller and motor from the MAV. In addition, they will be compared to combined forces measured with the wind tunnel balance for the as-configured MAV. There is currently no setup in the AFIT wind tunnel that can easily separate the motor from the MAV and take reasonable data. Many ideas were brainstormed to get this type of data including mounting a separate motor with a shroud around it and measuring thrust and torque from a sting extending from the top of the tunnel. This could be attempted in the future, but the blockage caused by the motor and shroud would severely disrupt the flow around the aircraft. Even in the Purdue University setup (described in ref. #38 and shown in Figure 13 of this document), there was a considerable amount of blockage and losses which made the experimental results less reliable. Without the ability to easily separate the motor from the MAV, the balance is only able to collect net forces and moments. The axial force component includes the total drag minus the propeller thrust. The total drag in this case is considered to be the drag caused by the freestream velocity plus the drag caused by the propeller wake. In the static tests, propwash drag to thrust ratios were found at different propeller speeds. The same non-dimensional ratios are found for the wind tunnel tests using a momentum balance.

The process of taking the velocity data from multiple test runs and extracting drag values requires some assumptions. One assumption is that the blank areas in the velocity data, indicated by the white rectangles in the contour plots, need to be accounted for to include the total velocity deficit. Another assumption is that the velocity measured at the outer edges of the contour plot is considered equal to the freestream velocity forward of

the wing. This is important since measurements were not taken in front of the wing due to the tunnel setup. In a momentum balance, from equation **(8)**, V_1 is the velocity profile in front of a body while V_2 is the velocity profile aft of a body. A further assumption is that the difference in the two velocity profiles when both the freestream and propeller wake are included will yield the total drag on the MAV.

To begin the process, the balance data for each test was time averaged and corrected for sensor interactions. This was done using portions of the Matlab® code developed by Capt DeLuca and Lt Gebbie and modified by Lt Rivera Parga (ref #10, #19, and #34). Since only the actual force numbers are needed for the momentum balance, the part of the program that develops force and moment coefficients was not utilized. The corrections to the balance data changed the axial component by less than 3% in most cases. In the rigid wing case at the nominal 30 *mph*, the corrected axial component is 1.509 *oz* and the raw axial component is 1.467 *oz,* which is a 2.8% change. Other raw and corrected balance data are presented in Appendix B for comparison.

Once the axial force component from the balance was available, a program was developed to perform the surface integrals of the velocity profiles. The Matlab® program was able to take two velocity profiles, difference them, and integrate over the entire surface to find drag forces. It performs the surface integrals one grid at a time. Grids 1-5 from Figure 30 are all added, plus the wingtip grid is added twice to account for both tips. The wingtip data was only collected on one side but assumed to be symmetric. The wingtip data is also included in both powered and non-powered runs equally since the propeller doesn't affect the velocity differential that far out on the wing. A more difficult

89

process was deciding how to interpolate across the blank areas (those areas unable to be tested). Since the top two blank areas take on similar geometry to their surrounding grids, (encompassing the wing just outside the fuselage) it is reasonable to perform a linear interpolation between the outer grids and the top center grid. The single blank area centrally located under the wing is more difficult to interpret. It includes the fuselage and the sting as well as some open area under the wing. This data is accounted for in a few different ways to examine its validity and relevance.

To develop an initial understanding and validation of the momentum balance, the nominal 30 *mph* flexible wing case without the propeller running is used. In this case the difference in the velocity field one inch aft of the wing from the freestream velocity should primarily yield the drag acting on the MAV. Since this test was with the tunnel running only, the balance data measured only drag in the axial direction. The drag measured by the balance includes the drag on the wing, the fuselage and the tail. Comparing this balance data to a similar test where the wing was removed, the drag contribution of the fuselage and tail was about 25% of the overall drag. Although the velocity measurements in this test were measured in front of the tail, at zero degrees angle of attack it is assumed that the fuselage contributes most of the 25% and therefore the momentum balance calculations are compared to the total drag on the MAV. The drag on the tail is assumed to be small and is left unaccounted for in the momentum balance. This provides a baseline examination of the momentum balance used for the other test runs. The blank, untested, area under the wing is accounted for by linear interpolation between grids 2 and 4 from Figure 30 in one case and left unaccounted for

90

in another for comparison. In the latter case, this approach is tantamount to assuming

that the momentum deficit in this region is negligible. Since balance data provides a

direct comparison in this case, the results clearly indicate the necessity to interpolate

across the bottom section. The results for this initial momentum balance are shown in

Table 7. In this case it appears that including the interpolation of the lower blank section

is an improvement. The error between the balance data and the momentum balance is

extremely low and is not expected to be representative of error levels in powered runs.

The same drag-only analysis is done for each of the other test conditions with varying

results. The primary outcome of this first comparison is that each of the blank, untested,

areas will be interpolated for the rest of the tests.

Table 7. Flexible Wing (Nominal 30 MPH) Momentum Balance Results

	Balance Result	Momentum Result Interpolating Across Lower Blank Area	Momentum Result Without Interpolating Across Lower Blank Area
Drag Force	1.263 oz	1.256 oz	1.119 oz
% Error		0.5%	12.8%

In order to extract the drag caused by the propeller wake, a few simple

relationships must be assumed. The first is that the axial component, *A1*, of the balance

is the difference between the thrust and the total drag. The total drag (D_T) is a

combination of the freestream drag (D_∞) and the drag due to propwash (D_{PW}). The

equations relating these values are:

$$A1 = D_T - T \qquad \qquad \textbf{(13)}$$

$$D_T = D_\infty + D_{PW} \qquad \qquad \textbf{(14)}$$

Where:
$A1$ = corrected balance axial force (oz)
T = thrust (oz)
D_T = total drag (oz)
D_∞ = drag due to freestream velocity (oz)
D_{PW} = drag due to propwash (oz)

The next momentum balance is performed on the flexible wing at 30 *mph* with the propeller running at a nominal 8000 RPM. This test is slightly different than the previous in that the velocity value in front of the wing is not the freestream only. The incoming velocity profile also includes the propeller slipstream velocity. For this reason, separate tests were conducted with the wing removed so a baseline velocity profile could be developed to represent V_1 in equation **(8)**, which includes both the freestream velocity along with the propeller wake. All of the other assumptions mentioned above are still utilized in this process, but the velocity deficit due to the wing is now subtracted from actual measured data. In order to have a direct comparison between the flexible wing case and wing removed case, the freestream velocity values have to match perfectly. Since this is nearly impossible in tunnel testing, a ratio of freestream velocities is found and multiplied through the velocity profile prior to differentiating. For this momentum balance the freestream velocity is 12.45 *m/s* with the flexible wing attached and 12.03 *m/s* without. Therefore, a 1.035 multiplier is applied to the V_1 value prior to the integration. Once this is taken into account, the integration is performed and the drag values are found. The results are shown in Table 8. With these values, the propeller drag to thrust ratio is 0.138 for the flexible wing at 30 *mph*. The total process used to find the thrust and propwash drag is listed below.

1. Find drag due to freestream only (D_∞) using axial balance data from tests *without* propeller running (measured) and compare to momentum balance results (calculated from velocity measurements).

2. Find total drag and thrust ($D_T - T$) using axial balance data tests *with* propeller running (measured results).

3. Perform momentum balance between wing on and wing off using velocity data *with* propeller running to find total drag (D_T) (calculated from velocity profiles via surface integration).

4. Find thrust (T) by subtracting balance results ($D_T - T$) from momentum results (D_T).

5. Find propwash drag (D_{PW}) by subtracting freestream only drag (D_∞) from total drag (D_T). $D_{PW} = D_T - D_\infty$

Table 8. Flexible Wing (Nominal 30 MPH with Propeller Running) Momentum Balance Results

	Balance Results (measured)	Momentum Results (calculated from velocity mesurements)	Thrust (calculated by D_T-(D_T-T))	Freestream Only Balance Result from Table 6 (measured)	Propwash Drag (calculated by $D_{PW}=D_T$- D_∞)
	$(D_T - T)$	(D_T)	(T)	(D_∞)	(D_{PW})
Force	-0.013 oz	1.467 oz	1.48 oz	1.263 oz	0.204 oz

The rest of the tests yielded similar results with their momentum balance performed using the same methodology as above. The results of all of the tests are presented together in Tables 9 and 10. Table 9 shows the freestream only cases for the flexible and rigid wings at nominal 20 and 30 *mph* and how they compare with their respective balance force measurements. For nearly all of the tests, adding the full interpolation across the lower section leads to better results. In order to get more exact momentum balance values, the velocities in the blank areas would need to be collected.

93

Notably, this could be challenging due to the interference of the sting. The actual value would most likely be found somewhere in between using the full interpolation and not including it at all. For the values in Table 10, the full interpolation of the bottom blank region was utilized.

Table 9. Flexible/Rigid Wing (Freestream Only) Momentum Balance Results

	Balance Results (D_∞)	Momentum Results (Full Interpolation) (D_∞) (%error)	Momentum Results (Without Lower Blank)
Flex Wing (20 mph)	0.585 oz	0.614 oz (4.9%)	0.518 oz (12.9%)
Flex Wing (30 mph)	1.263 oz	1.256 oz (0.5%)	1.119 oz (12.8%)
Rigid Wing (20 mph)	0.829 oz	0.868 oz (4.7%)	0.770 oz (7.1%)
Rigid Wing (30 mph)	1.509 oz	1.601 oz (6.1%)	1.461 oz (3.3%)

Table 10. Flexible/Rigid Wing (Freestream and Propeller Running) Momentum Balance Results

	Balance Results (measured) ($D_T - T$)	Momentum Results (calculated from velocity mesurements) (D_T)	Thrust (calculated by $D_T-(D_T-T)$) (T)	Table 9 Balance Results (measured) (D_∞)	Propwash Drag (calculated $D_{PW}=D_T- D_\infty$) (D_{PW})
Flex Wing (20mph)	-1.483 oz	0.934 oz	2.417 oz	0.585 oz	0.349 oz
Flex Wing (30mph)	-0.013 oz	1.467 oz	1.48 oz	1.263 oz	0.204 oz
Rigid Wing (20mph)	-1.40 oz	1.183 oz	2.583 oz	0.829 oz	0.354 oz
Rigid Wing (30mph)	0.152 oz	1.759 oz	1.607 oz	1.509 oz	0.250 oz

Now that thrust and drag values have been found for the nominal 20 *mph* and 30 *mph* cases, they can be compared to the results from the static tests. Table 11 shows the

non-dimensional values of drag/thrust for all of the test cases. From the propeller/wing

interaction results, the drag/thrust values for the wing positioned at its design location and

a propeller speed of 8000 RPM are used for comparison. The first thing to notice is that

the overall values of drag/thrust found in the momentum balance are reasonably

comparable to those found in the static tests when the thrust and drag were measured

separately. The drag/thrust ratio appears to be slightly higher when the MAV is placed in

the freestream velocity, which could be due to the mixing of the propeller wake, however

there is a higher uncertainty in the momentum balance measurements. The actual drag

and thrust values also make sense. As the freestream velocity increases and the propeller

remains at the same speed, the thrust decreases and therefore the drag caused by the

propwash also decreases. The consistency of this trend along with the similar values of

drag to thrust ratio show that the momentum balance is a valid approach to finding drag

on a body.

Table 11. Drag/Thrust (Static vs. Wind Tunnel) Comparison

	Propeller Drag (D_{PW})	Propeller Thrust (T)	Drag/Thrust (D_{PW}/T)
Flex Wing (0 mph) From Static Test Setup	0.434 oz	3.686 oz	0.118
Flex Wing (20 mph)	0.349 oz	2.417 oz	0.144
Flex Wing (30 mph)	0.204 oz	1.480 oz	0.138
Rigid Wing (0 mph) From Static Test Setup	0.435 oz	3.666 oz	0.119
Rigid Wing (20 mph)	0.354 oz	2.583 oz	0.137
Rigid Wing (30 mph)	0.250 oz	1.607 oz	0.156

Limitations of Experimental Effort

With any form of experimental research there are inherent sources of error that lead to uncertainty in the results. These experiments are no exception and certain sources of error must be recognized. For the propeller/wing interaction study the primary sources of error lie within the resolution of the AFIT-1 balance, the Lebow torque cell and the Interface load cell. Variation in propeller speed is another source of potential uncertainty however each measurement was normalized to the average RPM setting which should help minimize this error. For the wind tunnel tests the main sources of error are the AFIT-1 balance measurements, tri-wire velocity measurements, propeller speed variations and tunnel speed inconsistency between test runs. The main source of error for the momentum balance is lack of velocity data across the blank regions creating the need for interpolation. These errors can only be estimated at this time until further testing is conducted. Other sources of error exist for both of the tests that arise during data acquisition such as lead wire losses, analog to digital converter errors, time averaging and data reduction errors. These errors are considered subsidiary to the main sources of error and have much smaller effects on the uncertainty of the results. A more detailed analysis of the experimental error is presented in Appendix E.

Summary

All of the tests conducted in this research can be used to justify potential design changes for the MAV. From the propeller/wing interaction study, results indicate that moving the wing more forward on the fuselage will not adversely affect the performance of the motor or the aerodynamics on the MAV, particularly if it is not placed within two

inches of the propeller. Results also show a tradeoff between a high drag to thrust ratio and low roll moment to motor reaction torque ratio based on the height of the wing with respect to the propeller. Velocity profile results from the wind tunnel tests provide insight into the propwash effects on both the flexible and rigid wings. They show how the wing effectively flattens out the rotational flow caused by the propeller and how the propeller increases the axial velocity near the center of the MAV. Differences between the flexible and rigid wings are evident in the velocity profiles. Primarily, hot-wire data acquired one inch downstream of the wing indicated a low velocity region which could be due to laminar separation on the rigid wing. This was found to be more prevalent at lower velocities. Only small differences in propwash effects occur between the two wings but can lead to a slight increase in drag for the rigid wing as seen in the static test results. The velocity profiles also provided a basis for a momentum balance which successfully extracted values in the wind tunnel for thrust and drag from the propeller wake. Wind tunnel results for drag to thrust ratios compared closely to those found during the static, zero freestream tests, which indicates that the propeller/wing interaction conclusions likely apply in forward flight as well.

Chapter IV presented the results of both the propeller/wing interaction tests done out of the wind tunnel and the hot-wire tests performed in the wind tunnel. The results of the static tests showed the propeller and wing performance tradeoffs when the wing was placed in multiple locations. Results of the wind tunnel tests further examined the propeller/wing interactions with the addition of a freestream velocity. Velocity profiles graphically represented the flowfield aft of the wing with the influence of the freestream

velocity as well as the propeller wake. They clearly illustrated the secondary, cross-stream flow patterns around the MAV created by the propeller slipstream and showed the differences in the flow patterns between the rigid and flexible wings.

V. Conclusions and Recommendations

Overview

        The main conclusions developed during the research of the propeller/wing interaction study on the MAV are presented in this chapter. The results of the tests show that the research effort was very successful in accomplishing the goals set forth in Chapter I. Future recommendations for follow-on research, test improvements, and MAV design are included in an effort to expand upon the research conducted herein.

Conclusions and Significance of Research

        This research closely examined the effects a propeller driven propulsion system has on a micro-air-vehicle equipped with either a rigid or flexible wing. By developing a test setup that was able to separate the propulsion system from the body of the vehicle, propeller performance and aerodynamic performance were defined exclusively. This provided the opportunity to investigate the effects of altering the configuration of the MAV. By placing the wing in various locations both axially and vertically, lift, drag and roll moment caused by the wake of the propeller could be defined. At each instance, the thrust and torque created by the propeller were measured separately using a specially designed static test stand. This created the unique opportunity to directly compare the non-dimensional values of drag to thrust ratio, roll moment to torque ratio, and lift to drag ratio for all of the wing positions that were tested. Results from this test led to the following conclusions:

- Drag due to the wake of the propeller is consistently between 11% and 17% of the thrust produced by the propeller for both the flexible and rigid wings.

- Drag to thrust ratio increases as the wing moves closer to the propeller axially, and as the wing moves closer to the axis of the motor shaft vertically. Maximum of 16.7% at X_o=1" and Z_o=0".

- Roll moment due to the wake of the propeller varies from about 25% to 48% of the torque produced by the propeller, with the value increasing as the wing moves vertically closer to the center of the motor shaft (~40% at design location).

- The addition of the wing into the propeller wake at its design location increases the propeller thrust coefficient by about 7% and torque coefficient by 2%.

- Differences in the effect of the wing on the propeller torque and thrust coefficients, between the flexible and rigid wings, are small at zero freestream velocity.

- Drag due to the wake of the propeller for the rigid wing is between 2% and 7% higher than the flexible wing; the difference increasing with increased propeller speed.

- The differences in the non-dimensional values of drag/thrust, roll moment/torque and lift/drag between the rigid and flexible wings are fairly small at zero freestream velocity.

The second effort of this research was to examine the propeller/wing interactions with the addition of a freestream velocity. This was accomplished by placing the original MAV on a balance in the wind tunnel and measuring velocity profiles with a tri-wire anemometer. Velocity profiles were then plotted to show both the axial component as well as the rotational flow created by the propeller. Drag was found by means of momentum theory, taking the difference in two velocity profiles and integrating over the surface of the profile. The balance data along with the velocity profiles provided enough

100

information to effectively determine the thrust and the drag due to the propeller wake.

Results from this test led to the following conclusions:

- Velocity profiles show how the axial component increases in the wake of the propeller at different nominal freestream values (0, 20 and 30 *mph*). The flowfields are shown with the rigid wing, the flexible wing and with the wings removed. They illustrate how each configuration interacts with the propeller slipstream.

- Velocity profiles clearly demonstrate how the wake of the propeller is disrupted by the wing, creating the roll moment that counters the torque applied by the propeller motor. The cross-stream flow creates a downwash on the right wing, then is effectively flattened out by the wing and moves outward toward the wingtip. It also creates an upwash on the left wing and spreads out in a similar fashion.

- Velocity profiles show differences between the rigid and flexible wings. The data indicates that the inner portion (out to about y=210 *mm*) of the rigid wing experiences a laminar separation at a nominal 20 *mph* that creates a much larger velocity deficit and increases drag. At a nominal 30 *mph*, this separation bubble is much smaller and the difference in the drag values between the two wings decreases.

- Propeller slipstream effects are similar between the rigid and flexible wings since most of the propwash acts close to the fuselage when there is a freestream velocity present. Cross-stream patterns indicate a slightly larger outward component with the rigid wing compared to the flexible wing.

- Momentum theory is able to successfully extract drag values of an aircraft in a wind tunnel environment, where balance data provides only net (drag-thrust) values.

- At nominal freestream values of 20 and 30 *mph*, drag due to propeller wake is between 13% and 16% of propeller thrust, which compares closely to values of 12% found during the zero freestream tests in the static setup. This indicates that the static propeller/wing interaction results also likely apply in forward flight as well.

The research conducted during this thesis provided many interesting and significant results. The differences in propeller/wing interactions between a rigid and flexible wing MAV were successfully defined for the zero freestream case as well as the nominal 20 *mph* and 30 *mph* freestream cases. These results could be used in the future to affect other MAV designs. The secondary or cross-stream flow patterns could be utilized to examine the potential advantages to altering the wing design. For example, changing certain wing incidence angles to increase the (counteracting) roll moment due to the propeller slipstream could effectively reduce the overall roll moment on the aircraft. Also, the drag to thrust and roll moment to torque ratio plots (due to propwash) provide information that show how changing wing placement affects both the propeller motor and the MAV aerodynamics. The static experimental test stand provides an easy platform for future testing of this type, where motor characteristics and aerodynamic characteristics are defined exclusively. Finally, it was demonstrated that a complete set of velocity profile data can be utilized by means of momentum balance to calculate drag forces on a body in a wind tunnel.

Future Recommendations

Although this research was successful in determining the basic characteristics of propeller/wing interactions, there is room for improvement and further research. Some of the test setup and equipment could be altered to improve the reliability of the data. Further analysis of torque and roll moment should be investigated in the wind tunnel as well. Recommendations for the future of this research are:

- Run tests with other propellers on the static test stand. The setup is in place to investigate propeller/wing interactions with more efficient propellers.

- Mount tri-wire anemometer on a shorter probe which will allow testing in some of the areas that were unable to be measured during this research due to tail and sting interference. This will provide a much more reliable velocity profile and reduce the uncertainty in the momentum balance process.

- Purchase new motor, speed controller, and remote for MAV. Along with this, create a cooling mechanism for the motor such as fins or slots so air is allowed to cool the motor during long test runs. This will reduce the possibility of burning another motor or speed controller. The new remote will reduce the amount of radio frequency interference.

- Collect more velocity data with MAV at various angles of attack and sideslip angles to capture the propeller wake interactions in more flight configurations.

- Either with an entirely new test setup or by furthering the momentum theory to include the rotational flow, develop a method to capture the roll moment and torque separately in the wind tunnel. To date this has not successfully been accomplished with the MAV.

Appendix A: Additional Data and Rigid Wing Results

Propeller/Wing Interaction Data

The data shown in the tables below follow that presented in Table 5, which included the propeller/wing interaction results for the flexible wing at 10,000 RPM. The following tables include the flexible wing data at the other RPM settings as well as the rigid wing data at all RPM settings. All data tables include representative position data that moves the wing axially in one plane and vertically in another.

Table 12. Propeller/MAV Forces and Moments at 8,000 RPM (Flexible Wing)

Axial Separation X_o (in)	Vertical Separation Z_o(in)	Lift (lb$_f$)	Drag (lb$_f$)	Roll Moment (in-lb$_f$)	Thrust (lb$_f$)	Torque (in- lb$_f$)
4.375	1.25	0.002	0.027	0.043	0.230	0.121
3.75	1.25	0.001	0.026	0.047	0.231	0.122
3.00	1.25	0.002	0.026	0.041	0.227	0.122
2.00	1.25	-0.003	0.027	0.046	0.229	0.123
1.00	1.25	0.002	0.034	0.050	0.232	0.123
4.375	1.25	0.002	0.027	0.043	0.230	0.121
4.375	0.75	-0.001	0.027	0.057	0.208	0.124
4.375	0	0.008	0.031	0.052	0.222	0.124
4.375	-0.75	0.013	0.024	0.037	0.213	0.122

Table 13. Propeller/MAV Forces and Moments at 12,000 RPM (Flexible Wing)

Axial Separation X_o (in)	Vertical Separation Z_o(in)	Lift (lb$_f$)	Drag (lb$_f$)	Roll Moment (in-lb$_f$)	Thrust (lb$_f$)	Torque (in- lb$_f$)
4.375	1.25	0.001	0.055	0.128	0.514	0.270
3.75	1.25	-0.002	0.056	0.108	0.518	0.275
3.00	1.25	-0.007	0.057	0.095	0.518	0.277
2.00	1.25	-0.004	0.059	0.098	0.518	0.278
1.00	1.25	-0.001	0.073	0.105	0.519	0.277
4.375	1.25	0.001	0.055	0.128	0.514	0.270
4.375	0.75	0.002	0.061	0.129	0.485	0.277
4.375	0	0.018	0.068	0.121	0.503	0.279
4.375	-0.75	0.029	0.056	0.076	0.489	0.277

Table 14. Propeller/MAV Forces and Moments at 14,000 RPM (Flexible Wing)

Axial Separation X_o (in)	Vertical Separation Z_o(in)	Lift (lb$_f$)	Drag (lb$_f$)	Roll Moment (in-lb$_f$)	Thrust (lb$_f$)	Torque (in- lb$_f$)
4.375	1.25	-0.001	0.073	0.138	0.661	0.353
3.75	1.25	-0.005	0.072	0.126	0.659	0.353
3.00	1.25	-0.010	0.075	0.117	0.661	0.356
2.00	1.25	-0.008	0.075	0.121	0.659	0.356
1.00	1.25	-0.002	0.094	0.126	0.666	0.357
4.375	1.25	-0.001	0.073	0.138	0.661	0.353
4.375	0.75	-0.002	0.078	0.154	0.629	0.357
4.375	0	0.023	0.087	0.158	0.644	0.359
4.375	-0.75	0.038	0.071	0.099	0.624	0.353

Table 15. Propeller/MAV Forces and Moments at 8,000 RPM (Rigid Wing)

Axial Separation X_o (in)	Vertical Separation Z_o(in)	Lift (lb$_f$)	Drag (lb$_f$)	Roll Moment (in-lb$_f$)	Thrust (lb$_f$)	Torque (in- lb$_f$)
4.375	1.25	-0.001	0.027	0.046	0.229	0.115
3.75	1.25	0.000	0.026	0.045	0.229	0.121
3.00	1.25	0.000	0.027	0.046	0.229	0.120
2.00	1.25	0.001	0.027	0.051	0.229	0.122
1.00	1.25	0.001	0.035	0.048	0.232	0.123
4.375	1.25	-0.001	0.027	0.046	0.229	0.115
4.375	0.75	0.000	0.028	0.059	0.223	0.124
4.375	0	0.010	0.031	0.056	0.222	0.122
4.375	-0.75	0.015	0.026	0.036	0.220	0.128

Table 16. Propeller/MAV Forces and Moments at 10,000 RPM (Rigid Wing)

Axial Separation X_o (in)	Vertical Separation Z_o(in)	Lift (lb$_f$)	Drag (lb$_f$)	Roll Moment (in-lb$_f$)	Thrust (lb$_f$)	Torque (in- lb$_f$)
4.375	1.25	0.001	0.042	0.072	0.359	0.183
3.75	1.25	-0.003	0.042	0.065	0.363	0.186
3.00	1.25	-0.002	0.042	0.064	0.361	0.189
2.00	1.25	-0.001	0.043	0.064	0.360	0.191
1.00	1.25	0.000	0.055	0.066	0.365	0.194
4.375	1.25	0.001	0.042	0.072	0.359	0.183
4.375	0.75	-0.001	0.044	0.077	0.354	0.195
4.375	0	0.015	0.049	0.079	0.366	0.195
4.375	-0.75	0.024	0.040	0.049	0.343	0.197

Table 17. Propeller/MAV Forces and Moments at 12,000 RPM (Rigid Wing)

Axial Separation X_o (in)	Vertical Separation Z_o(in)	Lift (lb$_f$)	Drag (lb$_f$)	Roll Moment (in-lb$_f$)	Thrust (lb$_f$)	Torque (in- lb$_f$)
4.375	1.25	-0.001	0.060	0.097	0.522	0.271
3.75	1.25	-0.005	0.058	0.095	0.517	0.273
3.00	1.25	-0.005	0.060	0.088	0.520	0.279
2.00	1.25	-0.002	0.063	0.093	0.522	0.280
1.00	1.25	-0.001	0.078	0.095	0.525	0.280
4.375	1.25	-0.001	0.060	0.097	0.522	0.271
4.375	0.75	-0.003	0.062	0.111	0.516	0.283
4.375	0	0.022	0.070	0.118	0.505	0.283
4.375	-0.75	0.034	0.057	0.071	0.498	0.286

Table 18. Propeller/MAV Forces and Moments at 14,000 RPM (Rigid Wing)

Axial Separation X_o (in)	Vertical Separation Z_o(in)	Lift (lb$_f$)	Drag (lb$_f$)	Roll Moment (in-lb$_f$)	Thrust (lb$_f$)	Torque (in- lb$_f$)
4.375	1.25	-0.004	0.077	0.125	0.671	0.356
3.75	1.25	-0.008	0.076	0.118	0.666	0.357
3.00	1.25	-0.009	0.077	0.112	0.665	0.359
2.00	1.25	-0.005	0.078	0.117	0.666	0.359
1.00	1.25	-0.003	0.099	0.119	0.671	0.359
4.375	1.25	-0.004	0.077	0.125	0.671	0.356
4.375	0.75	-0.006	0.080	0.138	0.656	0.360
4.375	0	0.026	0.088	0.150	0.651	0.361
4.375	-0.75	0.045	0.073	0.087	0.633	0.363

Rigid Wing Interaction Plots

Along with the tabular results, the non-dimensional plots of drag to thrust, roll moment to torque and lift to drag for the rigid wing are presented. They can be directly compared to Figures 31, 33, and 35 which show the flexible wing results.
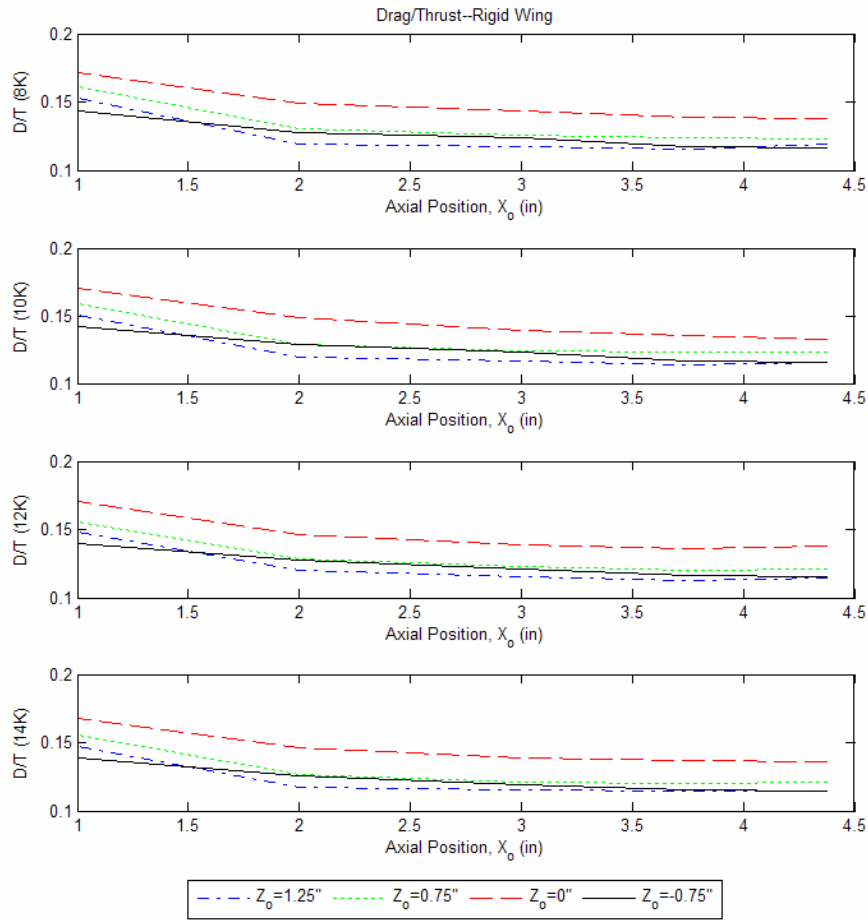

Figure 59. Drag/Thrust Curves at Multiple Wing Locations (Rigid Wing Root Chord=6", Propeller Radius=3")
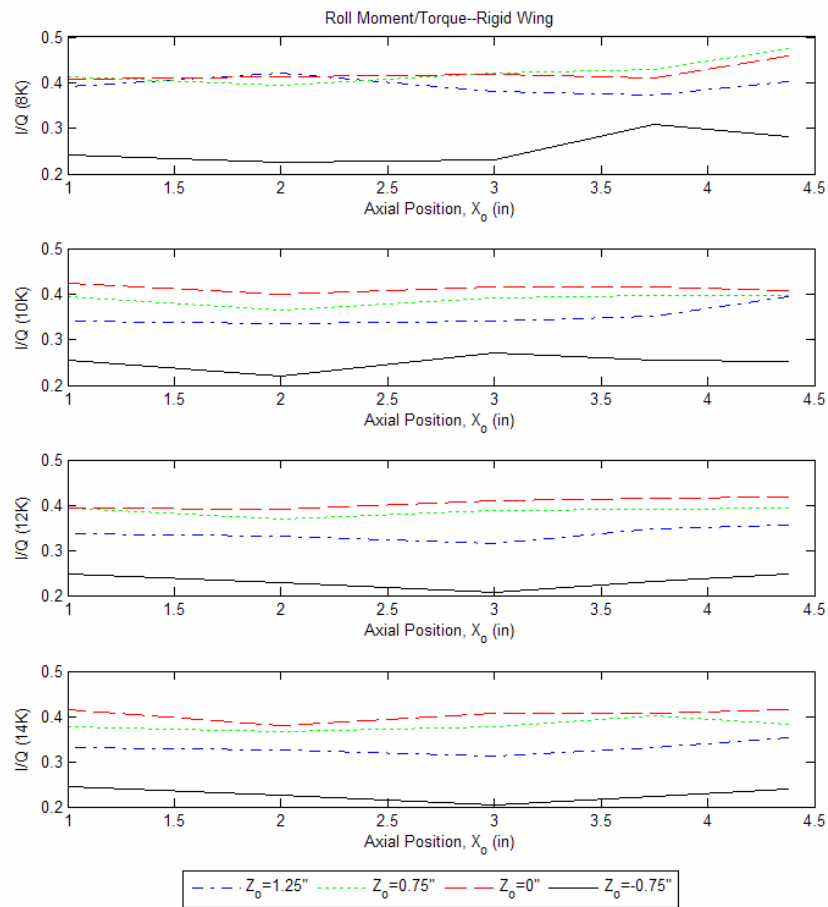
Figure 60. Roll Moment/Torque Curves at Multiple Wing Locations (Rigid Wing Root Chord=6", Propeller Radius=3")
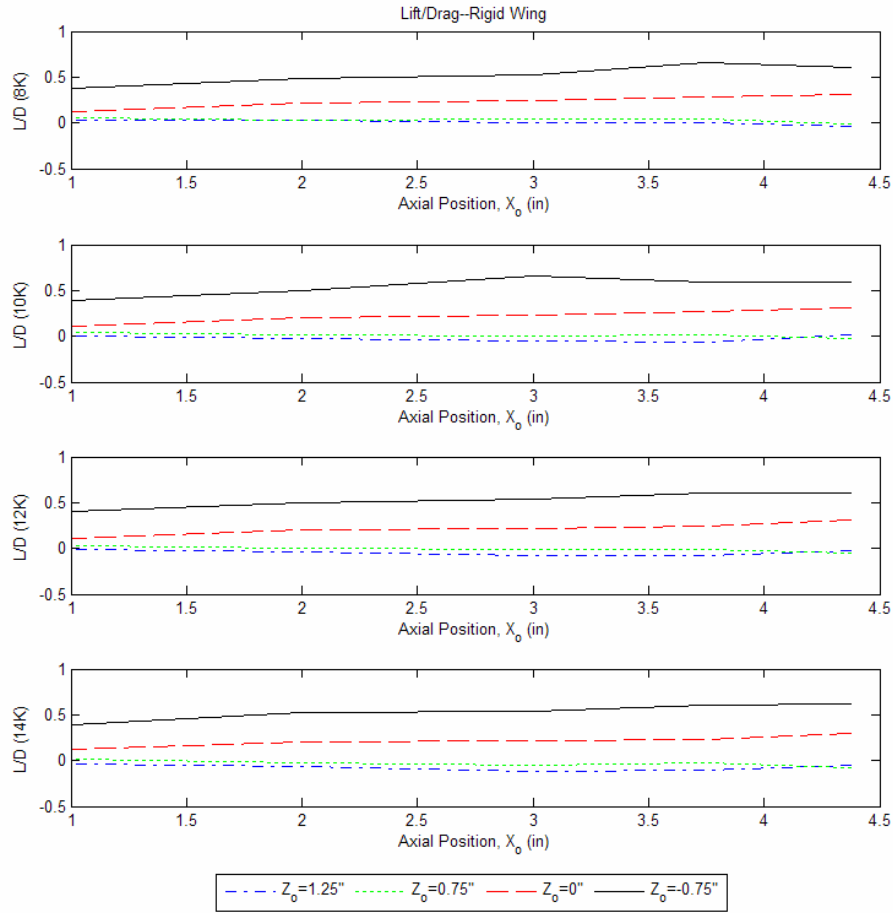
Figure 61. Lift/Drag Curves at Multiple Wing Locations (Rigid Wing Root Chord=6", Propeller Radius=3")

Figure 62 shows a drag comparison for the rigid and flexible wings at X_o=4.375" and X_o=1". The values for thrust are shown from a propeller velocity of 8000 RPM to 14,000 RPM. The plot shows that the thrust values are very similar between the rigid and flexible wings, with the rigid wing having only slightly larger values.
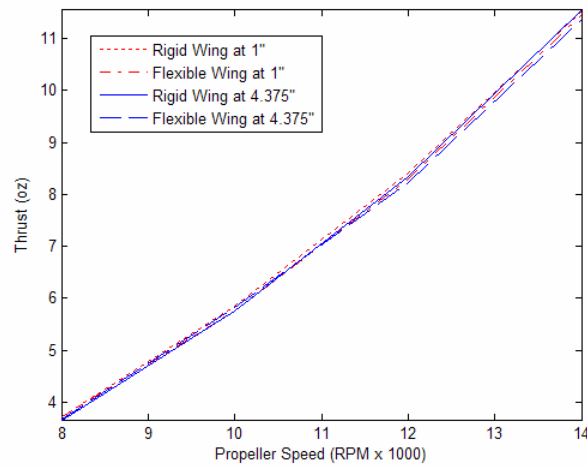
Figure 62. Rigid Wing and Flexible Wing Thrust Comparison (8K to 14K RPM)

Additional Velocity Contour Plots

While the most pertinent results of the wind tunnel velocity profiles are presented in Chapter IV, a few more contour plots were generated during the test runs. Figure 63 shows the velocity profile with no wing attached and the tunnel speed set at 30 *mph*. It shows how a slight velocity deficit remains at the center of the fuselage even when the wing is detached. Figure 64 then shows the velocity profile with no wing attached with a tunnel speed of 30 *mph* and the propeller running. It clearly shows the addition of the propeller wake in the 30 *mph* flow without the interference of the wing.

Figure 63. No Wing with an 11.6 m/s (26 mph) Freestream Only Velocity Profile

Figure 64. No Wing with an 11.6 m/s Freestream, Powered Propeller Velocity Profile
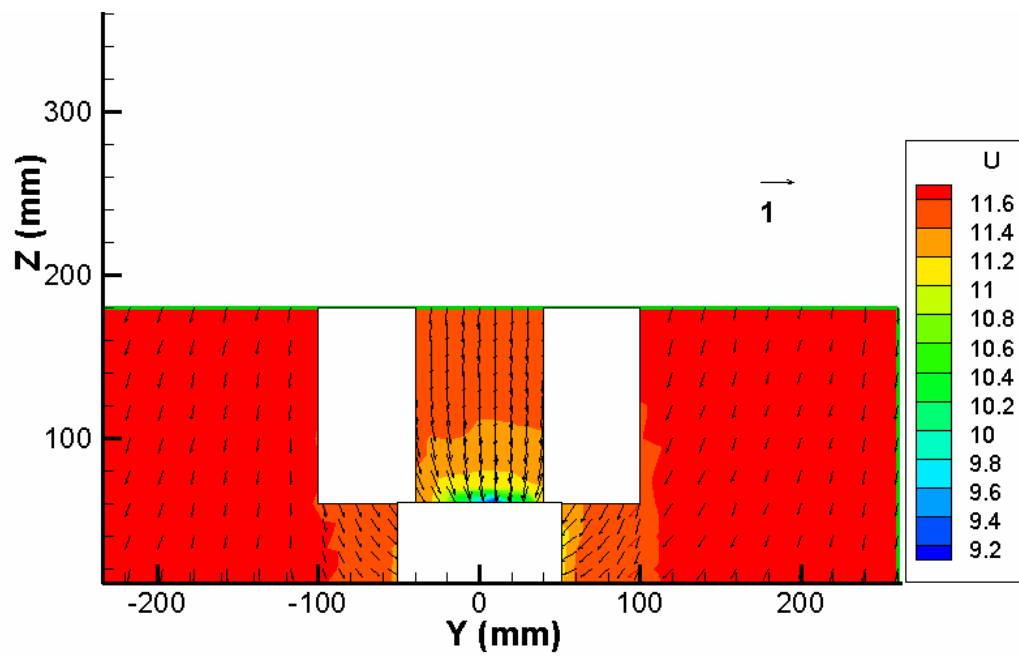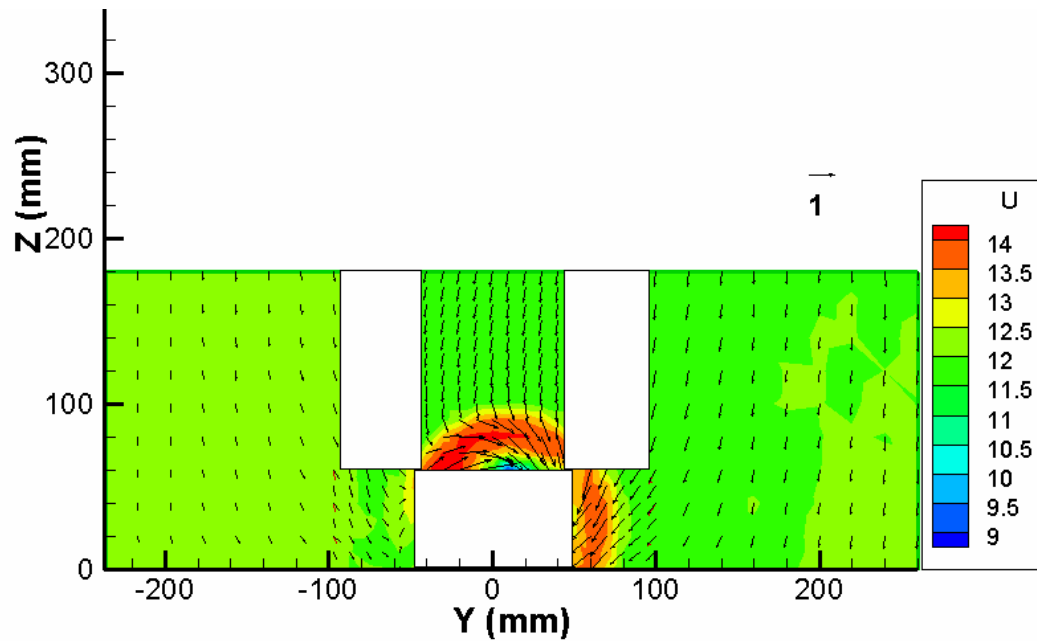
Appendix B: Balance Data Correction

The results of the forces and moments measured by the AFIT-1 balance had to be corrected for strain gauge sensor interactions. The results of the corrected balance values are compared to the raw data in Table 19. In the table, NW means no wing, FW is the flexible wing, RW is the rigid wing and the numbers following indicate tunnel speed and propeller speed (20 or 30 and 8K). The balance titles are the same as described in Chapter III. For the momentum balance analysis the axial component (A1), which represents the net drag minus thrust force, is the only value utilized.

Table 19. Balance Data (Raw and Corrected) Sample Set

	N1	N2	A1	S1	S2	L1
NW-20 Raw Data	0.153	0.265	0.00416	0.0119	-0.1134	0.062
Corrected Data	0.154	0.266	0.00356	0.0179	-0.1114	0.061
FW-20 Raw Data	0.306	0.976	0.0363	0.0017	-0.0092	0.124
Corrected Data	0.310	0.977	0.0366	0.0011	-0.0023	0.125
FW-20/8K Raw Data	0.244	1.188	-0.094	0.0244	-0.154	0.212
Corrected Data	0.249	1.191	-0.093	0.0333	-0.145	0.211
RW-30 Raw Data	0.906	3.770	0.0917	-0.0017	-0.211	0.220
Corrected Data	0.921	3.771	0.0943	0.0254	-0.187	0.219
RW-30/8K Raw Data	0.903	3.710	0.007	0.0024	-0.134	0.231
Corrected Data	0.917	3.710	0.010	0.0289	-0.110	0.231

Appendix C: Instrument Calibration Information

Torque Cell

The torque of the motor is measured by a 50 *in-oz* Lebow torque cell model 2105. Initially, the overhang caused a drift in the instrument, which was corrected by reducing the overhung moment to the specified 100 *in-oz*. The calibration performed by Mr. Andy Pitts yielded the following linear relationship with an excitation of 15 and a gain setting of 1 X 1000 on the Vishay signal conditioning amplifier:

0.729 *VDC* = 1 *in-oz*

Load Cell

The thrust created by the propeller is measured by a 25 *lb$_f$* Interface load cell. From a similar calibration the following linear relationship with an excitation of 7 and a gain setting of 2.54 X 1000 on the same type of amplifier:

0.1418 *VDC* = 1 *oz*

Tachometers

The two tachometers used to measure the speed of the propeller blade provided different advantages. The Monarch TACH-44 provided a very accurate view of the speed of the propeller, but only displayed the RPM numbers visually. In order to automate the data acquisition process, the Extech Instruments photo-tachometer was used which provided at DC voltage output that could be read by Labview™. The Extech was calibrated to match the output of the Monarch since its accuracy is known. The relationship is:

0.0994 *VDC* = 10,000 RPM

AFIT-1 Balance

An excellent description of the calibration process and results for the AFIT-1 balance is provided in Appendix B of Ensign Leveron's thesis (Leveron, 2005:77-85). Mr. Dwight Gehring performs the calibrations regularly and keeps the Labview™ program in the wind tunnel control room updated to reflect the most current calibration.

Tri-Wire Anemometer

As described in Chapter III, the calibration of the Dantec tri-wire is a lengthy process that is carried out in a commercially developed calibration machine. The calibration was performed prior to testing and verified by the Dantec 90H02 Unit Flow Calibrator. Figures 65-67 show the results of the calibration of each wire along with an error estimate derived from the output of the wire compared to the known velocity inside the calibrator.
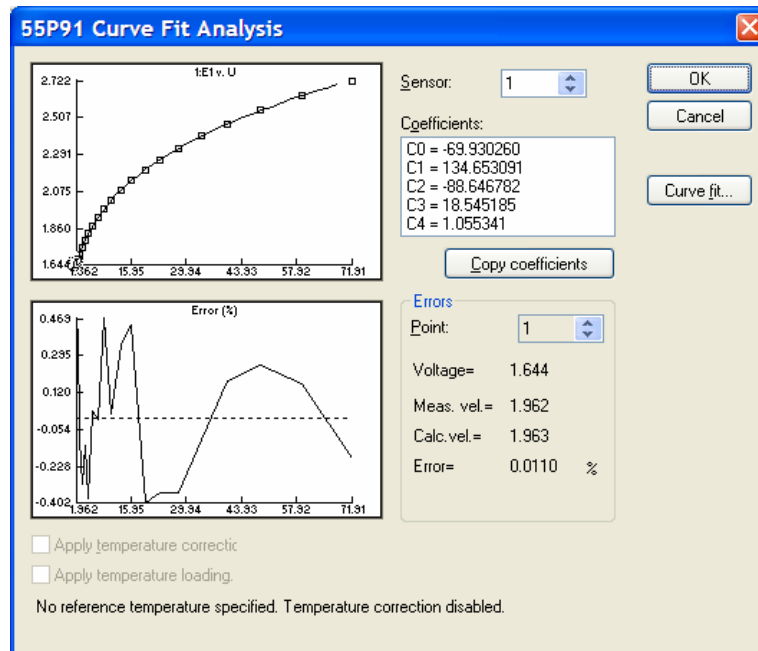
Figure 65. Tri-Wire Anemometer Calibration Sheet (Wire 1)
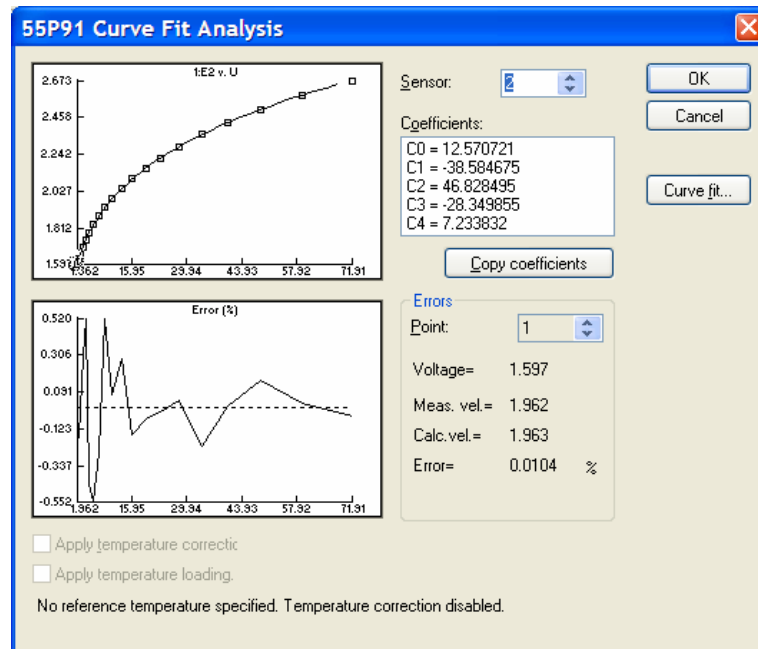
Figure 66. Tri-Wire Anemometer Calibration Sheet (Wire 2)
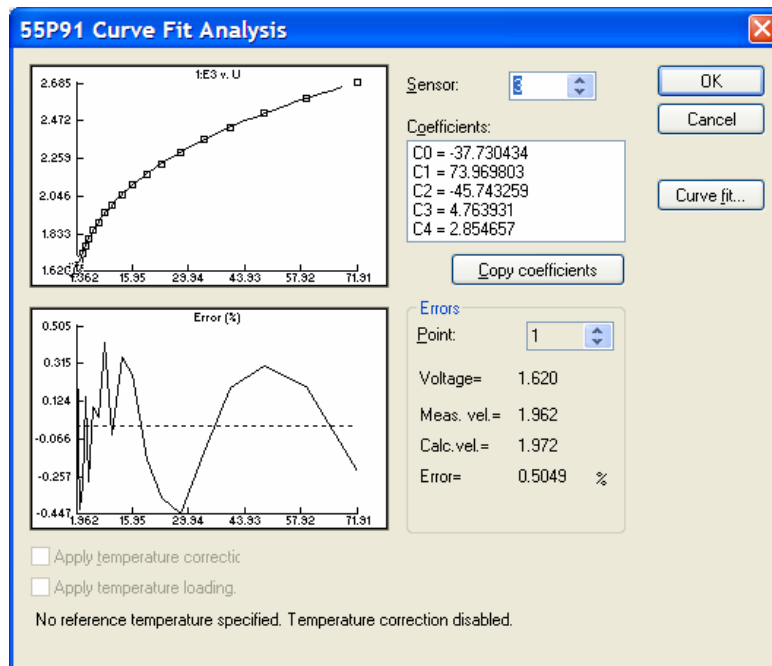
Figure 67. Tri-Wire Anemometer Calibration Sheet (Wire 3)

Appendix D: Additional Pictures/Drawings

Additional pictures of the fuselage testbed as well as test setup are included to help gain a further understanding of the tests conducted. Figure 68 shows a close up picture of the bottom potion of the fuselage testbed that was built on the rapid prototyping machine. Figure 69 is a close up of the top piece where the wing is attached.

Figure 68. Rapid Prototyped Fuselage Testbed (Lower Piece)

Figure 69. Rapid Prototyped Fuselage Testbed (Upper Piece)

A few simple engineering drawings are included that show some of the basic dimensions of the fuselage testbed. Figures 70 and 71 show drawings of the bottom and top sections of the fuselage testbed with the dimensions in inches.
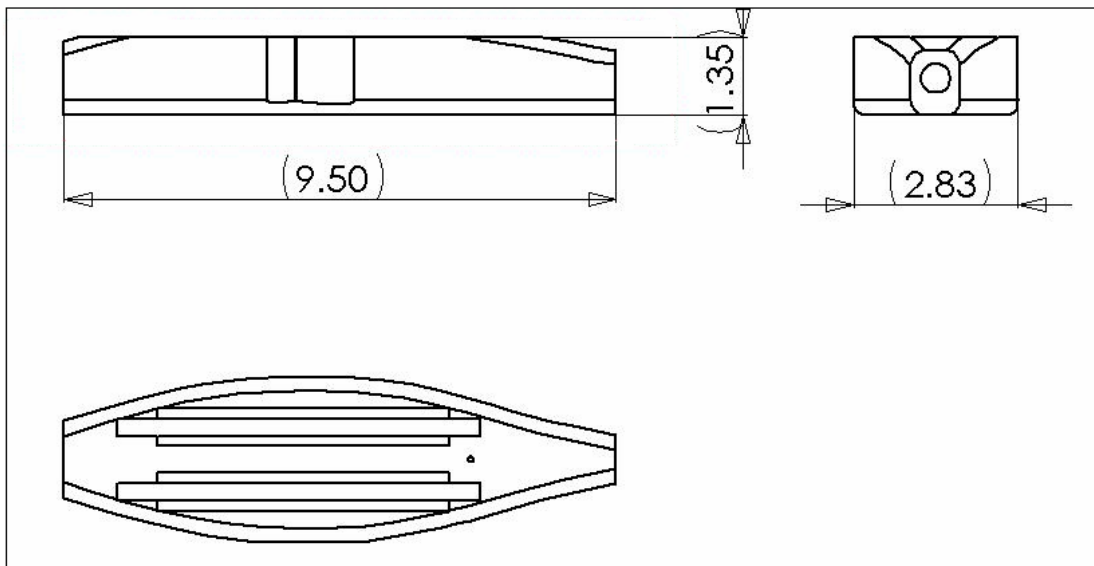
Figure 70. 3 View Drawing of Fuselage Testbed (Bottom)
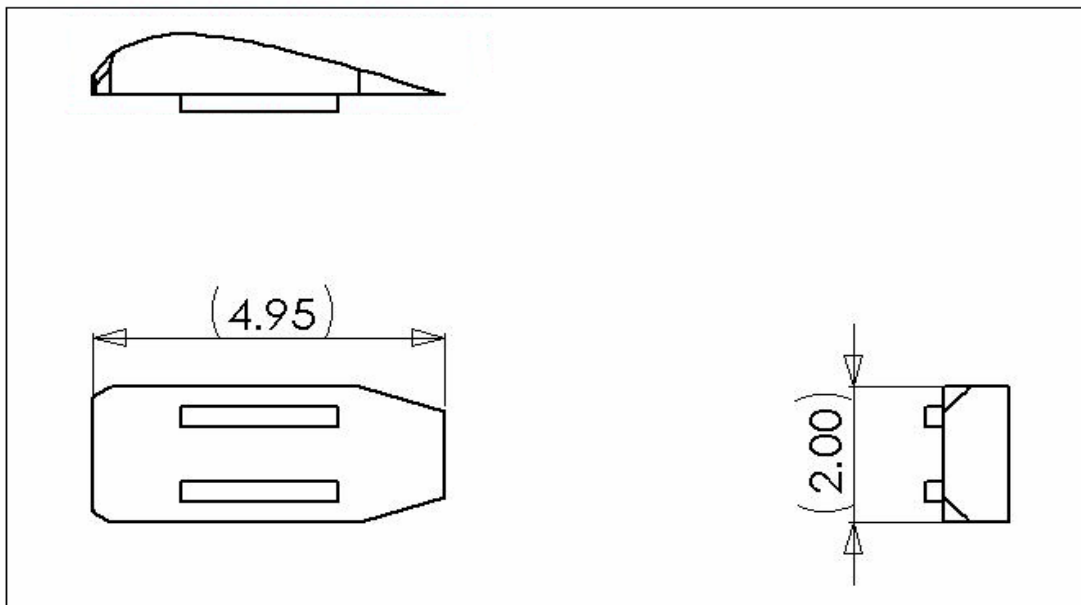
Figure 71. 3 View Drawing of Fuselage Testbed (Top)

The next picture provides a closer view of the separated test setup that was utilized outside the wind tunnel to measure the propeller and MAV forces exclusively. The AFIT-1 balance enters the back of the bottom plastic section and is mounted with two set screws.

Figure 72. Propeller/Wing Interaction Test Setup (MAV/Balance)

The next few pictures further illustrate the setup of the tri-wire anemometer inside the wind tunnel. Figure 73 shows the MAV mounted on the AFIT-1 balance. Figure 74 shows a close up view of the tri-wire anemometer in its test position just aft of the flexible wing inside the wind tunnel.

Figure 73. MAV Mounted on Balance in Wind Tunnel

Figure 74. Tri-Wire Anemometer Mounted Aft of Flexible Wing

Appendix E. Error Analysis

In order to get a good understanding of the errors involved in the experiments

conducted during this research, each pertinent source of error will be individually

discussed. The first and probably most definable source of error comes from the AFIT-1

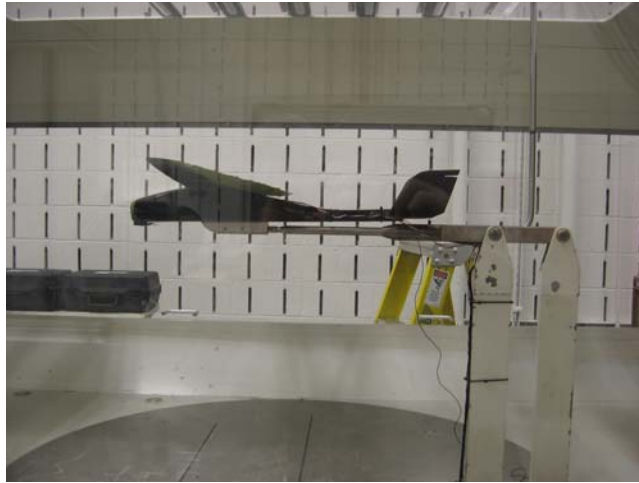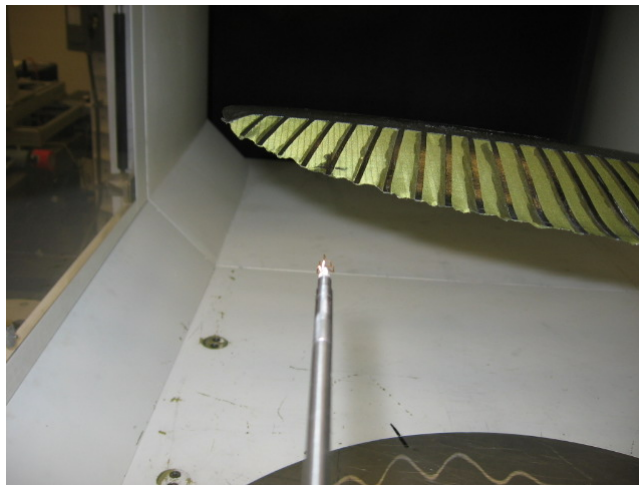balance. The balance has known resolution values that can lead to measurement

uncertainty, especially when dealing with small forces and moments. Table 20 shows the

resolution of the AFIT-1 balance as prescribed by the manufacturer and developed during

calibration. The percentages are taken from the maximum load of each sensor.

Table 20. AFIT-1 Balance Resolution

	Maximum Load	Accuracy	Resolution
Axial Force	5 lb$_f$	0.04%	0.002 lb$_f$
Normal Force	10 lb$_f$	0.12%	0.012 lb$_f$
Side Force	5 lb$_f$	0.07%	0.0035 lb$_f$
Roll Moment	4 in-lb$_f$	0.11%	0.0044 in-lb$_f$
Pitch Moment	10 in-lb$_f$	0.05%	0.005 in-lb$_f$
Yaw Moment	5 in-lb$_f$	0.07%	0.0035 in-lb$_f$

Taking a sample set of balance data from Table 19 for the rigid wing at 30 *mph*, the

following levels of uncertainty apply:

Table 21. Balance Uncertainty Example

	Axial Force	Normal Force	Side Force	Roll Moment	Pitch Moment	Yaw Moment
RW-30	0.0943	0.921	0.0254	0.219	3.771	-0.187
Resolution	0.002	0.012	0.0035	0.0044	0.005	0.0035
Uncertainty %	2.1%	1.3%	13.8%	2.0%	0.1%	1.9%

For most of the tests, these values of uncertainty are reasonable. The exception is when the axial force measurement is very small, which can occur when both the tunnel and the propeller are running. In the case where the tunnel is set at 30 mph and the propeller is running, from Table 19, the axial component measures 0.01 lb_f. Now with a resolution of 0.002, the uncertainty in the result is 20%.

The next potential sources of error are with the Lebow 50 in-oz torque cell and the 25 lb_f Interface load cell. Each manufacturer publishes rated accuracies of these instruments in the form of non-linearity and hysteresis. The torque cell has a non-linearity rating of 0.1% of rated capacity and a hysteresis of 0.1% of rated capacity. Actual performance ratings performed by Lebow show accuracy values of 0.039%. From this the resolution of the torque cell can be estimated at 0.0195 in-oz. Most of the torque measurements taken in the propeller/wing interaction test were on the order of 2.0 in-oz, which would indicate a 0.98% uncertainty in the results. The Interface load cell has a non-linear rating of 0.03% and a hysteresis of 0.02% of rated capacity (interfaceforce.com). Since the tests were performed with the load increasing on the load cell, hysteresis is not limiting the accuracy. Non-linearity is the driving source of error for the load cell and leads to a resolution of 0.0075 lb_f. Most drag measurements were within 0.03 lb_f to 0.09 lb_f which results in a range of uncertainty from 8.3% to 25% depending on the amount of force applied. A smaller range load cell would probably be more appropriate for this type of experiment in the future.

Errors within the tri-wire anemometer are fairly small. Figures 65-67 show the results of a computer analyzed error analysis performed on each wire. It compares the

known velocity values from the flow calibrator with the curve fit it performs on the data from the calibration process. It must be noted that these errors assume the calibration was performed properly with the angle of the oncoming flow at exactly zero degrees and the flow calibrator functioning as advertised from the manufacturer. The percent error is an average over the entire operating range of the hot-wire, which in this case is from 0 to 150 *mph*. Since components of each wire are involved in finding each of the three components of velocity, all of their errors must be analyzed. Wire 1 has an error of 0.011%, wire 2 has an error of 0.0104% and wire 3 has 0.505%. Each is a percentage of the oncoming tunnel velocity. In order to estimate the uncertainty of each velocity component (*u, v, w*), the error propagation equation is used (Figliola & Beasley, 1995:192). The standard equation is:

$$U_Q = \sqrt{\left(\frac{\partial Q}{\partial X_1} U_{X_1}\right)^2 + \left(\frac{\partial Q}{\partial X_2} U_{X_2}\right)^2 \ldots} \qquad \textbf{(15)}$$

Performing the error propagation on equation **(11)** from Chapter III, which is the method the software utilizes to find the components of velocity, the following uncertainty estimates arise:

Table 22. Hot-Wire Uncertainty

Velocity Component	Uncertainty %	At 12 m/s
u	0.29%	0.035 m/s
v	0.01%	0.0012 m/s
w	0.41%	0.0492 m/s

This shows that both the *u* and *v* components of the velocity data are quite accurate, while the *w*-component, which should be close to zero for most of the tests, has a slightly higher uncertainty. The extremely low uncertainty in the *v*-component is due to the *cos(90)* term that is multiplied by the wire 3 error, effectively not including wire 3 in its calculation. Since only the *u*-component is utilized in the momentum balance, the velocity profile is considered a small source of error. The bias error inherent in the velocity profile interpolation and integration dominates the momentum balance results.

The error propagation equation can also be used to evaluate the uncertainty in the propeller performance coefficients. Performing the error propagation on equations **(2)** and **(3)** from Chapter II and utilizing the torque and load cell errors from above along with a ±10 RPM uncertainty in the propeller speed, the following uncertainty examples are given at two different propeller speeds:

Table 23. Propeller Coefficient Uncertainty

Propeller Coefficient	8000 RPM	Uncertainty %	14,000 RPM	Uncertainty %
C_T	0.0112	3.3%	0.0105	1.2%
C_Q	0.0020	0.3%	0.0019	0.17%

These are representative uncertainty estimates for the extreme propeller speeds of 8000 and 14,000 RPM. The data were taken from the flexible wing test at its design location while mounted on the static test stand. It assumes a ±10 RPM uncertainty due to variations in propeller speed during each test. The propeller speeds were time-averaged over a 10 second time interval during the tests to produce the actual results.

125

Bibliography

1. Anderson, E. and Lawton, T., "Correlation Between Vortex Strength and Axial Velocity in a Trailing Vortex." *Journal of Aircraft*, Vol. 40, No. 4, 2003: 699-703.

2. Ardito Marretta, R.M., "Different Wings Flowfields Interaction on the Wing-Propeller Coupling." *Journal of Aircraft*, Vol. 34, No. 6, 1997: 740-746.

3. AV8N Aircraft Handbook. Online at http://www.av8n.com/how/htm/intro.html. Accessed 15 January 2006.

4. Bi, Nai-pei and Leishman, J. Gordon, "Experimental Study of Rotor/Body Aerodynamic Interactions." *Journal of Aircraft*, Vol. 27, No. 9, 1990: 779-788.

5. Chiaramonte, J., Favier, D., Maresca, C., and Benneceur, S., "Aerodynamic Interaction Study of the Propeller/Wing Under Different Flow Conditions." *Journal of Aircraft*, Vol. 33, No. 1, 1996: 46-52.

6. Chiocchia, G., Pignataro, S., "On the Induced Drag Reduction Due to Propeller-Wing Interaction." *Aeronautical Journal*, 1995: 328-336.

7. Cho, Jinsoo and Williams, Marc H., "Propeller-Wing Interaction Using A Frequency Domain Panel Method." *Journal of Aircraft*, Vol 27, 1990: 196-202.

8. Dantec Dynamics. Online at http://dantecdynamics.com. Accessed 05 January 2006.

9. Defense Advanced Research Projects Agency. Online at http://www.darpa.mil. Accessed 18 November 2005.

10. DeLuca, Anthony M., "Experimental Investigation into the Aerodynamic Performance of Both Rigid and Flexible Wing Structured Micro Air Vehicles." AFIT Thesis AFIT/GAE/ENY/04-M06, (Mar 04).

11. DeLuca, Anthony M., Reeder, Mark F., OL, Michael V., and Freeman, Jacob, "Experimental Investigation into the Aerodynamic Properties of a Flexible and Rigid Wing Micro Air Vehicle." AIAA Paper 2004.

126

12. E, Q., Yang, G., and Li, F., "Numerical Analysis of the Interference Effect of Propeller Slipstream on Aircraft Flowfield." *Journal of Aircraft*, Vol. 35, No. 1, 1998: 84-90.

13. Elsaadawy, Ehab A. and Britcher, Colin P., "Physical Model of a Propeller Slipstream Interacting with a Boundary Layer at Low Reynolds Number." AIAA Paper 2004-6590, (Sep 2004).

14. Favier, D., Ettaouil, and Maresca, C., "Numerical and Experimental Investigation of Isolated Propeller Wakes in Axial Flight." *Journal of Aircraft*, Vol. 26, No. 9, 1989: 837-846.

15. Federation of American Scientists (FAS). Online at http://www.fas.org/irp/program/collect/mav.htm. Accessed 18 November 2005.

16. Figliola, R.S. and Beasley, D.E., *Theory and Design for Mechanical Measurements* (2nd Edition). New York: John Wiley & Sons, 1995.

17. Fratello, G., Favier, D., and Maresca, C., "Experimental and Numerical Study of the Propeller/Fixed Wing Interaction." *Journal of Aircraft*, Vol. 28, No. 6, 1991: 365-373.

18. Fukada, R., Nigim, H., and Koyama, H., "Measurements and Visualization in the Flowfield Behind a Model Propeller." *Journal of Aircraft*, Vol. 33, No. 2, 1996: 407-413.

19. Gebbie, David A., "Experimental Study of the Subsonic Aerodynamics of a Blended Wing Body Air Vehicle with a Focus on Rapid Technology Assessment." AFIT Thesis AFIT/GAE/ENY/05-M09, (Mar 05).

20. Higgs, Travis J., "Modeling, Stability, and Control of a Rotatable Tail on a Micro Air Vehicle." AFIT Thesis AFIT/GAE/ENY/06-05, (Dec 05).

21. Houghton, E.L. and Carpenter, P.W., *Aerodynamics for Engineering Students* (4th Edition). New York: John Wiley & Sons, 1993.

22. Ifju, P.G., Jenkins, D.A., Ettinger, S., Lian, Y.,Shyy, W., and Waszak, M.R., "Flexible-Wing-Based Micro Air Vehicles." AIAA Paper 2002-0705, (Jan 2002).

23. Igue, Roberto T., "Experimental Investigation of a Lift Augmented Ground Effect Platform." AFIT Thesis AFIT/GAE/ENY/05-S04, (Sep 05).

24. Interface Advanced Force Measurement. Online at http://www.interfaceforce.com. Accessed 07 February 2006.

25. Kuethe, Arnold M., Chow, Chuen-Yen, *Foundation of Aerodynamics-Bases of Aerodynamic Design* (4th Edition). New York: John Wiley & Sons, 1986.

26. Leishman, J. Gordon, *Principles of Helicopter Aerodynamics*. Cambridge University Press, 2000.

27. Leishman, J. Gordon and Bi, Nai-pei, "Experimental Investigation of Rotor/Lifting Surface Interactions." *Journal of Aircraft*, Vol. 31, No. 4, 1994: 846-854.

28. Lepicovsky, J. and Bell, W.A., "Aerodynamic Measurements About a Rotating Propeller with a Laser Velocimeter." *Journal of Aircraft*, Vol. 21, No. 4, 1984: 264-271.

29. Leveron, Troy A., "Characterization of a Rotary Flat Tail as a Spoiler and Parametric Analysis of Improving Directional Stability in a Portable UAV." AFIT Thesis AFIT/GAE/ENY/05-J06, (Jun 05).

30. McMichael, J.M. and Francis, M.S., "Micro Air Vehicles-Toward a New Dimension in Flight." http://www.darpa.mil/tto/mav/mav_auvsi.html, (Dec 1997).

31. Mueller, T.J., *Low Reynolds Number Aerodynamics*. New York: Springer-Verlag, 1989.

32. Nelson, Wilbur C., *Airplane Propeller Principles*. New York: John Wiley & Sons, 1944.

33. Raymer, Daniel P., Aircraft Design: A Conceptual Approach (2nd Edition). Washington D.C.: AIAA Education Series, 1992.

34. Rivera Parga, Jose R., "Wind Tunnel Investigation of the Static Stability and Control Effectiveness of a Rotary Tail in a Portable UAV." AFIT Thesis AFIT/GAE/ENY/04-D02, (Dec 04).

35. Shyy, W., Klevebring, F., Nilsson, M., Sloan, J., Carroll, B., and Fuentes, C., "Rigid and Flexible Low Reynolds Number Airfoils." *Journal of Aircraft*, Vol. 36, No. 3, 1999: 523-529.

36. Shyy, W. and Smith, R., "A Study of Flexible Airfoil Aerodynamics with Application to Micro Aerial Vehicles." AIAA Paper 1997-1933. (Jul 1997)

37. *Streamline Installation and User's Guide* (1st Edition). Skovlunde, Denmark: Dantec Measurement Technology, 1996.

38. Witkowski, D.P., Lee, A.K.H., and Sullivan, J.P., "Aerodynamic Interaction Between Propellers and Wings." *Journal of Aircraft*, Vol. 26, No. 9, 1989: 829-836.

39. Waszak, M.R. and Jenkins, L.N., "Stability and Control Properties of an Aeroelastic Fixed Wing Micro Aerial Vehicle." AIAA Paper 2001-4005, (Aug 2001).

Vita

       Capt Brian J. Gamble was born and raised in Montana. He graduated Fergus

High School in 1994 and accepted an Air Force ROTC scholarship to Notre Dame. He

earned a Bachelor of Science in Aerospace Engineering from the University of Notre

Dame in 1998. He was commissioned a 2nd Lieutenant in the Air Force in May, 1998 and

assumed his first assignment at Wright-Patterson AFB, Ohio. There he was an engineer

on the C-17 Aircrew Training System. He also worked in the Air Vehicles Lab on the

modernization of UAVs. His second assignment was to Malmstrom AFB, MT where he

was the lead engineer and officer in charge of the technical engineering branch dealing

with the Minuteman III weapon system. In August, 2004 he entered the Graduate School

of Engineering and Management, Air Force Institute of Technology. Upon graduation in

March, 2006, he will be assigned to the Air Force Research Laboratory at Wright-

Patterson AFB.

REPORT DOCUMENTATION PAGE

1. REPORT DATE (DD-MM-YYYY)	2. REPORT TYPE	3. DATES COVERED (From – To)
23-03-2006	Master's Thesis	August 2004 – March 2006

4. TITLE AND SUBTITLE

Experimental Analysis of Propeller Interactions with a Flexible Wing Micro-Air-Vehicle

5a. CONTRACT NUMBER

5b. GRANT NUMBER

5c. PROGRAM ELEMENT NUMBER

6. AUTHOR(S)

Gamble, Brian J., Captain, USAF

5d. PROJECT NUMBER
JON #05-304

5e. TASK NUMBER

5f. WORK UNIT NUMBER

7. PERFORMING ORGANIZATION NAMES(S) AND ADDRESS(S)
Air Force Institute of Technology
Graduate School of Engineering and Management (AFIT/EN)
2950 Hobson Way, Building 640
WPAFB OH 45433-8865

8. PERFORMING ORGANIZATION REPORT NUMBER

AFIT/GAE/ENY/06-M10

9. SPONSORING/MONITORING AGENCY NAME(S) AND ADDRESS(ES)
Air Force Research Laboratory, Air Vehicles Directorate
Attn: Mr. Michael OL (AFRL/VAAA)
2130 8th St., Bldg. 45
Wright-Patterson AFB OH 45433

10. SPONSOR/MONITOR'S ACRONYM(S)

11. SPONSOR/MONITOR'S REPORT NUMBER(S)

12. DISTRIBUTION/AVAILABILITY STATEMENT

APPROVED FOR PUBLIC RELEASE; DISTRIBUTION UNLIMITED.

13. SUPPLEMENTARY NOTES

14. ABSTRACT An investigation into the effects of the propeller slipstream on a flexible wing micro-air-vehicle (MAV) was conducted. The Air Force Research Lab, Munitions Directorate designed a man-portable MAV with a 24" wingspan and 6" root chord to be used for battle damage assessment and reconnaissance. Two wings have been developed for this MAV. One is a rigid carbon-fiber wing and the other consists of flexible parachute material attached to a carbon-fiber skeleton. Experimental methods were implemented to investigate propeller and wing interactions, characterizing torque and thrust requirements on the motor along with aerodynamic forces on the aircraft as the wing was placed in various locations. Initially, the motor and propeller were mounted on an air bearing table and connected to a torque and load cell. A fuselage prototype was developed and built to mount the wing at multiple heights and distances from the propeller while keeping the same angle of attack. The airframe was attached to a six degree-of-freedom balance. A tri-axial hot-wire anemometer was used to capture velocity profiles in the wind tunnel to characterize propeller wake interactions. Momentum theory provided a method to extract drag and thrust from the velocity profiles. Propeller wake results indicate 12-18% of propeller thrust translates into aircraft drag while 25-45% of motor torque is countered by aircraft roll moment. Values depend on wing location. Results indicate that changing wing location is a viable option for improving pitch and yaw stability, without increasing power requirements.

15. SUBJECT TERMS
Micro air vehicle, flexible wing, hot wire anemometry, balances, momentum balance

16. SECURITY CLASSIFICATION OF:			17. LIMITATION OF ABSTRACT	18. NUMBER OF PAGES	19a. NAME OF RESPONSIBLE PERSON
a. REPORT	b. ABSTRACT	c. THIS PAGE			Mark F. Reeder, Ph.D.,Civ
U	U	U	UU	149	19b. TELEPHONE NUMBER (Include area code) (937) 255-3636, ext 4530 (mark.reeder@afit.edu)